

02/15/96

**VARIABLE POLARITY PLASMA ARC  
TORCH PERFORMANCE AND DESIGN ANALYSIS**

**Final Report**

**March 29, 1994 - September 30, 1996**

**Contract NAS8-39930**

**Prepared for: NASA Marshall Space Flight Center  
Marshall Space Flight Center, AL**

**Prepared by: Richard W. Richardson, Associate Professor  
Jesus M. Pagan, Graduate Research Associate  
Department of Industrial, Welding and Systems  
Engineering  
Vish V. Subramaniam, Associate Professor  
Shashi M. Aithal, Graduate Research Associate  
V. Babu, Research Associate  
Department of Mechanical Engineering  
The Ohio State University  
Columbus, OH 43210**





Welding Engineering

Department of Industrial, Welding  
and Systems Engineering  
190 West 19th Avenue  
Columbus, OH 43210-1182  
Phone 614-292-6841  
FAX 614-292-6842

December 11, 1996

NASA Center for Aerospace Information  
Attn: Accessioning Department  
800 Eldridge Landing Road  
Linthicum Heights, MD 21090-2934

Find enclosed two copies of the final report for contract NAS8-39930.

Sincerely,

Richard W. Richardson  
Co-Principal Investigator

Enclosures



# REPORT DOCUMENTATION PAGE

Form Approved  
OMB No. 0704-0188

Public reporting burden for this collection of information is estimated to average 1 hour per response, including the time for reviewing instructions, searching existing data sources, gathering and maintaining the data needed, and completing and reviewing the collection of information. Send comments regarding this burden estimate or any other aspect of this collection of information, including suggestions for reducing this burden, to Washington Headquarters Services, Directorate for Information Operations and Reports, 1215 Jefferson Davis Highway, Suite 1204, Arlington, VA 22202-4302, and to the Office of Management and Budget, Paperwork Reduction Project (0704-0188), Washington, DC 20503.

1. AGENCY USE ONLY (Leave blank)		2. REPORT DATE 12-11-96	3. REPORT TYPE AND DATES COVERED Final Report 3-29-94 to 9-30-96	
4. TITLE AND SUBTITLE VPPA Torch Performance and Design Analysis			5. FUNDING NUMBERS Contract #NAS8-39930	
6. AUTHOR(S) Richard W. Richardson and Vish V. Subramaniam			8. PERFORMING ORGANIZATION REPORT NUMBER RF 861701/728930	
7. PERFORMING ORGANIZATION NAME(S) AND ADDRESS(ES) The Ohio State University Research Foundation 1960 Kenny Rd. Columbus, Ohio 43210			9. SPONSORING/MONITORING AGENCY NAME(S) AND ADDRESS(ES) National Aeronautics & Space Administration George C. Marshall Space Flight Center Marshall Space Flight Center, Alabama 35812	
11. SUPPLEMENTARY NOTES			10. SPONSORING/MONITORING AGENCY REPORT NUMBER	
12a. DISTRIBUTION/AVAILABILITY STATEMENT			12b. DISTRIBUTION CODE	
13. ABSTRACT (Maximum 200 words) The VPPA welding process has been studied with a focus on the operation of the VPPA welding torch and the occurrence of arc skew. Arc skew has been found to mainly arise from asymmetries in the electrode and orifice geometry. The arc generally skews to the side of the torch to which there is asymmetric constriction in the flow through the electrode and orifice. The main operational occurrences of asymmetries leading to skew are initial misalignments of the electrode and orifice, and deterioration of the electrode and orifice with time. The pilot arc operates asymmetrically and produces skew, and also promotes asymmetric deterioration of the electrode and orifice. Electrode positive operation of the VP arc is mainly responsible for electrode and orifice deterioration. Circuit design modifications to redirect the electrode positive current flow were conceived and tested. One design directs current flow to the outer orifice surface, another to a second, auxilliary electrode. Both showed promise for reducing electrode and orifice deterioration, and for allowing higher welding currents to be utilized.				
14. SUBJECT TERMS			15. NUMBER OF PAGES 166	
			16. PRICE CODE	
17. SECURITY CLASSIFICATION OF REPORT UNCLASSIFIED	18. SECURITY CLASSIFICATION OF THIS PAGE UNCLASSIFIED	19. SECURITY CLASSIFICATION OF ABSTRACT UNCLASSIFIED	20. LIMITATION OF ABSTRACT	



**VARIABLE POLARITY PLASMA ARC  
TORCH PERFORMANCE AND DESIGN ANALYSIS**

**Final Report**

**March 29, 1994 - September 30, 1996**

**Contract NAS8-39930**

**Prepared for: NASA Marshall Space Flight Center  
Marshall Space Flight Center, AL**

**Prepared by: Richard W. Richardson, Associate Professor  
Jesus M. Pagan, Graduate Research Associate  
Department of Industrial, Welding and Systems  
Engineering  
Vish V. Subramaniam, Associate Professor  
Shashi M. Aithal, Graduate Research Associate  
V. Babu, Research Associate  
Department of Mechanical Engineering  
The Ohio State University  
Columbus, OH 43210**





## SUMMARY

Fundamental investigations have been conducted under Contract NAS8-39930 to study the VPPA welding arc to help refine and extend the application of the VPPA process. This summary is intended to highlight the main objectives and accomplishments of this work. Two particular objectives were of interest. One objective was to determine the source of the chronic occurrence of arc blow or skew of the plasma arc encountered during production welding. This arc skew produces an unacceptable undercut of the weld bead which does not meet quality specifications. The other objective was to investigate modifications to the design of the plasma torch to extend its current capacity and allow the welding of thicker materials. Two coordinated approaches were taken in this investigation to accomplish these objectives. In one approach, laboratory experimentation was conducted to provide data on the VPP arc and its operation. In the other approach, a computational model of the VPP arc was developed in order to allow computer simulation, and subsequent elucidation of relevant physical processes in the arc. Most useful results came from the experimental investigations, resulting in suggested improvements to the VPP system which have potential for impact relative to the problems of interest. The development of the computational model overcame significant barriers, and produced significant advancements in the modeling of high pressure arcs like the VPP arc. Unfortunately, the modeling task was more difficult than originally envisaged, and useful solutions emerged too late in the project to provide impact in the investigations. Nonetheless, the course of experimental progress was influenced greatly by interchange with the theoretical effort and expertise. Insight into physical processes were very useful in the consideration of sources of the skew phenomenon.

The main line of experimental effort was aimed at investigating the occurrence of the VPP arc skew. Arc skew was primarily documented by recording video images of the arc with simultaneous viewing of the arc from the front and the side. A split screen type of display was used for simultaneous recording of the arc images. This allowed the amount and direction of skew to be observed clearly. Most video observations were done with the arc operating to a copper anode instead of an aluminum work piece to allow extended observation times. Also, a relatively long arc was used to enhance viewing of skew. An off-line, high magnification video system was also used to record and document the condition of the VPP electrode and orifice before and after use. Some of the most fruitful studies were those directed at documenting the deterioration of the electrode and orifice after various conditions of operation. These observations led to interest in current paths in the arc and torch, and related power dissipation locations. This, in turn, led to the testing of some concepts for altering current flow paths and improving torch operation. Experimental work was also conducted to determine the pressure distribution created on the anode by the plasma arc, and to measure heat loads on the plasma torch and anode as a function of operating conditions.

## Arc Skew Detection

A key result obtained from video observations was that arc skew generally occurs because of asymmetries in the geometry of the plasma arc electrode and orifice. This is not a new nor surprising result, but was investigated more systematically than is known to have been done in the past. It was generally observed that the arc skews in the direction of any constriction in the flow, as illustrated in Figure 1. This is because any point of constriction in the flow between the electrode and orifice forces greater flow through the diametrically opposed side of the orifice. This creates a cross flow toward the side of the constriction which the arc follows. It was confirmed that this happens when any asymmetric preparation is made to the electrode or orifice - for instance, taking some material off of one edge of the electrode, or offsetting the orifice hole slightly to one side. It was also documented that random misalignment of the electrode centerline with the orifice created the same result. It was also observed that the pilot arc operates asymmetrically between the electrode and orifice. This can be observed by viewing the end of the torch while operating the pilot arc alone. Invariably, when operated with the pilot arc, the main plasma arc can be observed to skew towards the side to which the pilot arc was observed. Skew can also be observed to come and go with switching of the pilot arc on and off during operation. The pilot arc produced skew was observed to vary from significant to very slight. These observations, plus considerations of other theorized sources of skew, led to the conclusions that skew mainly occurs due to asymmetries in electrode/orifice geometry which disturb the high velocity flow of plasma from the torch. Asymmetries may arise from a variety of causes.

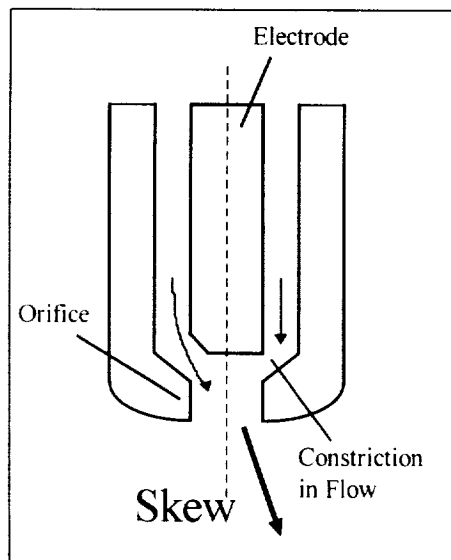
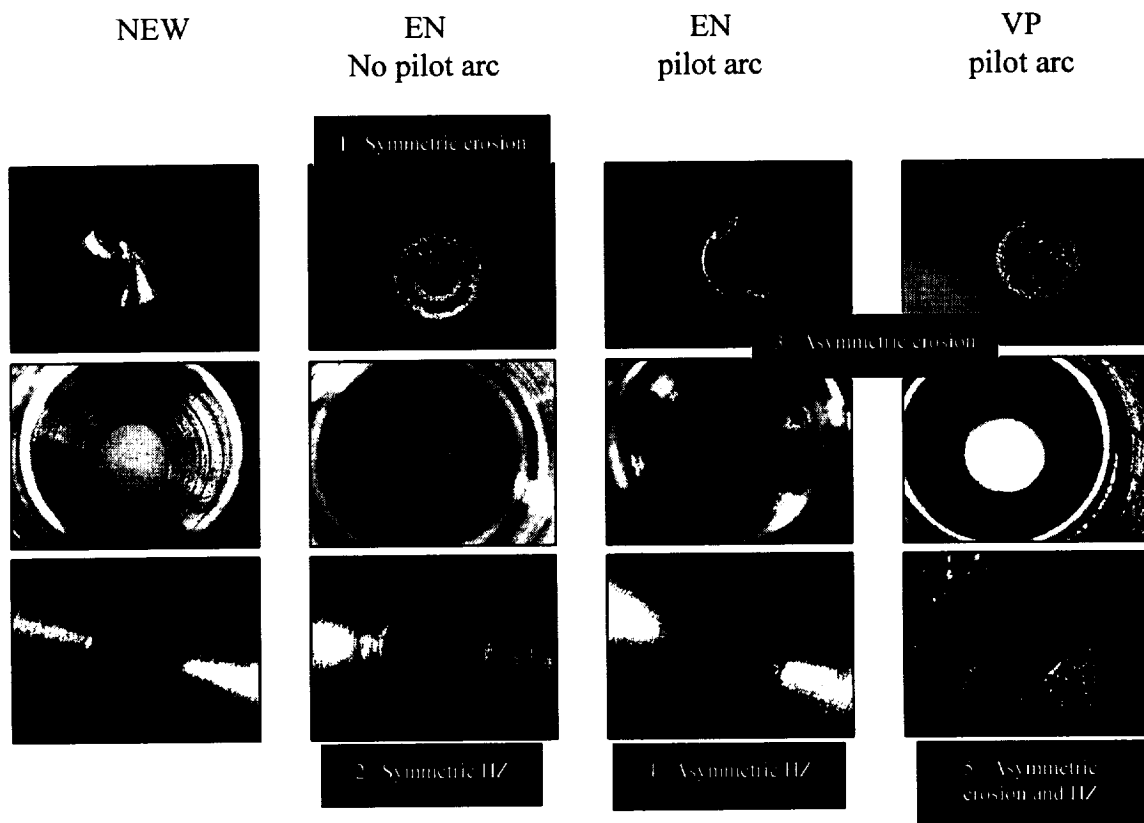


Figure 1: Direction of arc skew.

## Asymmetric Deterioration

With the above results in mind, asymmetric deterioration of the electrode/orifice geometry with operation was investigated as a probable source of skew development during long weld runs. Systematic tests were conducted that involved operating the arc for various lengths of time under different operating conditions. The orifice and electrode conditions were recorded and analyzed with a high magnification video system after each run. Runs as short as twenty minutes were found to produce significant deterioration results. Figure 2 shows video images taken of the electrode, and inner and outer orifice surfaces (in that order vertically in figure), after various conditions of operation. They are compared to a typical unused (new) electrode and orifice condition. Conditions of operation depicted in Figure 2 consisted of EN without the pilot arc, EN with the pilot arc, and VP with the pilot arc. The arc was operated for twenty minutes on a copper anode.



**Figure 2: Electrode and orifice condition with after various operating conditions.**

It can be seen from Figure 2 that EN arc operation produces a very even and symmetric heating pattern on the electrode and orifice, with minimal deterioration. EN operation with the pilot arc produces a distinctly asymmetric heating pattern on the electrode and orifice, which is associated with the location of pilot arc operation. A



similar asymmetry, with a much pronounced amount of deterioration, can be observed for the VP case with the pilot arc. The greater amount of deterioration can be associated with the EP cycle of operation which is known to deposit extra heat into the electrode. Again, the asymmetric location of heat deposition and deterioration on the electrode and orifice was associated with the location of the pilot arc attachment. Significant deterioration of the outer orifice surface is also observed. Thus, the combination of EP and pilot arc operation would be expected to create significant asymmetric deterioration over the course of long weld runs. It is thought that this must be the primary source of arc skew under production conditions. Unfortunately, no reasonable way of simulating long production run conditions in the lab was conceived to provide absolute verification.

### Current Flow Path Analysis

Current flow paths in the welding circuit and torch were analyzed since they have a close association with points of heat dissipation in the torch components, mainly the arc electrode and orifice. This heat dissipation creates the observed deterioration. The current flow paths are easy to establish in the case when operation is EN. This is illustrated in Figure 3 where electron flow is indicated.

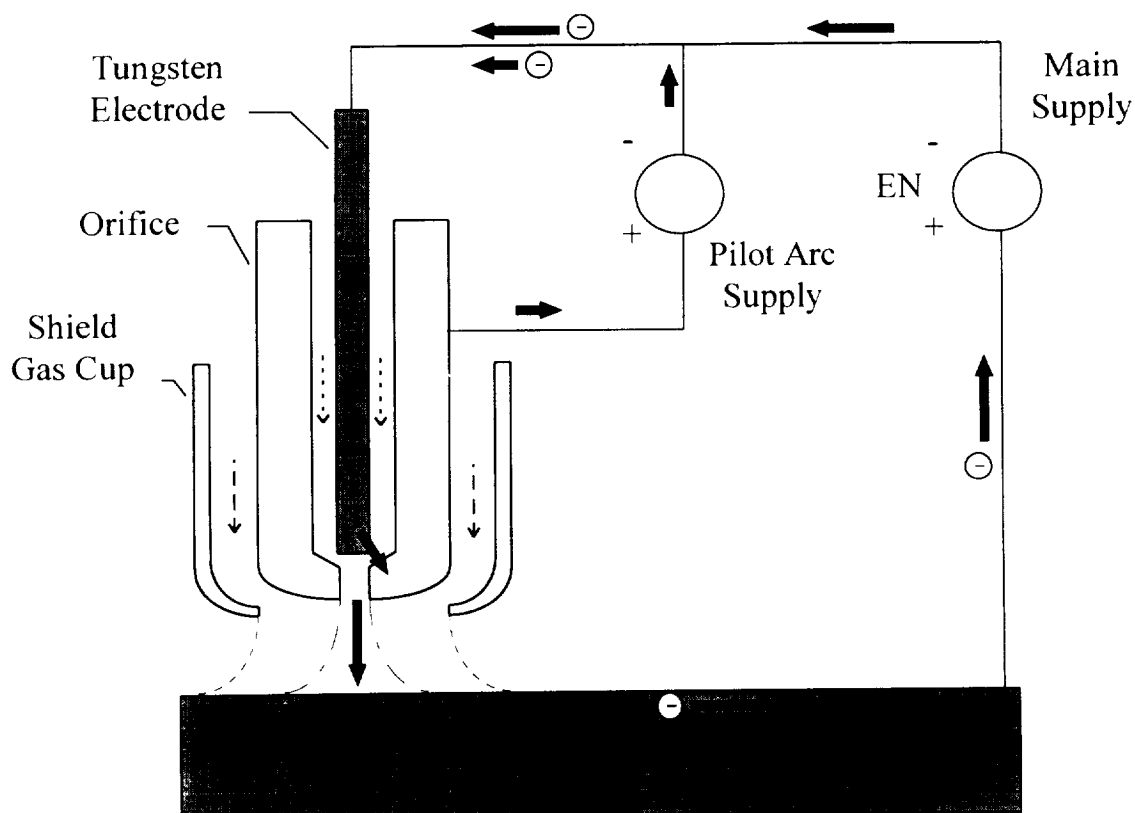
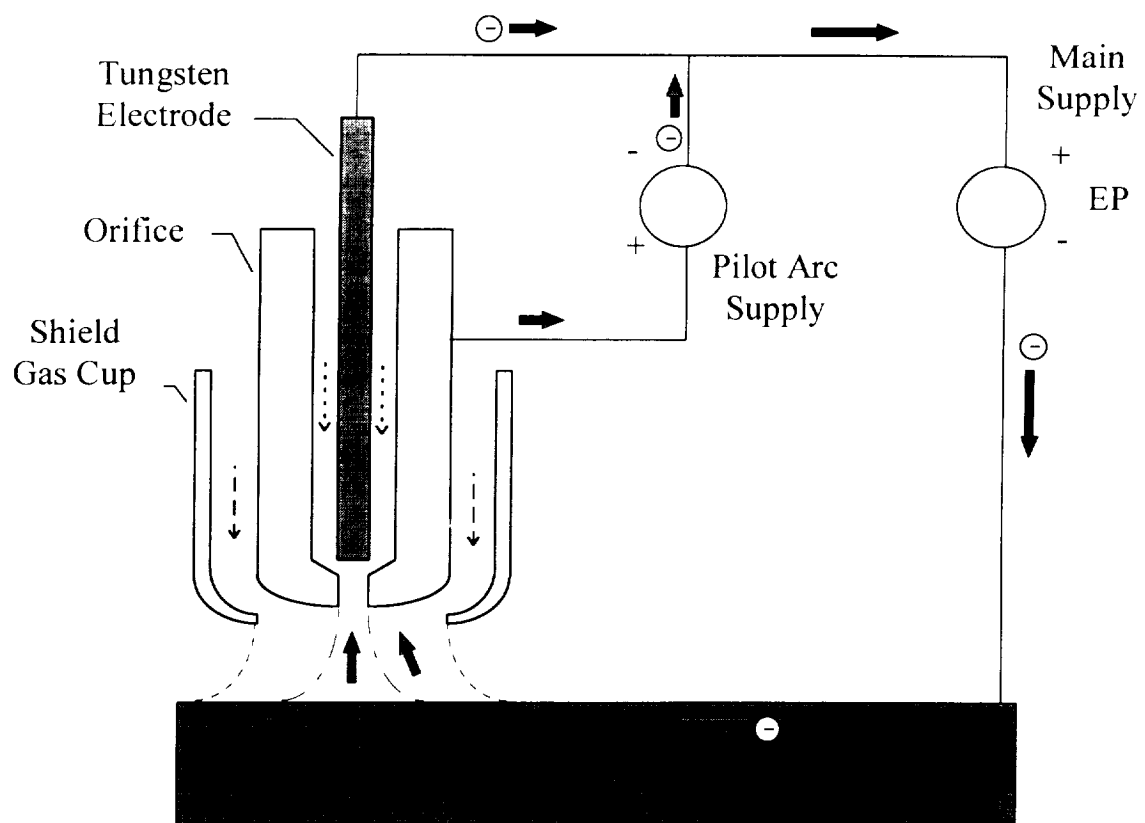


Figure 3: Current flow paths during EN operation.

In this case the main (transferred) arc current flows around the circuit, through the tungsten electrode, which is the cathode of the arc, to the work piece. Due to the

nature of processes at the electrodes, most of the main arc heat is dissipated at the work piece which is the anode. The pilot arc current is in the same direction as the main arc current in the portions of the circuit common to both. Thus the sum of the main and pilot arc current flow from the tungsten electrode. An amount of current equal to the pilot arc current must flow to the orifice and back to the pilot arc supply. The pilot arc is not a separate arc from the main arc, but is a partial current path within the total plasma arc. The deterioration studies show that this flow of pilot arc current is asymmetric, concentrated at some point between the electrode and orifice. Since the orifice is the anode of the pilot arc, it will absorb the greater amount of pilot arc heat dissipation. Although the pilot arc current is relatively small, typically of the order of ten percent of the main arc current, it does have significant effect on deterioration as was observed.

Current flow during times of EP operation is illustrated in Figure 4. In this case, the pilot arc actually runs between the work piece and the outer orifice surface, rather than from the tungsten electrode to the orifice. This is because the pilot and main arc supply voltages add in series under this condition, providing the sum of the pilot and main supply voltages across the orifice to the work piece. Since the main supply delivers a fixed current, this reduces the current flow to the tungsten electrode by an amount equal to the pilot current. Furthermore, since the pilot arc supply uses a voltage source and series resistance to control the current, the voltage across the series resistance is actually much greater during EP (because it is the sum of main and pilot supply voltages) and therefore the EP pilot current is much greater than indicated on the panel of the pilot arc source. This was confirmed by oscilloscope measurements of currents at various locations. This is actually desirable because it reduces heat load on the tungsten during EP operation when it is the anode for the main arc. It does produce extra heat load onto the orifice outer surface, which is evident from the appearance of the orifice outer surface condition after VP operation as can be seen in Figure 2.



**Figure 4: Current flow paths with EP operation.**

## Current Path Modification

These results led to the consideration of whether current paths might be modified by changes to the circuit to minimize heat deposition in the torch, especially to the electrode and inner orifice surface which are the most critical. The first experimental circuit tested is illustrated in Figure 5 which used two rectifying diodes placed in the arc circuit as shown. These diodes had no effect during the EN cycle, but forced the main arc current to run from the work piece to the orifice, rather than to the tungsten electrode, during EP. The benefits of doing this are shown in deterioration studies in Figure 6 where it can be seen that inner orifice and electrode deterioration are noticeably reduced ("torch body" as compared to "conventional"). There is still some asymmetry in electrode/orifice deterioration because of the EN pilot arc. With this configuration, the pilot arc is believed to operate continuously between the tungsten electrode and the inner orifice (rather than operating from the work piece to the orifice as for conventional VP operation).

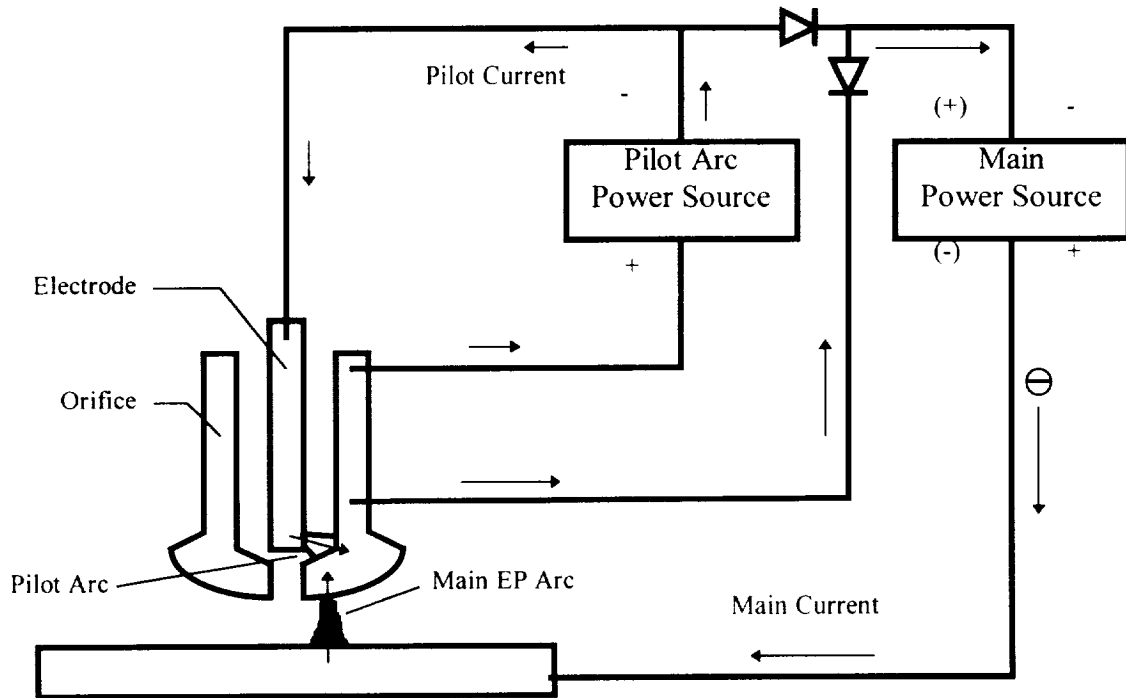
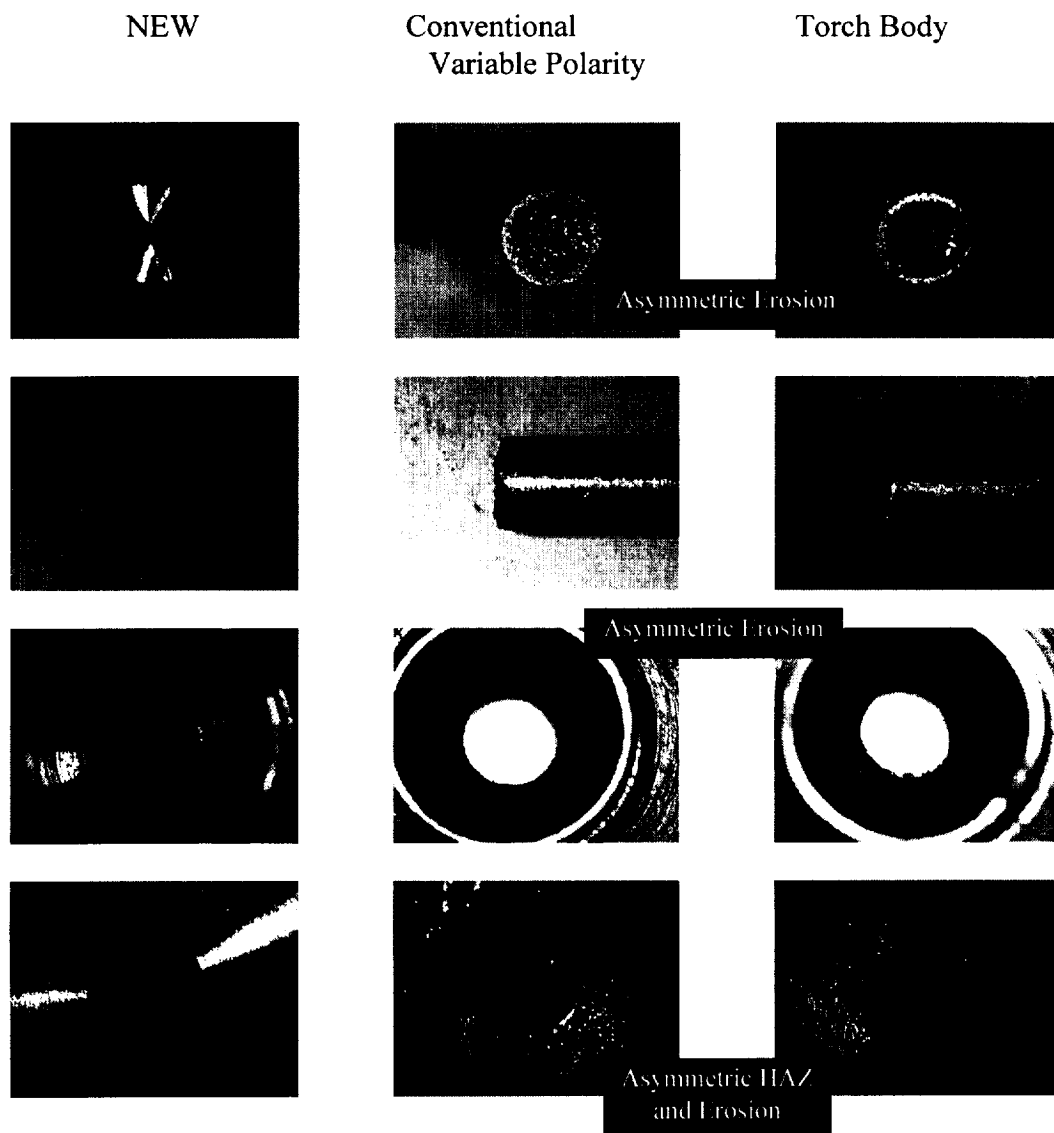


Figure 5: Current flow paths with diodes and EP operation.





**Figure 6: Electrode and orifice condition comparison.**



Another scheme utilized a second tungsten electrode external to the VPP torch as illustrated in Figure 7. For these tests, a manual GTA torch was mounted just in front of the VPP torch with the tungsten sticking into the vicinity of the plasma arc. A second shielding gas flow was passed through the GTA torch. The same diode arrangement was used, with connection to the second electrode rather than to the orifice.

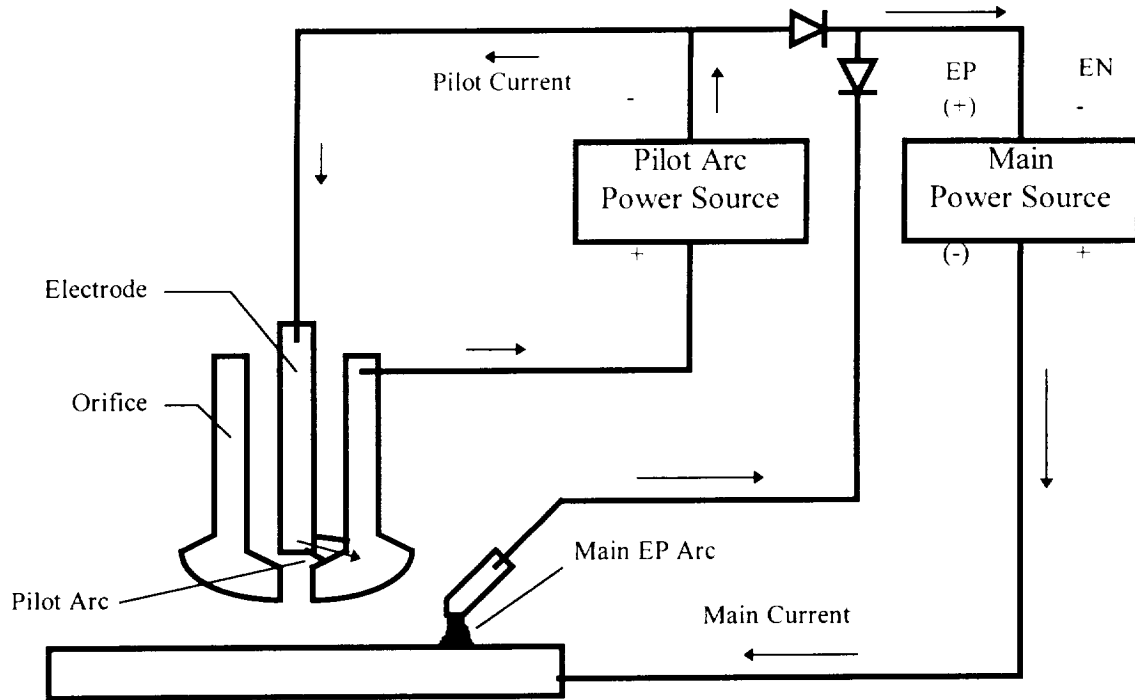


**Figure 7: Modification of current paths with a second electrode.**

The results are shown in Figure 8 where it can be seen that deterioration of the main tungsten and orifice are reduced significantly. Minimal deterioration of the outer surface of the orifice is evident, because EP current is no longer being drawn to the VPP torch. This produced the best results. In this case, the second tungsten electrode absorbed all of the EP heat, and served as what might be called a “sacrificial electrode”. This dual electrode system appears to present prospects for significant improvement in VPP torch operation in the VP mode. It not only reduces asymmetric deterioration of the torch, but also reduces the overall heat load on the torch, and should allow operation at higher welding currents. In this case, the VPP torch is in actuality only operated during the EN cycle, while the second electrode absorbs EP operation.



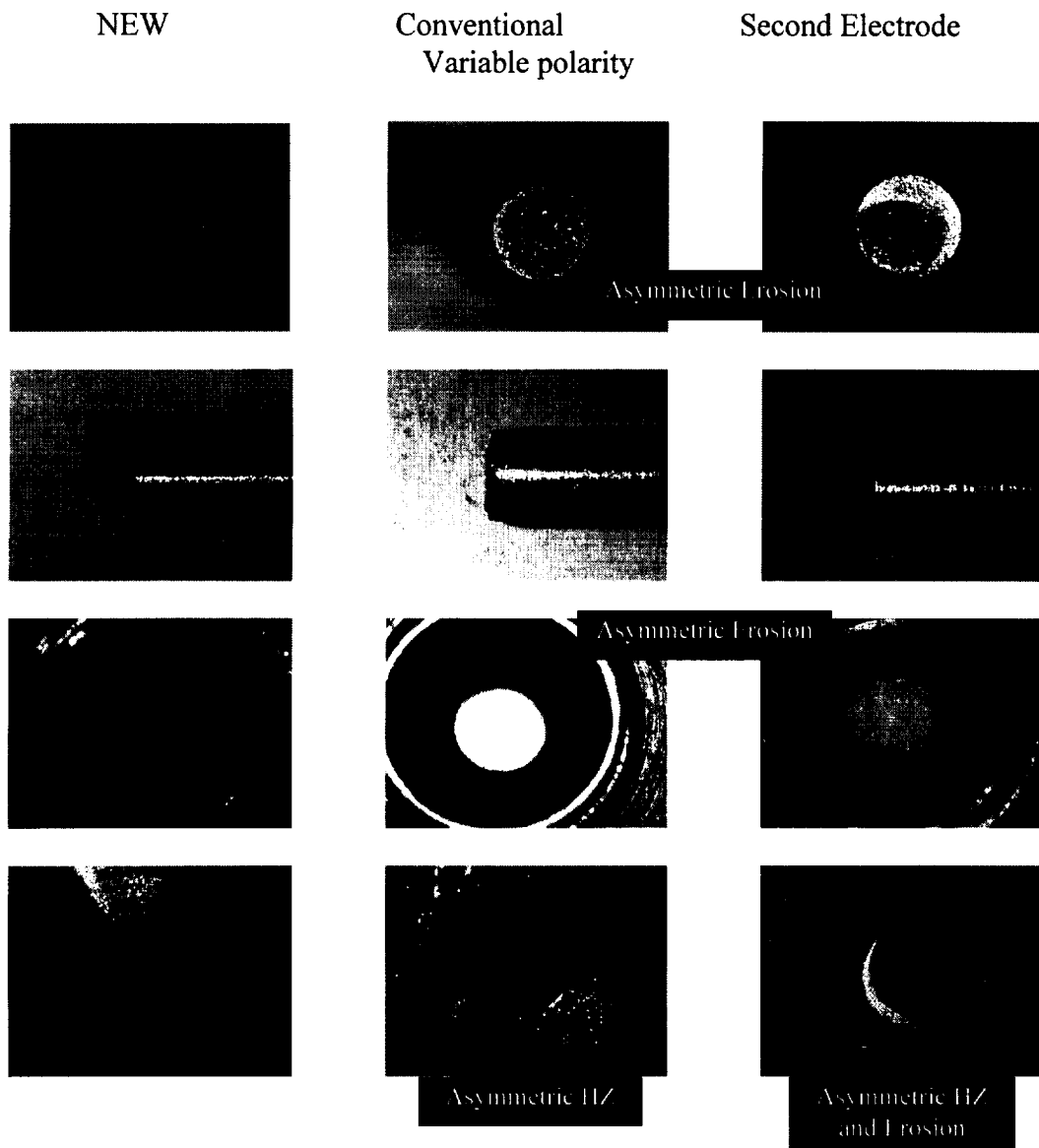


**Figure 8: Electrode and orifice condition comparison.**



Another result of decreased electrode deterioration with the modified current paths is that the use of a sharpened rather than a blunt electrode tip preparation can be considered. Tests indicated that the sharpened tip seemed to be less susceptible to arc skew in the absence of EP current flow to the electrode. It is thought that the tapered tip on the electrode produces a more uniform flow which is less affected by minor misalignments of the electrode/orifice geometry, as well as the pilot arc operation. Since the heat load on the electrode is eliminated during the EP cycle, the tip will retain its pointed shape. With conventional VP, the EP cycle quickly deforms the pointed tip shape due to the high heat input.

Limited testing of the two systems for modifying current flow paths was conducted for aluminum welding. In the tests that were conducted, both circuit configurations worked and seemed to provide satisfactory cathodic cleaning action. The configuration using the orifice as the EP anode was the simplest to implement, requiring only the diode circuit be incorporated into welding lead. This configuration did result in more deterioration of the orifice outer surface, which may be a problem for long duration welding. The second electrode system is complicated by the need for incorporating the second electrode and shielding gas supply. It also will produce some interference with a wire feed system. However, it was most effective at eliminating electrode and orifice deterioration. The two electrode system is deserving of an effort towards an integrated design of the second electrode feature into the VPP torch, and extended testing for evaluation to practical application.

### **Conclusions and Recommendations**

Arc skew occurrence has been primarily identified with asymmetries in the electrode and orifice geometry. The plasma is observed to skew in the direction of any asymmetric constriction in the flow. These asymmetries may result from initial misalignments, operation of the pilot arc, or deterioration of the electrode and orifice geometry during long duration operation. The pilot arc contributes to skew by producing an inherent asymmetry in the plasma flow, and also by contributing to asymmetric deterioration of the electrode and orifice geometry. Current flow paths during EN and EP operation dictate the points of heat dissipation and deterioration of electrode and orifice surfaces. Modifications to current flow paths by incorporation of rectifying diodes in the circuit, and by the use of a second, sacrificial electrode, were found to be possible solutions to heat dissipation and deterioration of electrode and orifice surfaces. Incorporation of these ideas into the torch and welding circuit design should reduce the arc skew tendency and increase the current capability of the VPP system.





## 1. INTRODUCTION

Plasma Arc Welding (PAW) is an arc welding process that is similar to Gas Tungsten Arc Welding (GTAW) but is often compared to high energy density processes such as Electron Beam and Laser Beam welding due to its deep penetration capability [Ref. 1]. PAW differs from GTAW in that the plasma arc is constricted by a copper nozzle to produce a high velocity plasma jet. PAW is generally operated in DC electrode negative (DCEN) mode when welding ferrous material and related alloys, but it also can be operated in a mode called variable polarity which is referred to as Variable Polarity Plasma Arc Welding (VPPAW) [Ref. 2]. Variable polarity is the term given to a variation of the AC waveform that can be achieved by combining two DC power supplies using solid-state technology to produce an alternating square-wave current waveform.

The National Aeronautics and Space Administration (NASA) has adopted VPPAW for the fabrication of the External Tanks (ET) of the Space Shuttle for its ability to weld thick sections of aluminum and aluminum alloys in a single weld pass. Welds made with the VPPA process have shown significantly less porosity and distortion compared to that obtained with multi-pass GTAW process [Ref. 2, Ref. 3, Ref. 4].

The VPPAW process has been widely accepted, and fabrication of the ET with VPPAW has proven itself in the production environment. Improvements in torch design

have extended the welding time capability of the process in order to meet the requirements for long duration welds necessary for the ET application. In spite of the fact that improvements to the torch design have led to enhanced performance, the plasma arc operation is not thoroughly understood and presents some unresolved operational problems.

One problem with the current VPPA process has been the tendency for the plasma arc to blow or skew as it transfers to the work piece. Arc skew often occurs after long periods of welding and it is believed to be at least partially associated with the development of asymmetry between the electrode and orifice due to arc induced deterioration of the surfaces. Other sources have been proposed as well. The skew, which is a chronic problem, leads to the formation of asymmetry in the weld pool and a resulting weld defect which is in the form of an unacceptable undercut at the toe of the weld (Figure 1) [Ref. 3].

Currently, the effects of arc skew are resolved by rotating the welding torch by manual or automatic control. This rotation ensures that the arc skew is aligned with the weld motion direction, minimizing weld defects. The unpredictable nature of the arc skew formation results in the requirement for continuous manual monitoring of the welding process. A solution to the arc skew problem would reduce the need for manual monitoring and operator intervention.

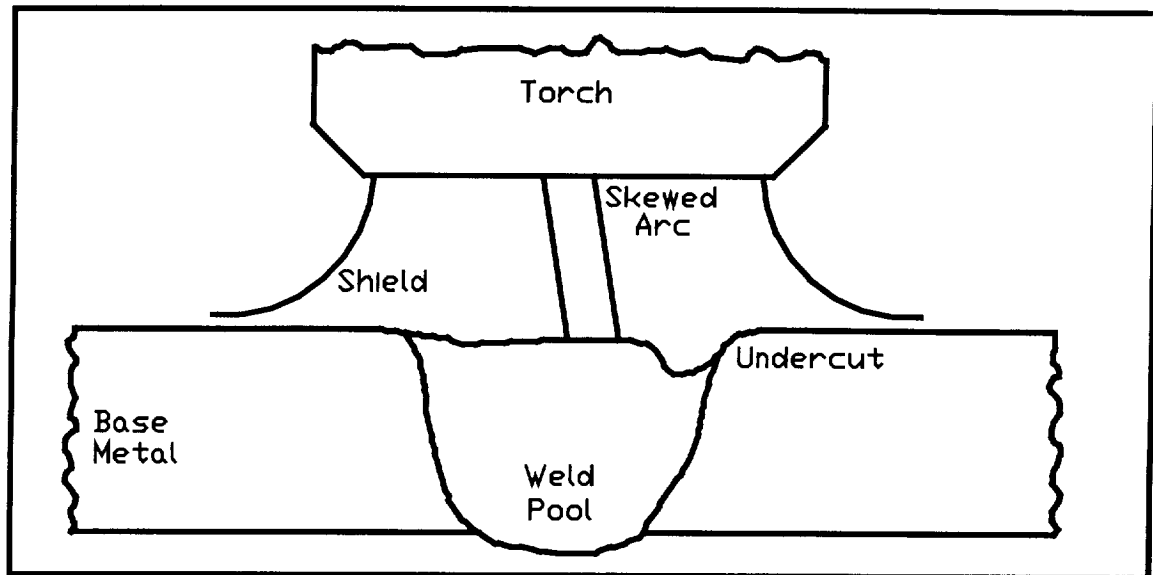


**Figure 1. Skewed Arc with the Chronic Problem of Weld Undercut.**

Another limitation of the VPPA process is the torch design which allows 100% duty cycle only up to 300 amperes. Extension of the torch carrying current capacity is sought to allow for even thicker materials to be welded in one pass. Design parameters for the torch are not well understood since previous torch development has been on a trial and error basis. A more systematic and scientific approach to understanding the VPPA process is sought in order to provide insight for VPPA process and equipment improvement.

This research examines the VPPAW process, and the arc skew phenomena in particular, as they relate to VPPA torch capacity and design. Experimental and analytical methods have been used to address several research objectives of understanding the

source of arc skew and suggesting ways to improve torch operation. This report will detail experimental and analytical investigations.

## **2. BACKGROUND**

This chapter presents a historical evolution of the application of the VPPA process. The basic principles of PAW and VPPAW are examined followed by a review of recent NASA research concerning VPPA process characteristics. Finally, an overview of the arc skew phenomena issues is presented.

### **2.1 Historical Background**

In order to understand the current state of VPPA technology, the historical evolution of the VPPA process is useful (O'Brien [Ref. 5] and Nunes, A. C. [Ref. 6]). Since the beginning of the century, when Schonherr developed a gas vortex stabilized device in 1909, interest in studying plasma arcs has accelerated and various applications have been developed. In 1922, Gerdien and Lotz developed a water vortex arc-stabilizing device which was used for experimental purposes only. It was not until 1953, when Gage observed similarities between the electric arc and fuel gas arc that the modern plasma arc torch was developed.

The development of the Plasma Arc process is dated at 1955 when Linde Corp. commercialized a plasma torch for cutting applications. Later, in 1965, Linde developed

a Plasma Arc welding facility for Westinghouse Electric for the fabrication of steel rocket cases. The PAW process improved production efficiency by achieving deeper penetration welds and reducing the number of weld passes required by approximately 50%. This same year, Thermal Dynamics Corp. used reverse polarity PAW on aluminum. Another advancement made during the 1960's was the incorporation of Variable Polarity keyhole welding of aluminum by VanCleave at Boeing Corporation. This process was able to achieve deeper penetration than the reverse polarity PAW of aluminum.

The 1970's led to the development of VPPA. In 1972, a square-wave power supply by Sciaky Corp. showed promising results in the search for improvements to the Plasma Arc welding of aluminum. Two years later, Hobart Brothers Corp. built a VPPA power supply for Boeing similar to the Sciaky power supply.

In 1979, NASA Marshall Space Flight Center received a VPPAW system to evaluate the system performance on the ET application. After six months of studying the VPPAW system, NASA decided to partially replace the GTAW system for the reduction of distortion and weld time achievable with VPPAW.

VPPAW represented an improvement over the former GTAW system. Some equipment modifications were designed and implemented in order to enhance application and process performance. For example, in 1980, a digital program controller was added to the system to reduce the need for operator intervention. Due to its success, a second controller for the VPPAW system was delivered to the production facility in 1981. Two

years later, a contract was awarded to B&B Precision Machine for the development of a new torch that could overcome problems like electrode centering and coolant fluid leakage associated with O-rings in the existing torch assembly. A patent was granted relative to this new torch development in 1986 [Ref. 7]. Successive improvements, including the development of a smaller torch size for robotic applications and for accessing small spaces, have followed in order to accommodate the ET production needs.

## 2.2 PAW

PAW is similar to Gas Tungsten Arc Welding (GTAW) in that both welding processes produce a molten weld pool by heat transfer from an electric arc between a non-consumable tungsten electrode and the workpiece. The main difference is that the arc in PAW produces a high temperature, high velocity directional plasma jet. The plasma jet is produced by the constricting effect of a copper nozzle in combination with the introduction of cold plasma gas. When the cold plasma gas is introduced into the path of the hot arc, gas expansion occurs. The gas particles are accelerated through the orifice towards the workpiece in order to maintain the conservation of mass, resulting in a high velocity jet. The main advantage of the high velocity plasma jet is the depression of the weld pool surface, allowing for deeper penetrating welds to be made with the PAW process.

Figure 2 presents a comparison between GTAW and PAW by showing the main components of each process [Ref. 5, Ref. 8]. Among the added features of the PAW

process are a constricting nozzle, and an added shielding gas in addition to the plasma gas. The electrode in PAW is recessed inside a constricting copper nozzle. The second gas flow has been added to the torch configuration as an auxiliary shielding source to avoid weld metal contamination.

### **2.2.1 Arc Modes**

The two arc modes used in PAW are the non-transferred arc mode and the transferred arc mode. Figure 3 shows these two modes of arc transfer for the PAW process. The non-transferred arc mode is characterized by having the power supply connected between the electrode and the constricting nozzle. This arc transfer mode is used mostly for plasma spraying or heating non-conducting materials.

The transferred arc mode is characterized by having the power supply connected between the electrode and the workpiece. The transferred arc mode is used for the welding of metals. Note that in both cases, the current (electrons) will flow from the electrode which is the negative connection, to the other connection which is positive. This is DCEN or so called straight polarity [**Ref. 2, Ref. 5, Ref. 9**].



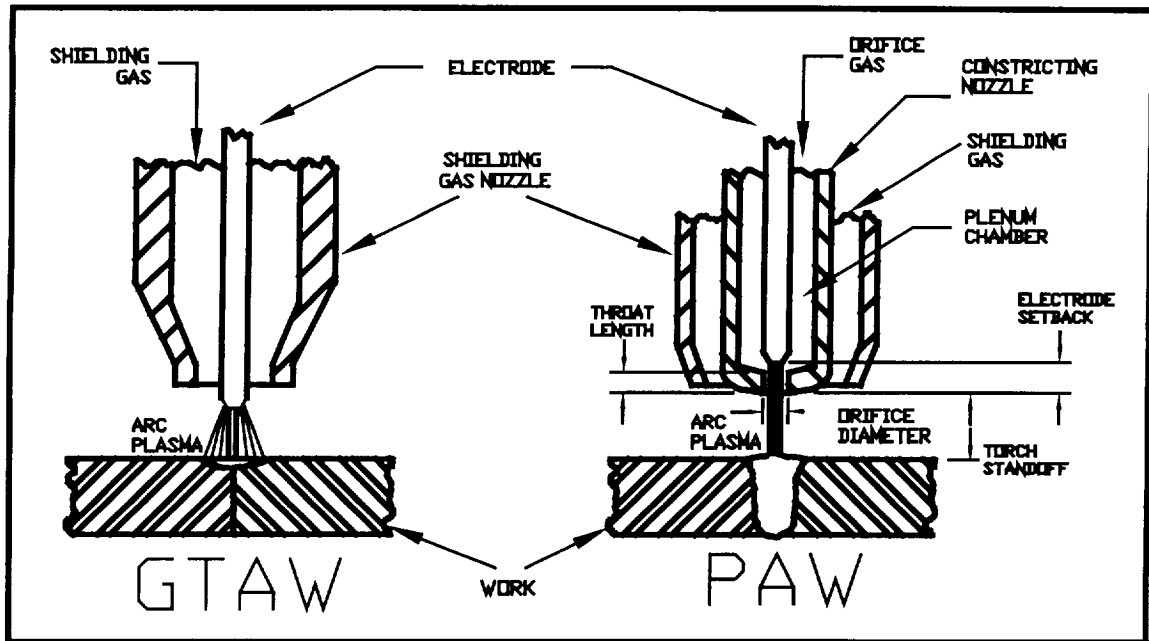


Figure 2. Comparison Between GTAW and PAW.

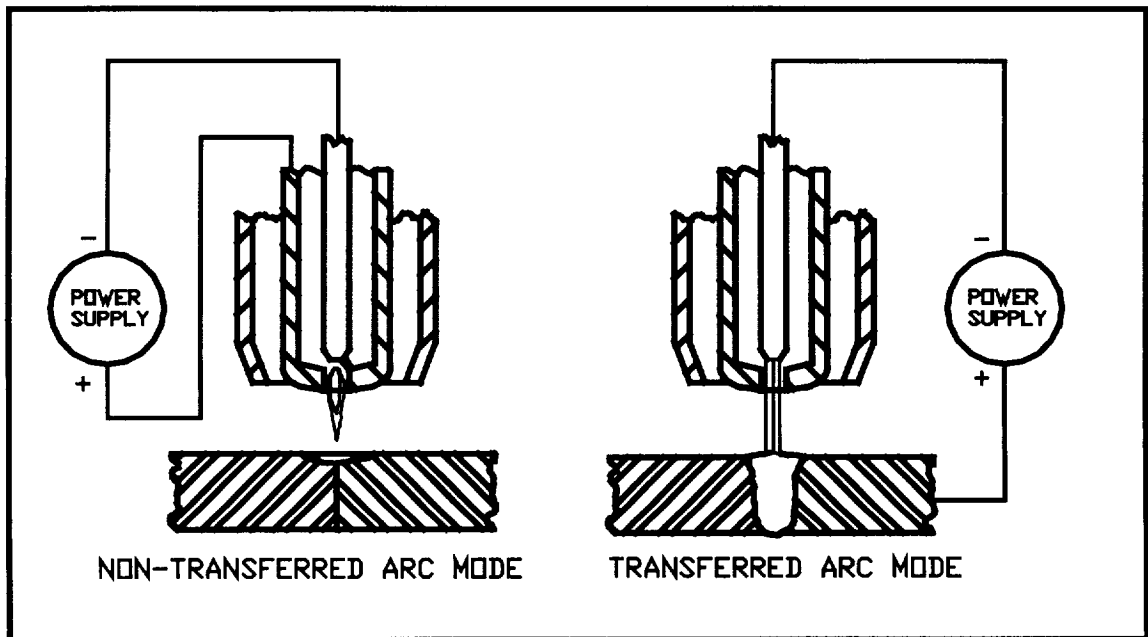


Figure 3. PAW Arc Transfer Modes.

### 2.2.2 Operating Modes

The PAW process with a transferred arc has two distinct operating modes, called the melt-in mode and the keyhole mode. The melt-in mode, generally used at current levels of 20 to 80 Amps, attains only partial penetration on heavy sections. At high current levels (100 to 250 Amps), the keyhole mode is predominant and full penetration of heavy sections can be achieved. Figure 4 shows schematics of the melt-in and the keyhole modes. As can be seen in the figure, the keyhole mode can achieve full penetration in one pass while the melt-in mode is much like conventional GTAW and requires multiple passes [Ref. 2, Ref. 5].

The melt-in mode weld pool is produced by surface heating of the materials being welded. Conduction of the surface heat accounts for the penetrating potential of this mode of operation. On the other hand, the keyhole mode is achieved by a displacement action of molten weld metal producing either a depression of the weld pool or a hole through the thickness of the material, generally referred to as the keyhole. As welding progresses, weld metal is melted from the front of the keyhole. The weld metal then flows around the sides of the keyhole to the back of the weld, closing the keyhole.

Generally, direct-current (DC) constant-current (CC) power supplies are used for PAW. DC power supplies are used for welding materials such as stainless steels, carbon steels and alloy steels. When welding aluminum and aluminum alloys, alternating current (AC) using alternating power supplies can be utilized as well. New developments

have introduced variations to the PAW process. These variations include pulsed-current PAW, hot-wire PAW, micro plasma low-current precision PAW, and Variable Polarity Plasma Arc (VPPA).

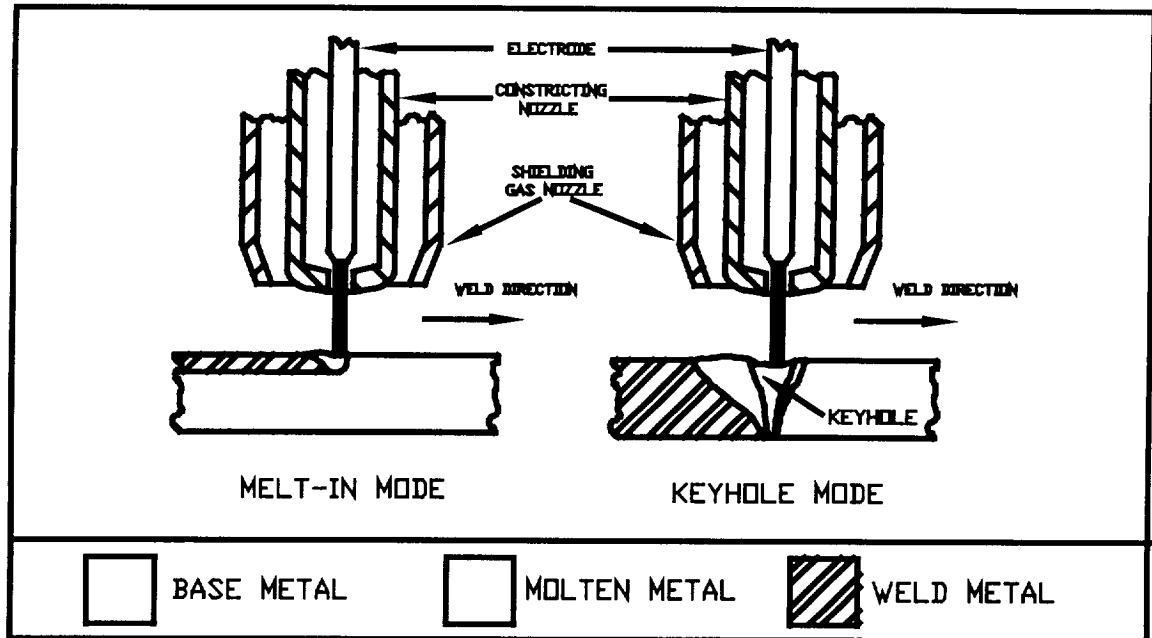


**Figure 4. Schematic of the Melt-in and Keyhole Modes of Operation.**

### 2.3 VPPAW

The VPPA variation of the PAW process was developed by the aerospace industry. One of the purposes for its development was for its potential to weld thicker sections of aluminum in a single pass [Ref. 9].

VPPA power supplies using solid-state technology enhance the welding of aluminum by using a square current waveform rather than a conventional AC waveform.

A typical square wave VPPAW current waveform is shown in Figure 5. This waveform is superior to the AC waveform for welding aluminum since current amplitude and time settings can be controlled independently. In addition, the square nature of the VPPAW current waveform provides a degree of stability to polarity changes. As in PAW, the straight polarity (DCEN) cycle of the VPPA process provides the penetrating action of the process. The reverse polarity (DCEP) of the VPPA process provides the cathodic etching needed to break up the tenacious oxide layer formed on aluminum, therefore, allowing for a steady flow of the molten metal [**Ref. 4, Ref. 5, Ref. 9, Ref. 10, Ref. 11**].

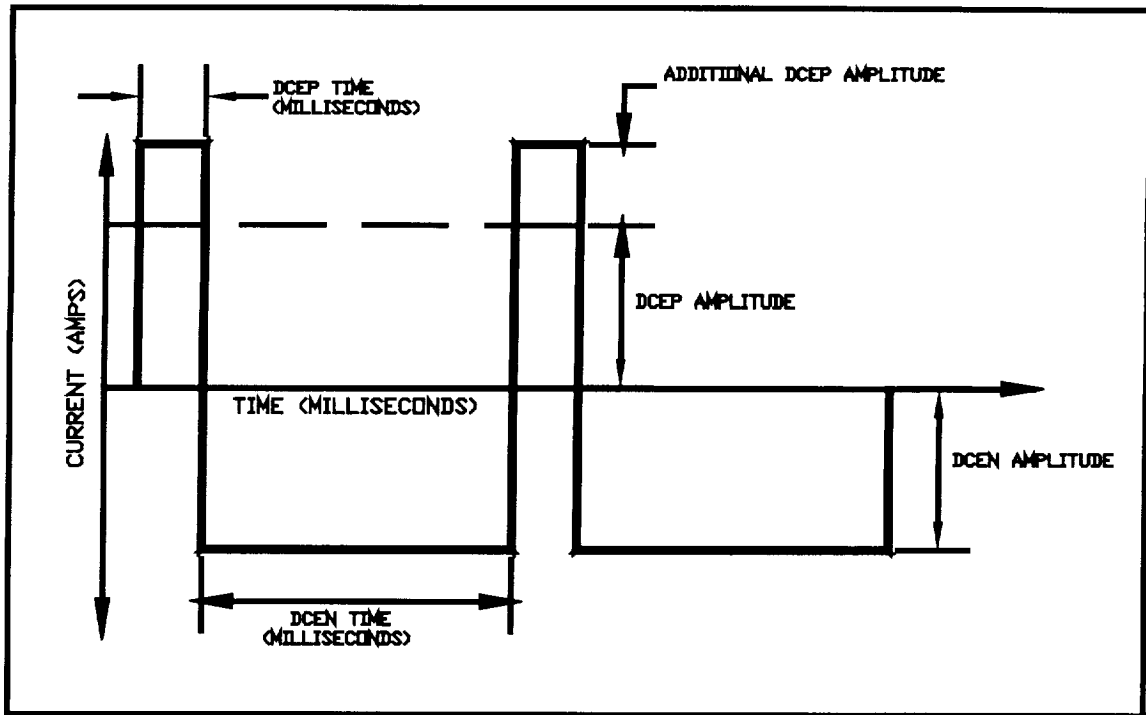


**Figure 5. VPPAW Current Waveform.**

Cathodic etching, also known as cathodic cleaning, is the main advantage associated with the VPPAW process when welding aluminum or aluminum alloys since it can reduce base metal preparation. Aluminum and aluminum alloys are characterized by a tenacious oxide surface layer that disrupts metal flow. In order to improve metal flow, oxide removal techniques have been employed such as chemical cleaning and mechanical cleaning. These are expensive and time consuming. The EP cycle of the VPPAW process provides cathodic cleaning of the oxide layer at the point of welding, improving metal flow characteristics within the weld. This reduces or eliminates the need for base metal preparation prior to welding.

Many theories have been proposed to explain the mechanisms of cathodic cleaning. For example, thermionic emission, ion bombardment and sputtering are few of these theories, but one theory in particular, dielectric breakdown, has been proposed as the predominant mechanism behind oxide removal during the reverse cycle of the VPPA process. Dielectric breakdown of the oxides occurs when positive charges build up on the surface of the oxide near the arc. This is followed by glowing spots of exploding oxides accompanied by audible noises from the reverse polarity cycle [Ref. 10, Ref. 12].

### **2.3.1 Arc Initiation Technique**

Arc initiation techniques for the VPPAW process are limited due to the electrode being recessed in the torch. This does not permit touch-start techniques to be utilized. Instead, a high voltage, in the form of a high frequency or a high voltage DC pulse, is used to break down the gap between the electrode and the nozzle so that a non-transferred arc (pilot arc) can be initiated. The circuit is shown in Figure 6. After the break down, a pilot arc power supply maintains the pilot arc current. The welding equipment is designed to shut-off the high frequency once the pilot arc is started. When the main power source is energized, the transferred arc is initiated between the electrode and the workpiece. The pilot arc may be turned off in conventional PAW, but in VPPAW, the pilot arc source is often left on to stabilize the plasma arc during polarity switching [Ref. 5].

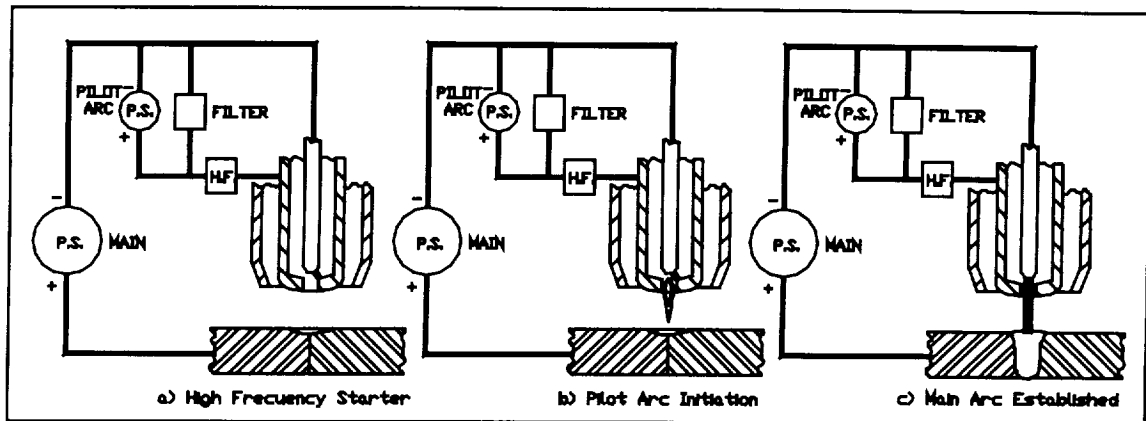


Figure 6. Arc Initiation Sequence.

## 2.4 Recent VPPAW Research

In the last fifteen years or so, research on VPPAW has been primarily done by individuals involved in the development of equipment for the aerospace industry. Welding parameters for a variety of aluminum alloys have been developed and weldability studies have been performed. Literature relating to the issues of welding parameters and weldability are relatively numerous. Literature describing the physical behavior of the process and its characterization is much more limited. Therefore, most of the information about VPPAW lies with those who employ the process on a regular basis.

Some recent articles have been published about VPPAW. For example, a study by Torres, et. al. [Ref. 3] explains the formation of asymmetric undercutting in the weld metal. In addition, an article on NASA Tech Briefs magazine in June 1995 claims performance improvements of the welding torch by adding a swirl ring in the plenum

chamber [Ref. 13]. Both of these articles address the important problem of arc skew and the resulting undercut.

#### **2.4.1 Asymmetric Undercutting**

It has been observed that occasionally, the VPPA plasma jet deflects from the torch center line. This arc skew results in asymmetric undercutting. Once arc skew develops, the heat distribution into the weld pool will be higher towards the side to which the arc skews. This generates greater spatial surface tension gradients on the hotter side of the weld pool producing faster Marangoni convection on that side. Changes in weld pool velocities can induce undercut by Bernoulli and surface tension effects accounting for a depression in the weld pool side with faster convection [Ref. 3].

Correction methods have been employed to eliminate weld undercut. For example, rotation of the welding torch so that the arc skew is aligned with the direction of travel can eliminate the undercut problem. Replacement of the electrode and orifice can also eliminate arc skew and its associated undercut. Despite these offered solutions, no systematic study has been done that looks at the mechanics behind arc skew to determine whether torch or process variations might mitigate its occurrence.



### 2.4.2 Possible Sources of Arc Skew

Based on field observations and laboratory tests, possible sources of arc skew have been offered by practitioners. This information on potential sources of arc skew was useful for the definition of experiments for the study of skew. For the most part, these ideas are unpublished and have been obtained through personal discussions.

#### *Electrode Tip Asymmetries*

Arc skew could occur due to a misalignment of the electrode with respect to the orifice or vice versa. This type of misalignment could introduce an initial asymmetry in the torch configuration that, if not accounted for, could deflect the plasma jet. Improved torch design has addressed increasing the precision of centering of the electrode with the orifice.

At the current levels used in aluminum welding applications, it is known [Ref. 14] that current conduction in the electrode (cathode) during the straight polarity cycle occurs in the spot mode. The electrode during this mode is characterized by scattered molten spots through which most of the welding current is conducted. Conduction of the welding current through these spots is often erratic and transient, with these spots moving all over the electrode tip surface.

It is also known [Ref. 1] that when the arc is operating in reverse polarity, the electrode is exposed to higher heat loads, causing melting of the electrode tip. The erratic spotting during straight polarity, and the higher heat loads encountered in reverse

polarity, suggest that uneven erosion of the cathode tip could cause an asymmetric shape of the cathode tip, resulting in possible deflection of the plasma jet.

#### ***Uneven Attachment Of A Secondary Arc***

Current conduction by a secondary arc such as the pilot arc could be present between the electrode and the orifice. In addition, double arcing could be present between the orifice and the work piece. Either current conduction path is likely to be asymmetric. Non-uniform cooling of the orifice and electrode could lead to changes in the pressure distribution of the plasma arc. This non-uniformity of the pressure distribution could cause separation of the flow exiting the copper orifice resulting in loss of plasma arc symmetry.

#### ***Erosion Of The Orifice's Inside Surface***

Erosion of the orifice's inside surface could be produced by the erratic nature of the spot mode current conduction. In this case, the uneven erosion could be associated with a secondary arc discharge (pilot arc) between the electrode and the orifice.

#### ***Heat Load Distribution On Orifice Wall***

Uneven cooling or heating of the orifice could cause an asymmetry within the torch, affecting the plasma flow and the heat distribution of the arc issuing from the orifice. Causes of this uneven cooling or heating could be related to non-uniform

shielding or plasma gas flows, uneven attachment of secondary arcs, and cathode and/or orifice erosion.

#### ***Non-Uniform Entrainment Of Ambient Air***

Another possible source of arc skew could be the result of air being pulled into the plasma jet due to changes in velocity within its surroundings. This entrainment of air also known as entrainment. If the entrainment were non-uniform, the jet could be deflected, resulting in arc skew.

#### ***Current Paths Between The Electrode, Work Piece And Orifice During Straight And Reverse VPPA Cycle***

If the current path between the electrode and the orifice during the reverse cycle produces an asymmetric discharge, arc skew could occur. The electrode negative (EN) or straight polarity half of the cycle involves a transferred arc between the electrode and the work piece. The electrode positive (EP) or reverse polarity in general is a discharge between the work piece and the electrode, however it could be possible for a discharge between the work piece and the orifice to be in operation during this polarity. The path of the current might influence the degradation of the electrode and the orifice causing asymmetries that could result in arc skew.

#### ***Creep-Induced Changes In Orifice Or Electrode Geometry***

Creep occurs when a material is exposed to thermal heat cycles. As a result of creep, dimensional changes within the electrode and the orifice could occur. The effects of creep in the cross-sectional areas of the torch components could result in a deflected jet when asymmetries are introduced. In addition, creep could reduce the pressure of the plasma jet by reducing the cross-sectional area decreasing the amount of plasma gas flow through the orifice.

## **2.5 Summary**

A historical background of NASA's application of the VPPAW process to the External Tanks of the Space Shuttle and the basic principles of PAW and VPPAW, one of the variations to the PAW process, have been presented. Although VPPAW has provided numerous advantages over GTAW, some problems remain. This research deals with one of these problems, the deflection of the plasma jet, which has been observed to cause asymmetric undercutting at the toe of the weld.

Weld undercut has been associated with uneven surface tension developed by uneven heat distribution due to arc skew. The study of some possible sources to arc skew provides information that can later be used to find a solution to the problem. Primarily, asymmetries within the electrode and orifice configuration are suspected to be the source of the plasma jet deflection. These asymmetries can be due to erosion, uneven heat load distribution, and current paths.

### **3. EXPERIMENTAL METHODOLOGY**

This chapter presents the methodology used to experimentally investigate the VPPAW process. This will include the experimental approach, a description of the experimental apparatus, and an overview of the experiments conducted.

#### **3.1 Approach**

A three stage experimental approach has been designed to study VPPA operation and especially the phenomenon of arc skew and its possible solutions. In the first stage of research, the VPPAW process was studied in order to gain fundamental qualitative and quantitative knowledge about the process. This phase of the research was intended to provide a better understanding of the process by systematically relating welding variables to tangible parameters such as arc pressure and heat deposition. These results were used to verify the analytical model of the plasma arc.

The second stage of research focused on the phenomenon of arc skew. Arc skew was studied by simulating the possible sources of arc under controlled laboratory conditions. Simulation of the arc skew was achieved by introducing asymmetries into the torch components. By doing so, it was possible to determine which potential causes of

arc skew were most influential. Arc skew was recorded by video monitoring of the plasma arc.

In the final stage of experimentation, possible solutions to arc skew were tested based on the knowledge gained from the other experimental phases. The experiments for the first and second stages of the study will be described in detail after a discussion of the experimental apparatus. Experimentation and results for the final stage are presented in Chapter 6.

### **3.2 Experimental Apparatus**

In order to execute the experimental approach, a laboratory setup of the VPPA process with related instrumentation and video equipment was used. The experiments, which took place at The Ohio State University Welding Engineering laboratories, were designed around the VPPAW system shown in Figure 7. This section presents the VPPAW setup, the instrumentation and the video equipment as well as additional procedures and equipment utilized for another phase of research dealing with the arc skew phenomena.

### 3.2.1 VPPA Equipment

Figure 7 illustrates the basic VPPAW equipment setup. The welding power supply shown on the left portion of Figure 7 controlled most of the welding parameters except for those controlled by the plasma console. The plasma console received electric power, gas and coolant, and delivered them to the plasma torch. It also controlled the pilot arc parameters. Figure 7 shows the gas, electrical, and cooling connections between the main components of the VPPAW equipment.

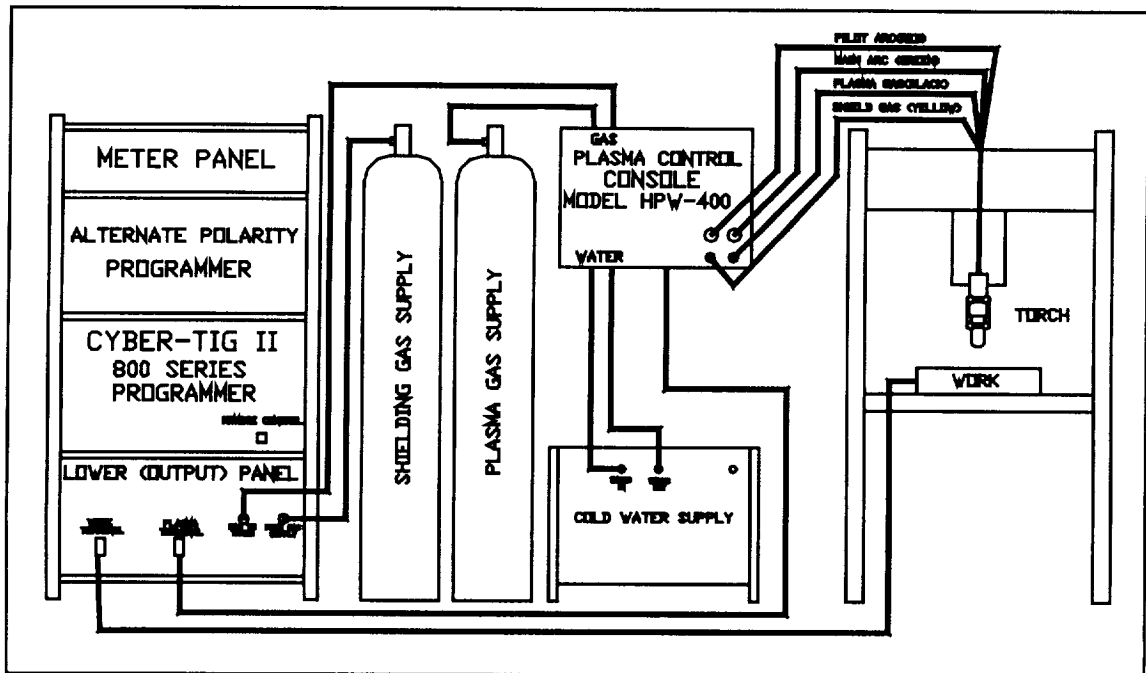


Figure 7. VPPAW Equipment Setup.

A Hobart model VP-300-S Variable Polarity welding machine, pictured in Figure 8, was used for this study. This power source could deliver a constant current output of 3 to 299 amperes at a voltage of up to 50 volts for each polarity. When running in variable polarity mode, the power source could deliver a additional current of 5 to 99 amperes to the electrode positive cycle above that for which the EN cycle was set [**Ref. 16**].

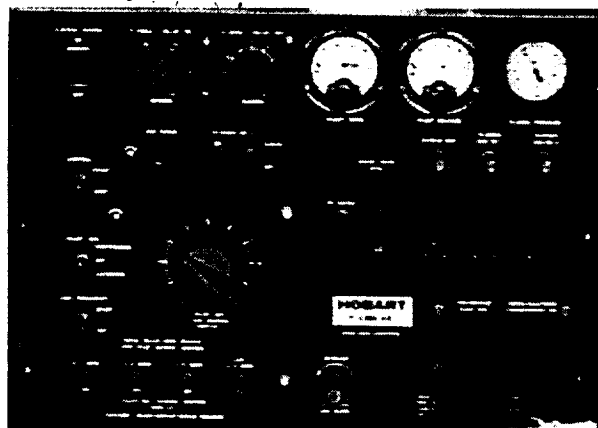
The welding power supply was configured in a four panel power source unit. An alternate polarity programmer panel (Hobart Cyber-TIG II) controlled polarity switching, additional reverse current, and straight and reverse polarity durations. An output panel contained the welding terminal connections. Schematics of the four panel power source unit can be found in equipment manuals [**Ref. 16, Ref. 17, Ref. 18**].

Figure 9 shows a photograph of the plasma console. The plasma console controlled the high frequency, the pilot arc, plasma and shielding gas flows, and coolant flow. Four hoses from the plasma console were connected to a B&B HEC-300A plasma torch shown in Figure 10. One hose delivered the welding current as well as the coolant flow, while a second hose returned the coolant fluid and completed the pilot arc circuitry. The other two hoses delivered the plasma and shielding gases [**Ref. 19**].





**Figure 8. VP-300-S Variable Polarity Welding Machine.**



**Figure 9. Plasma Console.**



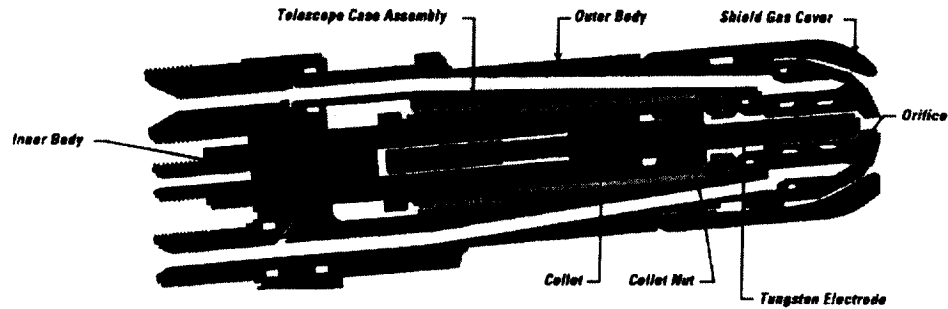


**Figure 10. Cutaway of B&B Plasma Arc Torch.**

The B&B plasma torch (Figure 10) was developed in the early 1980's as a collaborative effort between B&B Precision Machine and the Materials and Processing Laboratory of NASA Marshall Space Flight Center, replacing an older Hobart VPPA torch design. The B&B torch was designed to overcome electrode alignment and sealing problems with previous torches. Some of the key features of the B&B torch are a self-centering electrode design, repeatable electrode setback adjustment, hermetic sealing, 300 Ampere continuous operating capability in the VP mode, and 360 Ampere continuous capability in the EN mode [Ref. 7].

For most experiments in this work, the welding torch was operated in the flat position over a chilled copper block. A diagram of the chilled copper block with its dimensions is shown in Figure 12. Some experiments were performed in the flat position on aluminum samples, while others were done in the vertical up position, as is normal for the process. Figure 11 shows the vertical fixture used for positioning the aluminum

samples. In the flat position, various clamps were used to hold a variable height positioner, with pre-drilled tapped holes in place to restrain a fixture or a copper chilled block in the flat position where the plasma arc was run. Figure 13 shows the variable height positioner used to set various standoff distances.

The welding torch was mounted on the carriage of a Superior Slo-Syn stepper motor which controlled the vertical motion. Manipulation of the welding torch was done from a computer which controlled a side beam type carriage, pictured in Figure 14, with capabilities to move in x, y, and z directions [Ref. 15].



**Figure 11. Vertical Fixture.**

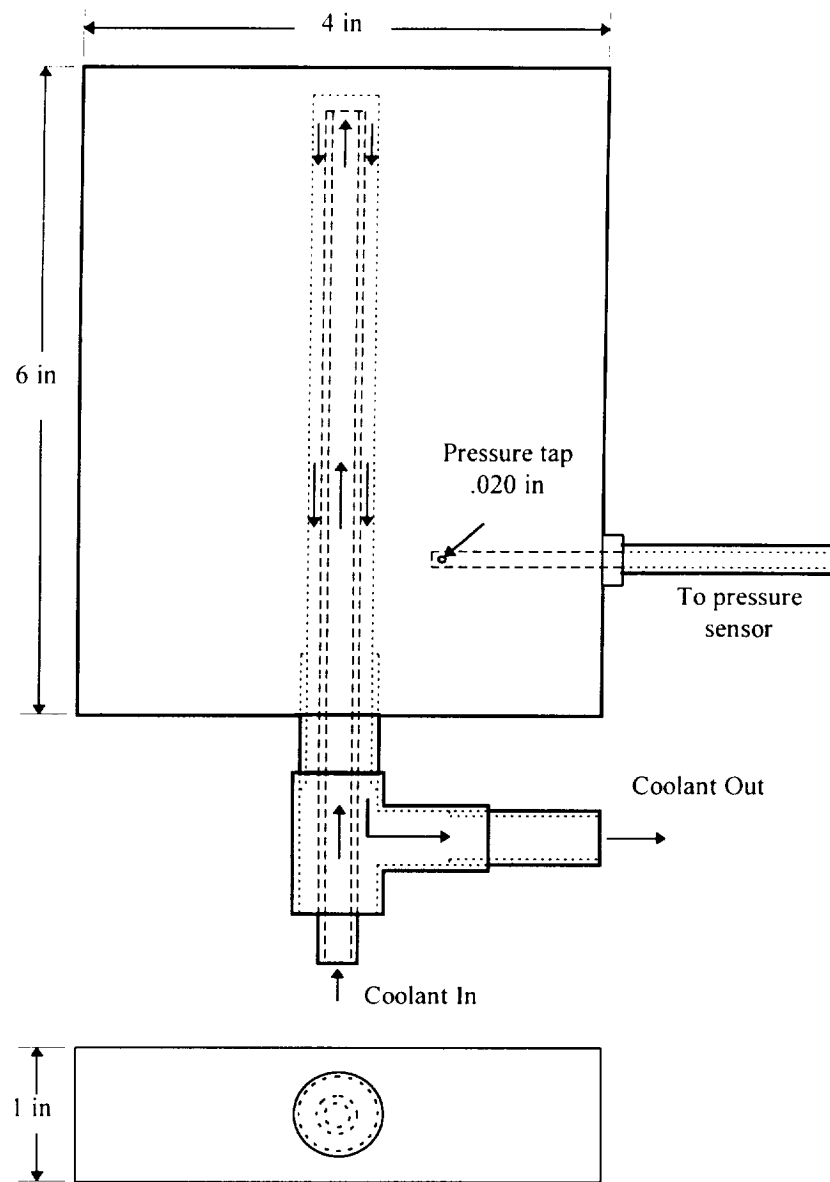


**Figure 12. Chilled Copper Block Diagram.**

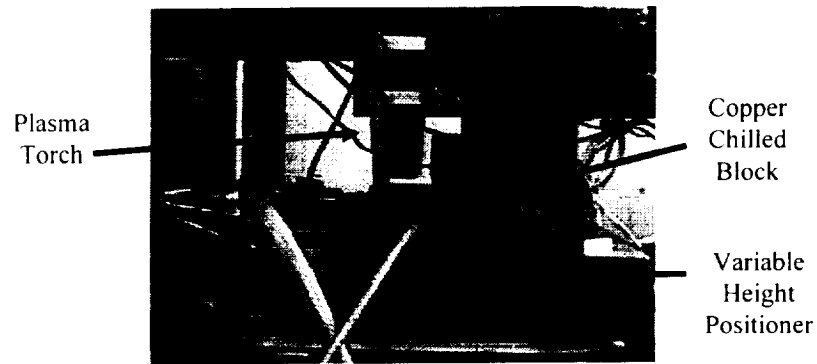


**Figure 13. Variable Height Positioner.**



**Figure 14. Side Beam.**

### **3.2.2 Instrumentation**

Figure 15 illustrates the computerized instrumentation which was utilized to measure the welding parameters, and to perform arc pressure and calorimetric measurement studies. A data acquisition system was used to gather information from

various transducers. Figure 15 illustrates the instrumentation system and the connections between the main power and pilot arc power sources to the plasma torch and workpiece.

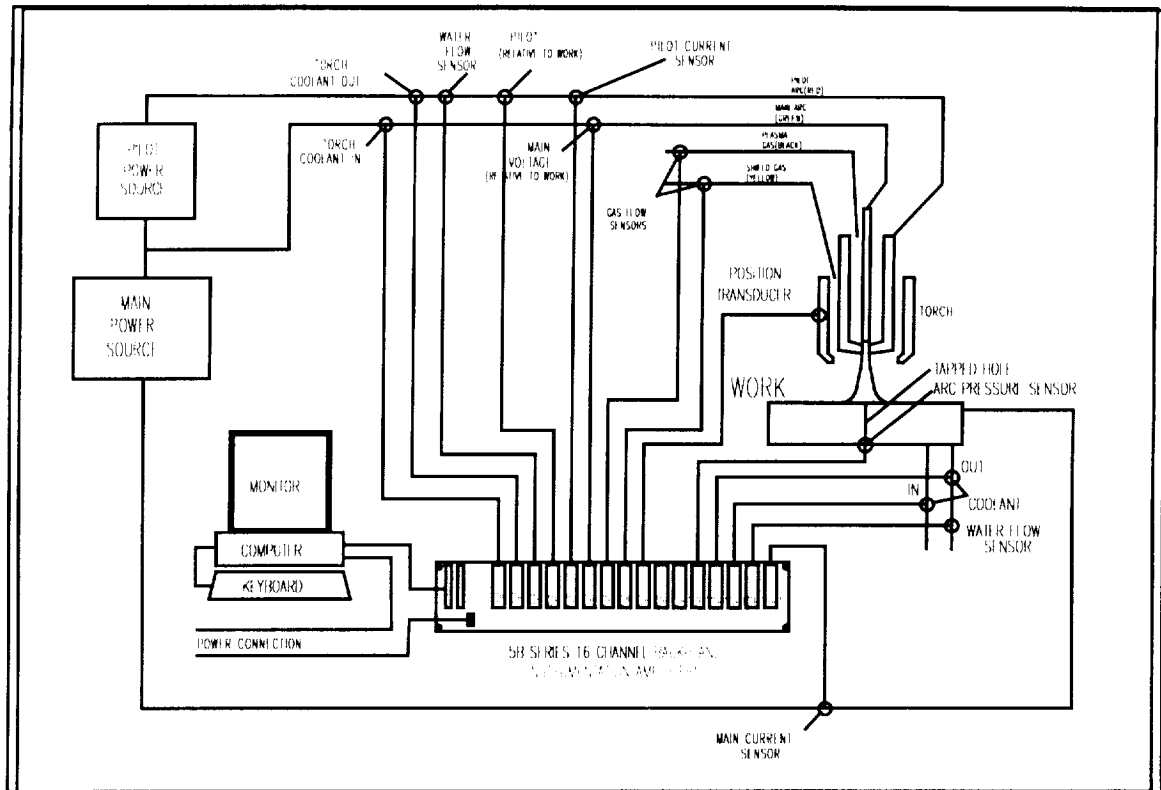


**Figure 15. Instrumentation System.**

The data acquisition system consisted of hardware, software, and sensing devices. The combination of these three components allowed for the data acquisition of welding parameters such as voltage, current, and gas flows. In addition, data for calorimetric and arc pressure measurements were acquired.

The acquisition system, shown in Figure 16, consisted of a desktop IBM-compatible personal computer with a data acquisition board. The computer was a 486/DX2 compatible with a VGA monitor, 8 Mbytes of RAM, 350 Mbytes of hard drive and a 3.5" floppy diskette drive. The data acquisition hardware, also shown in Figure 16, consisted of an Analog Devices type 5B01 Instrumentation Amplifiers backplane connected to a analog input computer card. The 5B01 board had 16 input/output channels powered by a 5 VDC power supply. Various signal conditioning isolation modules were utilized depending on the transducer signal levels. The modules used here were Analog Devices type 5B30, 5B31, and 5B34 modules with a 4 Hertz bandwidth.



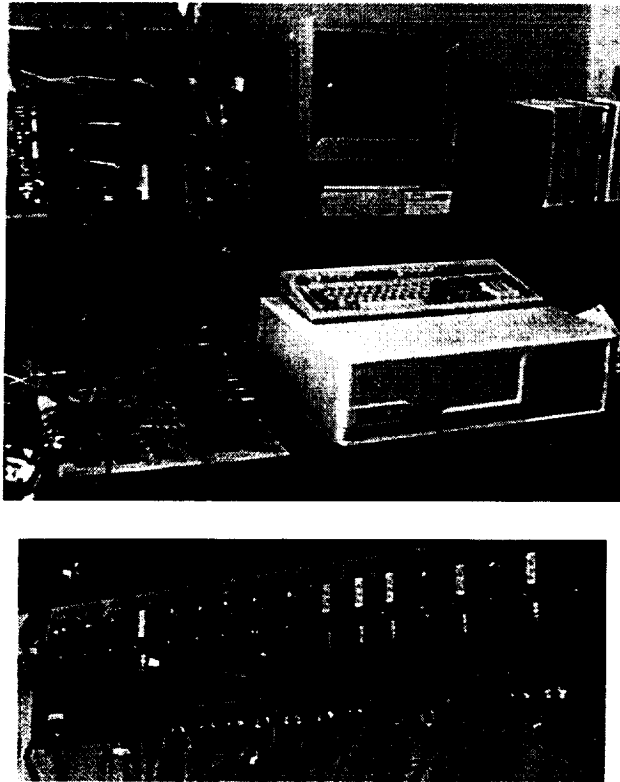


**Figure 16. Hardware.**

Labtech Control software was used for data acquisition. After the data was acquired, the data was saved in text format. All data was sampled at ten Hertz. The data was then imported into Microsoft Excel. Tables and graphics were created using Microsoft Excel for analysis of the experimental results.

Sensing devices were placed within or between connections of the above described VPPAW equipment in order to measure welding parameters such as voltages, currents, and plasma and shielding gas flows. Voltage signals related to the pilot arc and main arc were measured. Figure 17 shows the points of voltage measurement. The

voltage was passed through an EMI filter (low pass filter) for high frequency protection and through a voltage divider in order to reduce the voltage signal and meet the  $\pm 5$  V input of the conditioning module.

The main and pilot arc currents were measured by using two non-obtrusive Hall Effect current sensors. The two points of current measurement are shown in Figure 17. These devices were PI-600 current/watt sensors from F. W. Bell Corporation. They had a frequency range from DC to 1 kHz, adequate to measure at a 10 Hz sampling rate [Ref. 20]. The output signal of the current sensors was passed through a low pass R-C filter and through a voltage divider before reaching the signal conditioning module in the backplane. The R-C filter was used to eliminate high frequency noise from the signal. The voltage divider consisted of two resistors, one in series and the other in parallel, to reduce the voltage signal going into the conditioning module.

For measuring plasma and shielding gas flows, an Omega FMA-5609 mass flowmeter with a flow range of 0-5 liters per minute (LPM) and a Cole Parmer GMF-1710 with a flow range of 0-15 LPM were used respectively. Both flow meters, pictured in Figure 18, were powered by +12 VDC voltage sources and delivered output signals of 0-5 VDC.

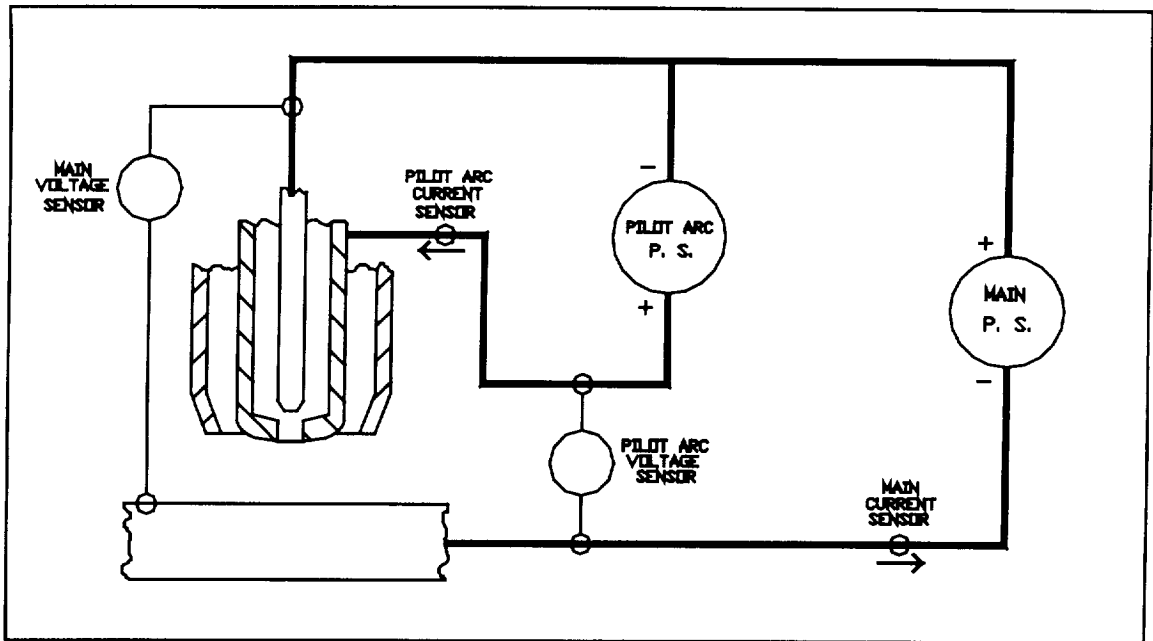


**Figure 17. Voltage and Current Measurement Points.**



**Figure 18. Gas Flow Meters.**

The water-cooled copper block, shown in Figure 19 and schematically in previous Figure 12, was designed specifically for the VPPA application with a centrally bored hole to provide for water flow and a small pressure tap as the pressure pick-up point for arc pressure measurements. This pressure tap was located off to one side of the water flow channel. An Omega PX150 series pressure transducer was used to measure the stagnation pressure onto the water cooled copper block. A 24 VDC constant potential power supply was utilized as the transducer's excitation source. The sensor's output used a 4-20 mA 2-wire loop with a parallel 250 ohms resistor to provide a 1-5 VDC signal to a signal conditioning module [Ref. 21].

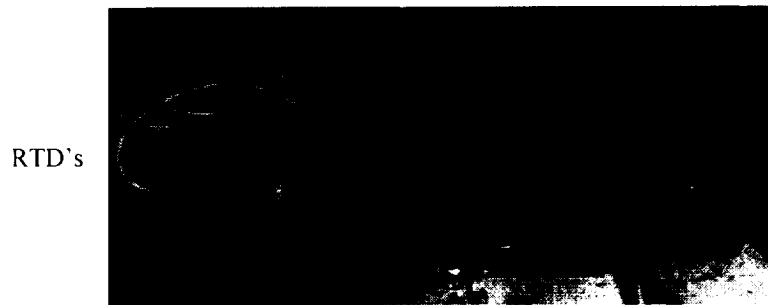


**Figure 19. Water Cooled Copper Block.**

An Omega PX142 gauge pressure transducer, with a sensitivity of 1.000 Volts per psi., was used to measure the back pressure of the plasma gas. This sensor was placed within the plasma gas hose between the welding torch and the plasma console. The PX140 series transducers are solid state piezoresistive devices with implanted resistors in a sensing diaphragm. When pressure was applied to its diaphragm, the resistance in the

chip changed, resulting in a voltage output proportional to the applied pressure. This sensor was excited with an 8 VDC power supply [Ref. 22].

The position sensor was a Genisco Tech PVT-150A position/velocity transducer pictured in Figure 20. This transducer was connected via a cable to the welding torch carriage running parallel to the direction of travel. As the welding torch moved forward, the cable reeled in and out of the unit to produce an output voltage signal proportional to the position of the welding torch.

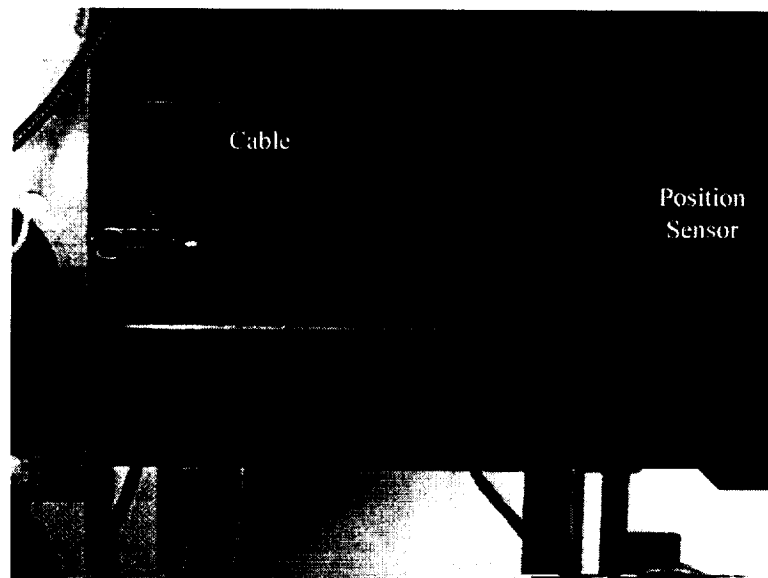


**Figure 20. Position Sensor.**

For calorimetric measurements, the two Omega FTB602 paddlewheel flowmeters shown in Figure 21, were connected to an FLSC-720 voltage range signal conditioner via a toggle switch. The toggle switch was allowed switching the signal conditioners between the two transducers. The flowmeters had a flow range of 0.3 to 9 LPM with a working pressure of 150 PSIG at 175°F. These flowmeters were installed in the welding torch and water cooled copper block coolant lines.

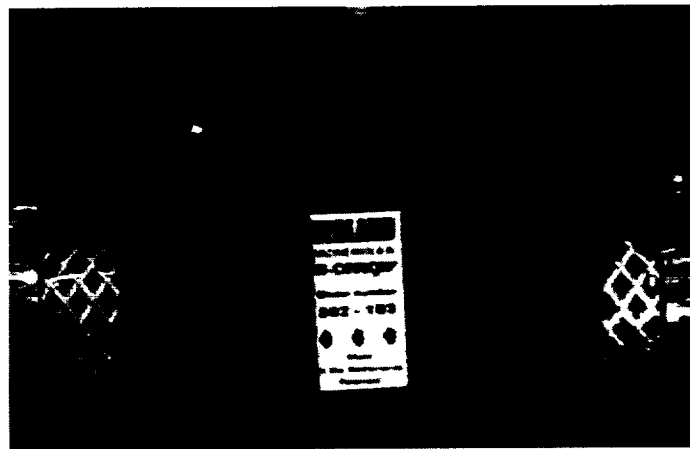


**Figure 21. Water Flow Meter.**

The sensors used for coolant temperature measurement were Platinum Resistance Thermometers (RTD) elements. These devices work on the principle that when a change in temperature of the RTD occurs, a change in electrical resistance within the resistive element of the RTD produces a voltage differential. The sensing unit or resistive element of the RTD was in the form of a wire wound of 99.99% pure Platinum hermetically sealed within a ceramic capsule to provide mechanical and electrical stability [**Ref. 23**].

The two kinds of RTD used were the 2PT100 K 2017 and the 1PT100 K 2010 made by Omega with a temperature range of -220 to +750 degrees Celsius. The RTD's were housed in brass tubes to protect the ceramic sensor and provide a suitable leak tight connection to the cooling system. A special machined copper fixture, shown in Figure 19, was prepared with connections for the inflow and outflow of the coolant. Via this fixture, the RTD's were inserted into the coolant system.

A three wire line connection was made to provide the excitation current and deliver the voltage signal to the data acquisition board where an Analog Devices 5B34 RTD input module was used. This module accepted an isolated 100  $\Omega$  platinum RTD input calibrated from 0 to 100 degrees Celsius with an output of 0 to 5 V to the computer.

### **3.2.3 Video System**

A video system, shown in Figure 22, consisted of three video cameras, a video cassette recorder (VCR), a video mixer, monitors, and a computer with a frame grabber board. A Pulnix TM-540 camera and a Pulnix TM-7 CCD camera were used to observe the arc and detect arc skew occurrences. One video camera was placed transverse to the welding direction in order to view the welding arc from the side relative to the direction of motion (Figure 22). The other camera was placed in the travel direction capturing the side-to-side view of the arc. Both camera were attached to the torch carriage so that the cameras moved with torch. Video signals from the CCD camera were mixed using a Panasonic WJ-MX10 video mixer resulting in a split screen of both video camera images.

Camera lenses were used to magnify the plasma arc images so that they would fill the split screen. The split screen image was recorded using a Panasonic NV-8200 VCR. The VCR was connected to a computer with a frame grabber board. Global Lab Image software was used to capture video images and save them into TIFF formatted files.

A Sony DXC-101 CCD camera, shown in Figure 23, was used to take high magnification images of the electrode and orifice surfaces for erosion investigation. Figure 24 shows the video setup for the high magnification images. Images were recorded using the Global Lab Image setup for analysis (see Figure 25).



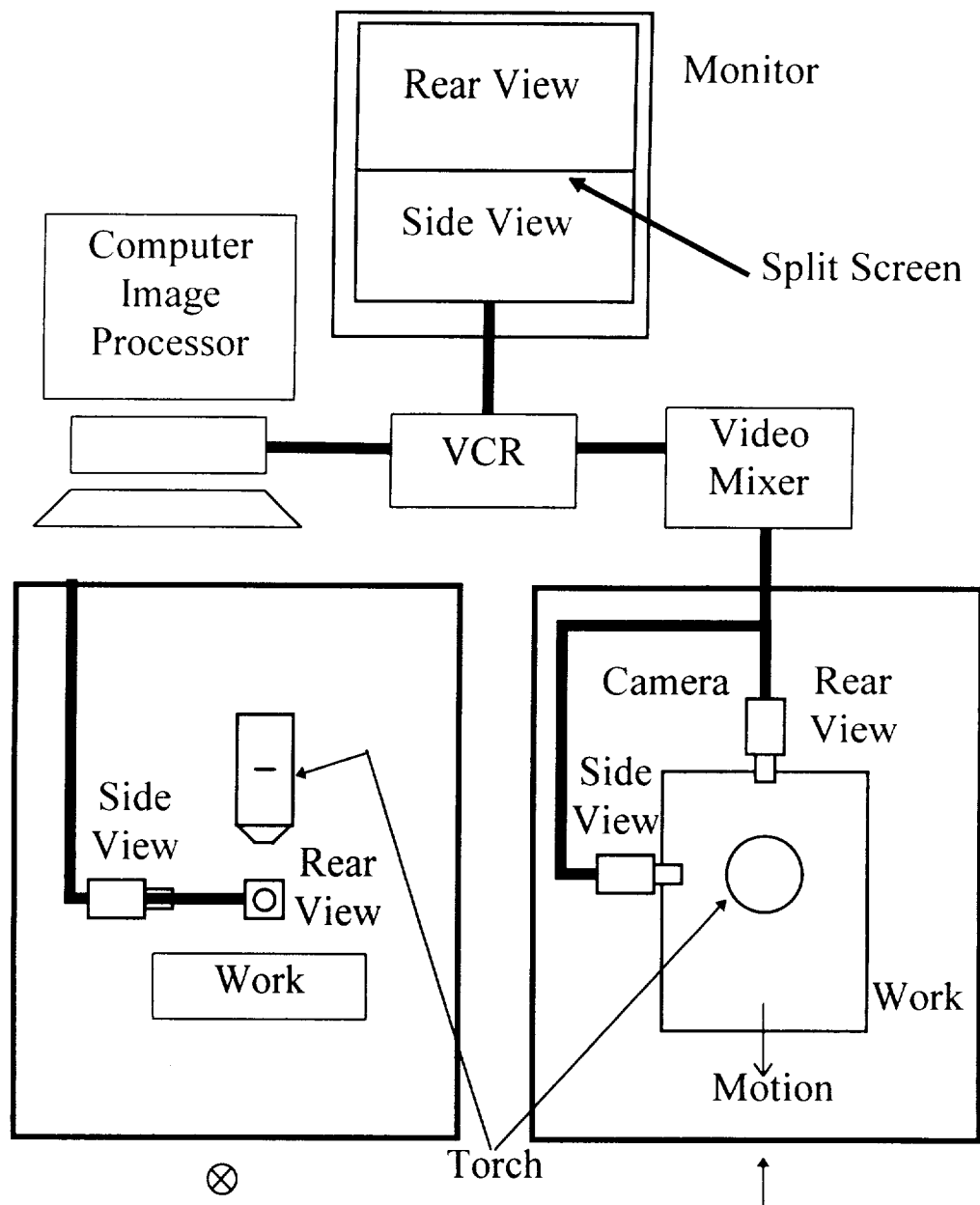


**Figure 22. Video Setup.**



**Figure 23. Sony DXC-101 CCD Video Camera.**



**Figure 24. Video Setup for High Magnification Images.**

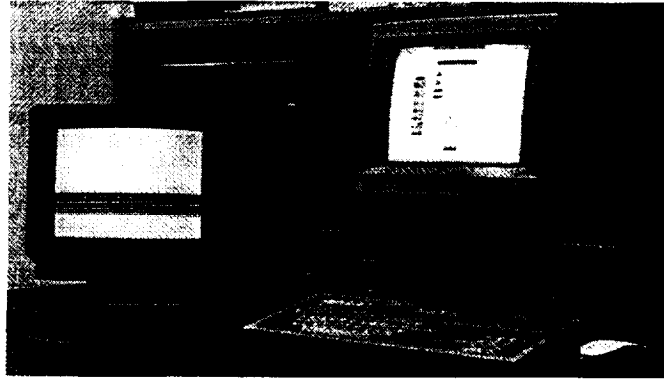


**Figure 25. Global Lab Image Computer Setup.**

### **3.3 Welding Conditions**

The electrodes used for the experiments were an  $\frac{1}{8}^{\text{th}}$  inch 2% thoriated tungsten with a 0.145 inch electrode setback distance. The setback is the distance from the orifice outer surface to the electrode tip once these are assembled. The tip preparation of the electrodes were either blunt or beveled. The bevel formed a 15 degree angle with the shank of the tungsten electrode, resulting in a 0.100 inch tip diameter. Most experiments were carried out with an  $\frac{1}{8}^{\text{th}}$  inch orifice unless otherwise specified. The shielding and plasma gases used were 99.998% argon with nominal gas flow rates of 25 cubic feet per hour (CFH) and 6 CFH respectively. Flow rates were varied accordingly to experimental requirements as described in following sections. A  $\frac{3}{8}^{\text{th}}$  inch standoff distance was used for most experiments except when variations in standoff distance were being tested. The welding current was varied according to experimental requirements. Specific welding conditions are presented with the results and discussions.

### **3.4 Experimental Procedures**

Several experiments were designed to study the VPPAW process and test possible sources of arc skew. The following section outlines the experiments performed in each of these areas.

#### **3.4.1 VPPAW experimentation**

The first phase of experimentation was designed to study the VPPA process by using high magnification video of the plasma arc and by measuring welding parameters such as voltage, current, arc pressure, gas pressures, gas flows, coolant temperatures, coolant flows, position, and others. Calorimetric and arc pressure measurements also were performed to provide additional information about the VPPA process. Video observations provided documentation for evaluating the arc when the measured welding parameters were varied.

#### ***Arc Pressure Measurements***

The arc pressure measurements were performed by establishing the welding arc and running the torch above a pressure tap located on a water cooled copper block. Sensing devices were used to measure arc pressure and position. The weld pass began before the pressure tap and ended after it, at a welding speed of one inch/min. An insert

to the inner orifice, shown in Figure 26, was designed to allow alignment of the welding torch axis on the pressure tap axis. Then, a variable resistor, located within the positioning sensor output signal, was adjusted until the voltage across the conditioning module input terminals was balanced to zero. At the beginning of each run, the data acquisition system was activated to store arc pressure data. Once the data was acquired, the data was downloaded into Microsoft Excel for analysis.



**Figure 26. Inner Orifice Insert.**

### ***Calorimetric Measurements***

The same water cooled copper block used for arc pressure measurements was utilized for calorimetric measurements. Special fittings were prepared to place temperature sensors in the inlet and outlet coolant flow of the welding torch and the chilled copper block. Flowmeters were placed in the outlet hoses of both coolant systems. The welding arc was operated over the coolant channel of the copper block while data acquisition took place.

During calorimetry runs with EN operation, the welding torch was stationary over the copper block. However, when running VP, the welding torch was moved back and forth over the copper block. This was done because during VP, the plasma arc became unstable once the region around the plasma arc had been cleaned of oxide. The reverse polarity of the VP cycle required uncleaned cathodic sites to maintain its operation.

A heat balance was used to determine heat loads from coolant temperatures and flows for the calorimetric study. The heat balance can be represented by the following equation:

$$P = W + T + L \quad (1)$$

where  $P$  is the electrical power,  $W$  is the work heat load,  $T$  is the torch heat load, and  $L$  is heat that is unaccounted for and considered to be lost, e.g., by radiation from the arc. The measurable parameters were  $P$ ,  $W$ , and  $T$ .  $P$  was measured from main arc voltage and current.  $W$  and  $T$  were measured by calorimetry. The lost heat was then found from:

$$L = P - (W + T). \quad (2)$$

The electrical power was calculated by:

$$P = V \times I \quad (3)$$

where  $V$  is the main voltage and  $I$  is the main current. The torch and work heat loads were calculated from the equations:

$$W = (T_{out} - T_m) \times W_{pw} \times C \times \rho \times 4.18 \times 10^6 \quad (4)$$

$$T = (T_{out} - T_m) \times W_{pt} \times C \times \rho \times 4.18 \times 10^6 \quad (5)$$

where  $T_{out}$  is the measured outlet temperature, and  $T_{in}$  is the measured inlet temperature, of the coolant fluid in degrees Celsius.  $W_{fw}$  and  $W_{ft}$  are the coolant flows through the workpiece and torch, respectively, in Liter/sec,  $C$  is the specific heat of water in cal/g°C,  $\rho$  is the density of water g/liter, and  $4.18 \times 10^6$  is a conversion factor from calories/sec to Joules/sec or Watts.

Changes in current, orifice diameter, electrode preparation, plasma and shielding gas flows, plasma gas pressure, and standoff distances were introduced to determine the process response to these variations.

### **3.4.2 Testing the Possible Causes of Arc Skew**

The second phase of the study was to look at possible causes of arc skew by means of video observations of arc skew. As part of the arc skew experimentation, electron flows and the deterioration of surfaces involved in the current path of the plasma arc were studied.

Some basic arc runs were completed using electrode negative (EN) and variable polarity (VP), with and without the pilot arc in operation. Electrode positive was not performed because of arc instability when running the electrode positive portion of the VP cycle alone. Video frames were obtained to show arc behavior under various operating conditions. Video observations during arc pressure and calorimetric measurements were performed to record any variation of the plasma arc performance.

In order to study the basic effect of asymmetry on arc skew, various asymmetries were intentionally introduced within the torch assembly. For example, an electrode was prepared asymmetrically by deliberately grinding away a portion of the electrode to produce a bevel to the electrode tip. Similarly, an orifice was prepared with a slight offset from the torch centerline. Video observations of the arc operating with these asymmetries were recorded, noting the arc skew relative to the direction and location of the electrode and orifice asymmetries. Blockage to the shielding gas flow was imposed so that an asymmetry was introduced to the gas flow. Finally, asymmetry in the electrode and orifice due to erosion were observed by inspection before and after welding with a high magnification video system.

Oscilloscope traces of voltage and current were recorded at different points in the welding circuit to allow analysis of the path of the main and pilot arc currents. A Tektronix 2211 digital storage oscilloscope was used for observation of time resolved current and voltage waveforms. Voltage measurements were realized by using voltage probes while Fluke's Y8100 DC/AC and 80i-1010 DC/AC current probes were used for current measurement. The oscilloscope signals were stored and then printed.



## **4. RESULTS & DISCUSSION**

This chapter presents the results and discussion of each stage of experimentation. The first stage focuses on the study of the VPPAW process in general. Next, an analysis of the possible causes of arc skew is presented. Finally, the chapter concludes with a summary of the findings regarding the causes of the arc skew phenomena.

### **4.1 Study of the VPPA Process**

A mathematical model capable of simulating torch behavior was developed in parallel with the experimental effort. In order to model the process, gas pressure, torch dimensions, and operating conditions were provided. The model was able to provide the arc pressure distribution on the flat work piece for given operating conditions. The results of the simulation were verified by comparison to the empirical results of arc pressure performed in the laboratory. The first phase of experimentation to be reported focused on the measurement of arc pressures. The arc pressure data also provided information about the location and distribution of the main plasma arc on the work piece. The data also displayed asymmetries associated with a skewed arc.

In addition, calorimetry supplemented the study of the VPPA process and later contributed to an evaluation of the possible solutions to arc skew. Heat loads, as they relate to welding parameters, were measured by means of calorimetry. Calorimetric measurements of work and torch heat loads were to identify the effect of change in operating conditions on the heating efficiency of the process.

#### **4.1.1 Arc Pressure Measurements**

The plasma arc pressure plays a role in the production of the keyhole in the weld material during the PAW process. As the arc pressure increases, a deeper keyhole depression can be formed in the weld pool, providing the possibility of welding thicker aluminum sections. The pressure exerted by the plasma arc as a function of current, plasma gas pressure and electrode tip configuration was studied.

Plasma arc pressure profiles were obtained by moving the welding arc across a pressure tap on the chilled copper block. Initial trials were performed in order to test the equipment and ensure that the pressure profiles were not distorted by lags in the pressure measurement readings or by torch to pressure tap misalignment. It was found that a one inch per minute (ipm) welding speed was sufficiently slow to avoid any lags.

Figure 27 shows a typical pressure profile for cold flow (no arc). Cold flow measurements were performed with plasma gas only because the welding equipment did

not allow for the shielding gas flow to operate unless arc initiation had occurred. Figure 28 shows a typical arc pressure profile for an 88 Ampere, DCEN arc without the operation of the pilot arc. Other operating conditions for these runs are shown in the figures. It can be seen that the maximum pressure increased from .97 with cold flow to 13.4 inches of water with the arc. The full width at half maximum decreased slightly from 0.15 inch for the cold flow profile to 0.14 inch for the 80 Ampere profile, but otherwise a similar distribution was observed for both the cold and arc pressure profiles.

The zero value of the position axis for the pressure profiles, shown in Figure 27 and Figure 28, indicate the location where the orifice was mechanically aligned with the pressure tap as described earlier. The slight offset of the peak pressures may be measurement error, or natural skew of the jet or arc. Recall for reference that the pressure tap was 0.020 inch in diameter. Also note the slight asymmetry in the plasma arc pressure profile. Data extracted from these pressure profiles, particularly maximum pressure and width of the pressure distribution at one-half maximum (Full Width at Half Maximum - FWHM), provided results for further analysis.

Plasma gas supply or back pressure was measured for comparison with predictions from the mathematical model. The plasma gas supply pressure was important in the study because it provided a measure of the amount of the constriction in the flow created by the plasma arc, which was simulated by the model.

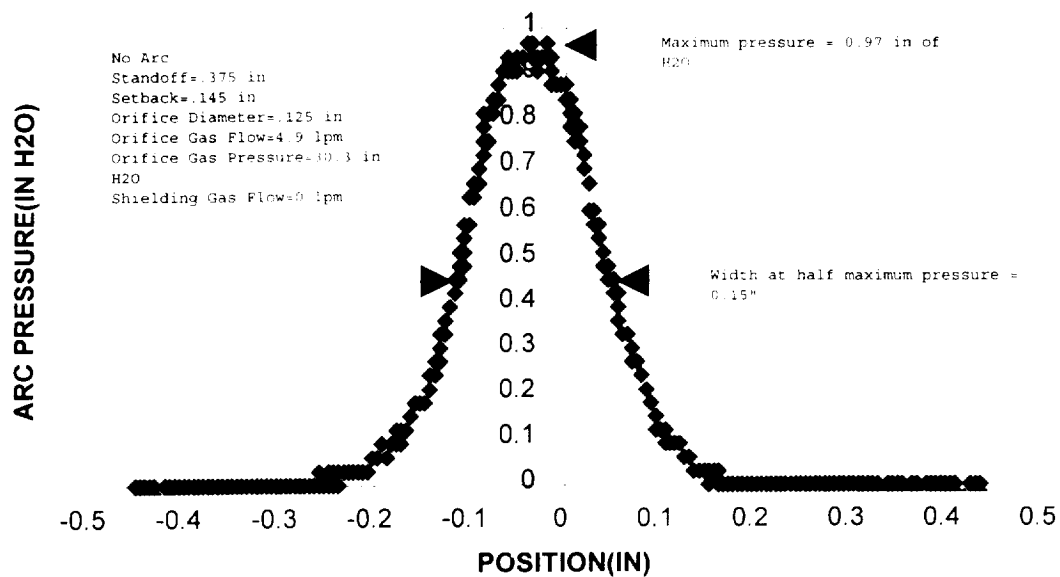


Figure 27. Typical Cold Flow Pressure Profile (arc off).

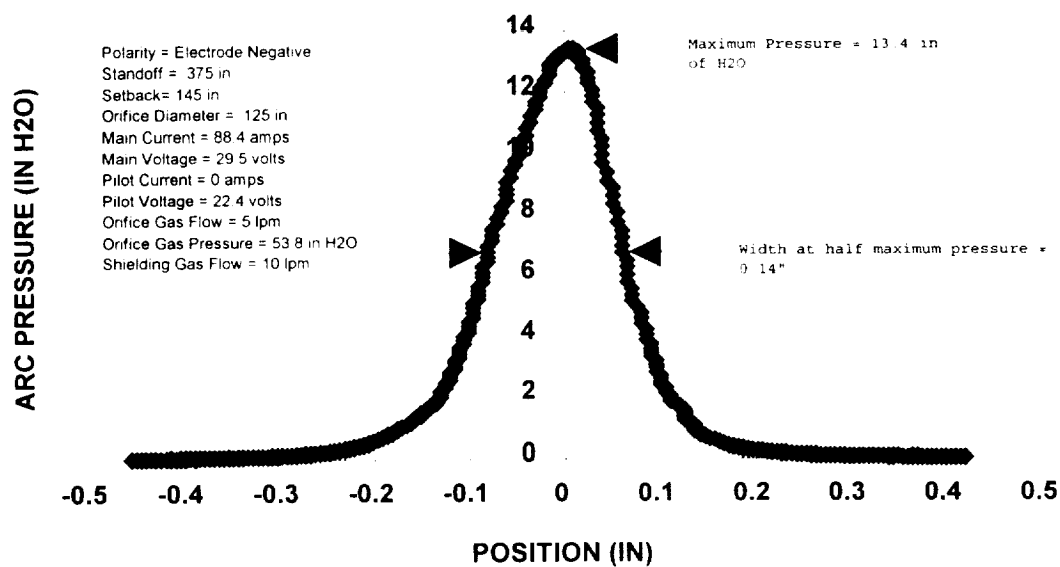
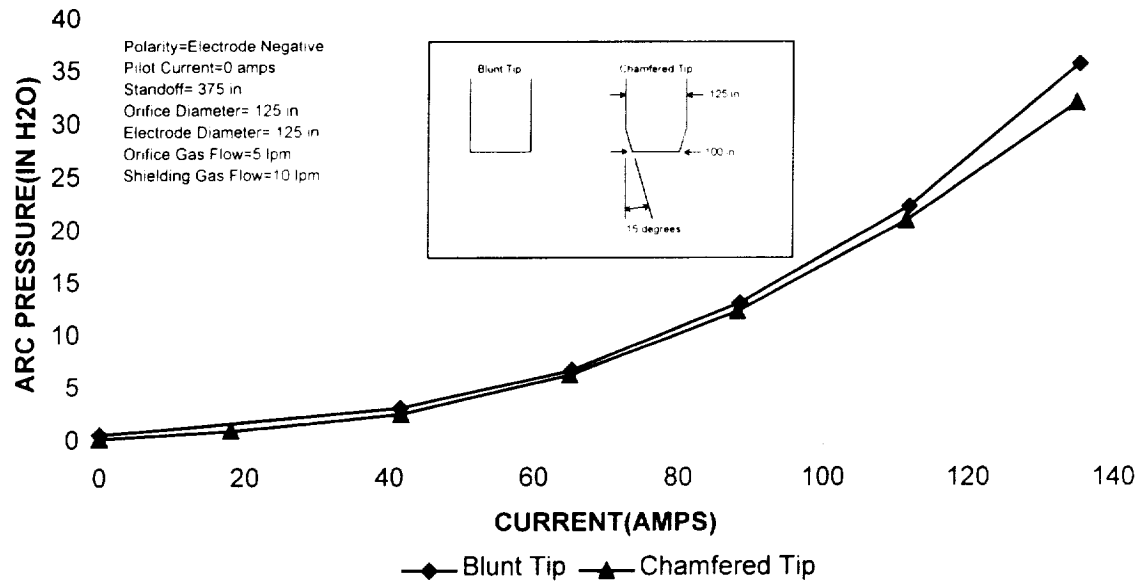


Figure 28. Typical Arc Pressure Profile (arc on).

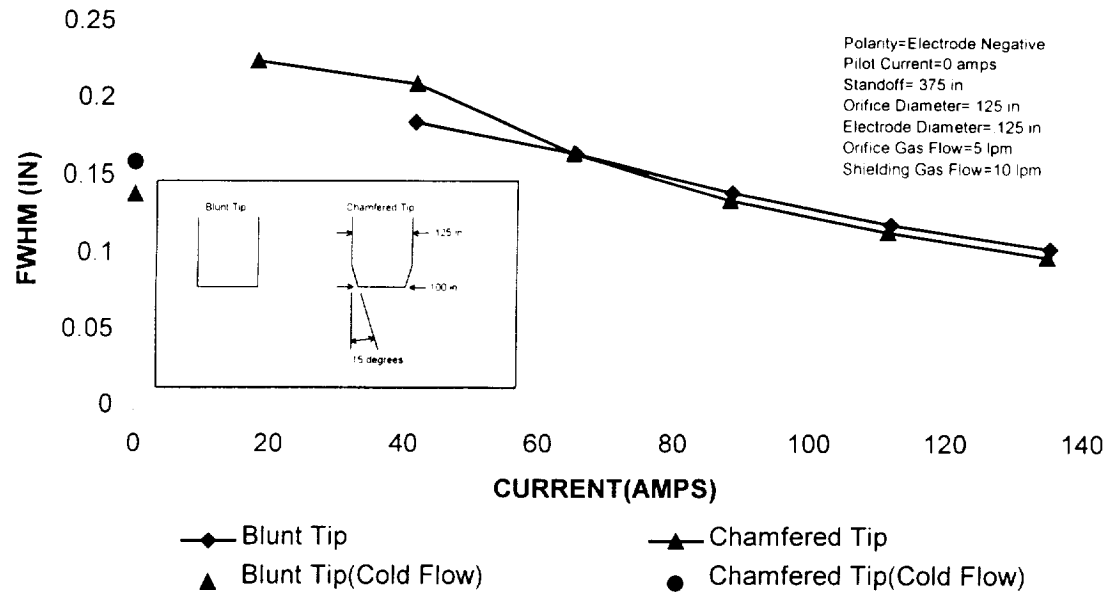
In the following section, the effects of current on the measured pressures are presented. Figure 29 presents the maximum pressure of the arc pressure profile as a function of current. The currents tested range from zero to 140 Amperes. As shown in the diagram within Figure 29, two electrode tip configurations, a blunt and a chamfered tip, were tested with the same electrode setback to study the effects of electrode preparation on arc pressure.

Figure 29 shows that as the welding current increases, the arc pressure increases in a quadratic like behavior. In addition, the chamfer in the electrode tip resulted in a slight decrease in arc pressure for a given arc current. In general, the pressure force created by the plasma on the weld metal plays a role in the penetrating potential of the welding process. Therefore, based on the results from Figure 29, the current capacity of the welding torch determines the achievable arc pressures by the square of the current.



**Figure 29. Arc Pressure as a Function of Main Current for Blunt and Chamfered Tip Configurations.**

Figure 30 presents the FWHM of the pressure distribution as a function of current. As the welding current increased, the FWHM decreased. This indicates that arc constricts with increasing arc current. This contributes to the effect of creating a larger depression of the pool since the higher arc pressure is applied over a smaller area of the weld pool.. Both the chamfered and blunt electrode tip yielded similar results.



**Figure 30. Half Pressure Diameter as a Function of Main Current.**

Figure 31 shows the plasma gas supply pressure (back pressure) as a function of current. It was found that as the welding current was increased, the back pressure increased. This can be explained by continuity of flow. As the plasma gas enters into the hot arc region, the gas expands, increasing the supply pressure. The gas flow velocity increases in order to maintain conservation of mass flow through the orifice. As the welding current is increased, the heating increases, and the gas pressure must increase to produce faster gas flow velocities at the orifice. The higher these velocities become, the more arc pressure will be applied to the work surface.

Similar back pressure trends were found for both electrode tip configurations, but as previous results show, lower back pressure was observed with the chamfered electrode tip due to less flow constriction.

In summary, an increase in the main current will result in an increase in arc pressure and plasma gas pressure (back pressure) with a decrease in the width of the arc. The model would be expected to exhibit these same characteristics.

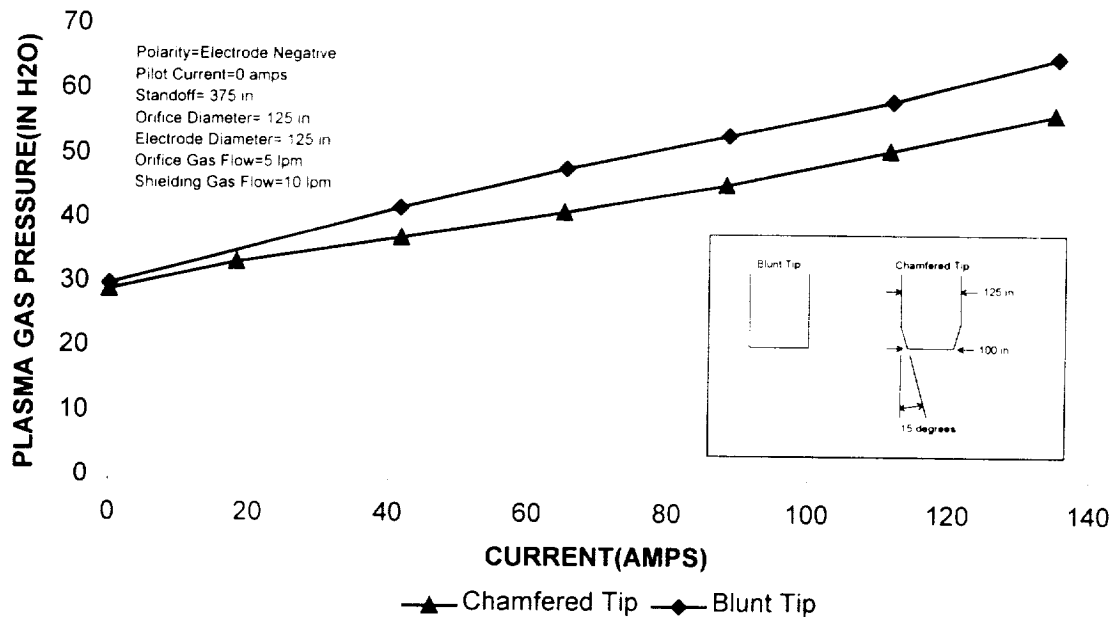


**Figure 31. Plasma Gas Pressure as a Function of Main Current.**

#### 4.1.2 Calorimetric Investigations

Calorimetric measurements are performed on arc welding processes to study the deposition of heat as a function of welding conditions. Arc efficiencies are also revealed by such experiments. Calorimetry was performed in this work to examine work and torch heat loads under various operating conditions. The heat load on the torch is important to



design of the plasma torch due to the heat affects on deterioration of the electrode and orifice. This deterioration is believed to be an important contributor to arc skew.

Calorimetry measurements were made with varying current, plasma and shielding gas flow, torch standoff distances, and orifice diameter. The heat loads associated with the work and the torch are presented in the following charts.

The welding parameters used during the calorimetric measurements are summarized in Table 1. Note that the varied parameter for the given welding condition is highlighted in gray. All conditions were with DCEN.

<u>File Name</u>	<u>Main Voltage</u>	<u>Main Current</u>	<u>Plasma Flow</u>	<u>Shielding Flow</u>	<u>Orifice Diameter</u>	<u>Standoff Distance</u>
Cal-01	29	88	5	10	0.125	0.375
Cal-03	31	139	5	10	0.125	0.375
Cal-06	33	190	5	10	0.125	0.375
<u>File Name</u>	<u>Main Voltage</u>	<u>Main Current</u>	<u>Plasma Flow</u>	<u>Shielding Flow</u>	<u>Orifice Diameter</u>	<u>Standoff Distance</u>
Cal-g4	28	141	2	10	0.125	0.375
Cal-g3	30	141	3	10	0.125	0.375
Cal-g2	32	140	4	10	0.125	0.375
Cal-g1	33	141	5	10	0.125	0.375
<u>File Name</u>	<u>Main Voltage</u>	<u>Main Current</u>	<u>Plasma Flow</u>	<u>Shielding Flow</u>	<u>Orifice Diameter</u>	<u>Standoff Distance</u>
Cal-g7	34	140	5	6	0.125	0.375
Cal-g6	34	140	5	8	0.125	0.375
Cal-g1	33	141	5	10	0.125	0.375
Cal-g5	34	140	5	12	0.125	0.375
<u>File Name</u>	<u>Main Voltage</u>	<u>Main Current</u>	<u>Plasma Flow</u>	<u>Shielding Flow</u>	<u>Orifice Diameter</u>	<u>Standoff Distance</u>
Cal-or1	26	141	5	10	0.094	0.375
Cal-or3	31	140	5	10	0.125	0.375
Cal-or2	41	140	5	10	0.156	0.375
<u>File Name</u>	<u>Main Voltage</u>	<u>Main Current</u>	<u>Plasma Flow</u>	<u>Shielding Flow</u>	<u>Orifice Diameter</u>	<u>Standoff Distance</u>
Cal-d3	29	141	5	10	0.125	0.250
Cal-d2	32	140	5	10	0.125	0.375
Cal-d1	33	141	5	10	0.125	0.500

**Table 1. Welding Conditions Used for Calorimetric Measurements.**

The first set of calorimetric measurements studied the effect of variations in welding current. Figure 32 shows the heat load distribution for three current levels in units of watts. The electrical power was determined by multiplying plasma arc current and voltages, as measured during plasma arc operation. As discussed earlier, the power loss is the difference between the electrical power and the measured heating rates. It can be seen that an increase in electrical power from 2771 to 6495 Watts was produced by the increase in welding current from 88 to 190 Amperes. The calorimetrically measured work and torch heat loads also increased with increasing welding current. The voltage increased as can be seen from Table 1.

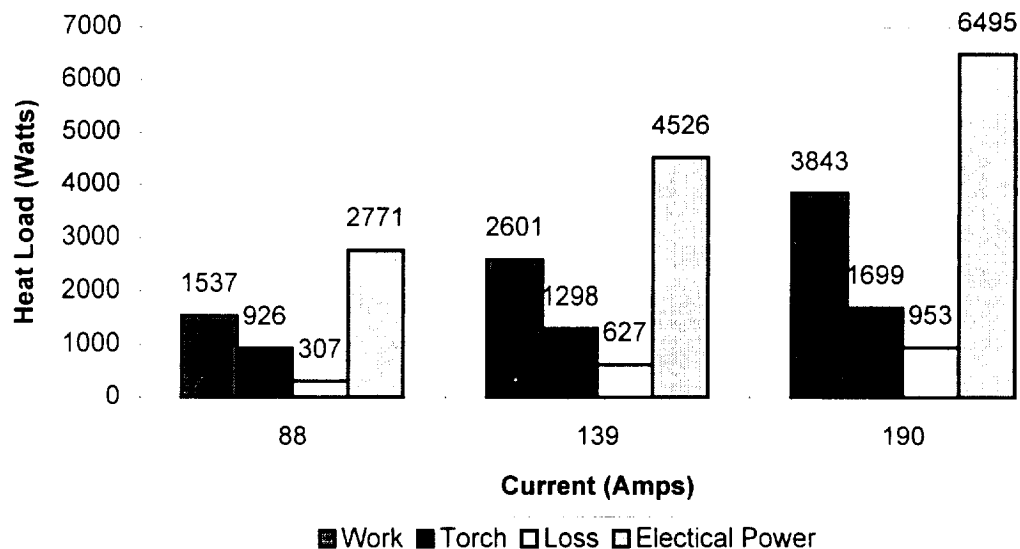


**Figure 32. Current Variation Effects on Heat Loads.**

Figure 33 presents the data in Figure 32 in the form of percentages of the total electrical power. It can be seen that the increase in welding current from 88 to 190 amperes reduces the percentage welding torch heat load by 8%, of which 4% is accounted for by an increase in the lost heat. The percent of work heat load accounts for the rest, increasing from 55 to 59 %. This percentage figure is also the arc efficiency. Thus, at higher currents, the arc efficiency increases slightly. At the 88 ampere level, the welding torch receives the highest percentage of heating among the three current levels tested.

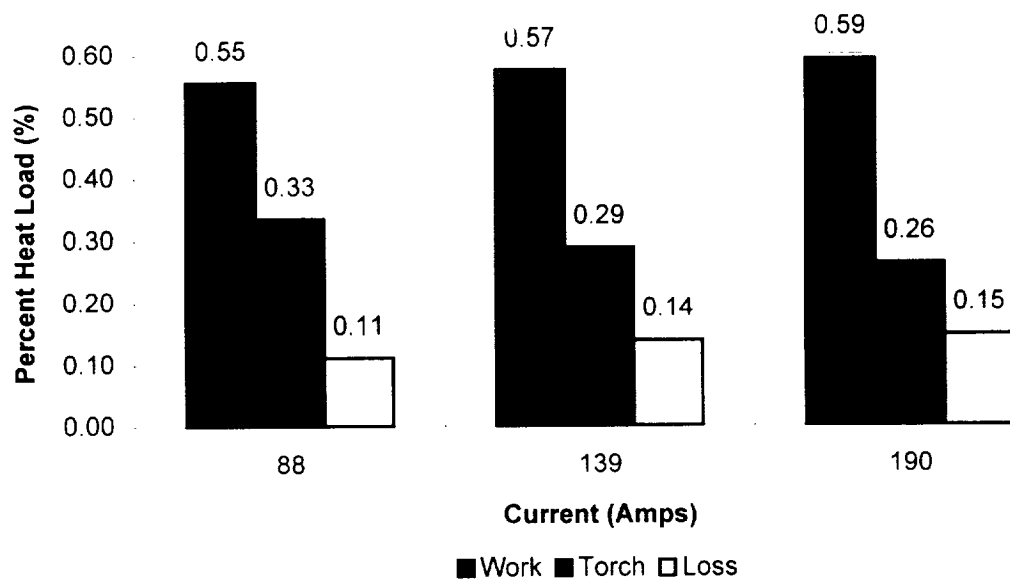


**Figure 33. Current Variation Effects on Percent of Heat Loads.**

A second set of calorimetric experiments examined plasma and shielding gas flows at a current level of approximately 140 amps. Plasma gas flow was varied from 2 LPM to 5 LPM, with results shown in Figure 34. The total electrical power dissipation increased from 3959 to 4694 watts, or 735 watts. The work heat load increased from 2151 to 2794, or 643 watts. This is comparable to the electrical power increase. It is interesting that the torch component of heat load decreased from 1585 to 841, or 744 watts, while the lost heat increased from 223 to 1058, or 835 watts. Thus, plasma gas flow rate is an important parameter relative to work and torch heating rates, with higher flow rates significantly increasing work and decreasing torch heat loads.

Shielding gas flow variations, shown in Figure 35, showed no significant effects on the heat load distribution between the torch, work and lost heat loads. This is not surprising, since the shielding gas is not heated directly by the plasma arc, and plays no obvious role in the arc heat balance.

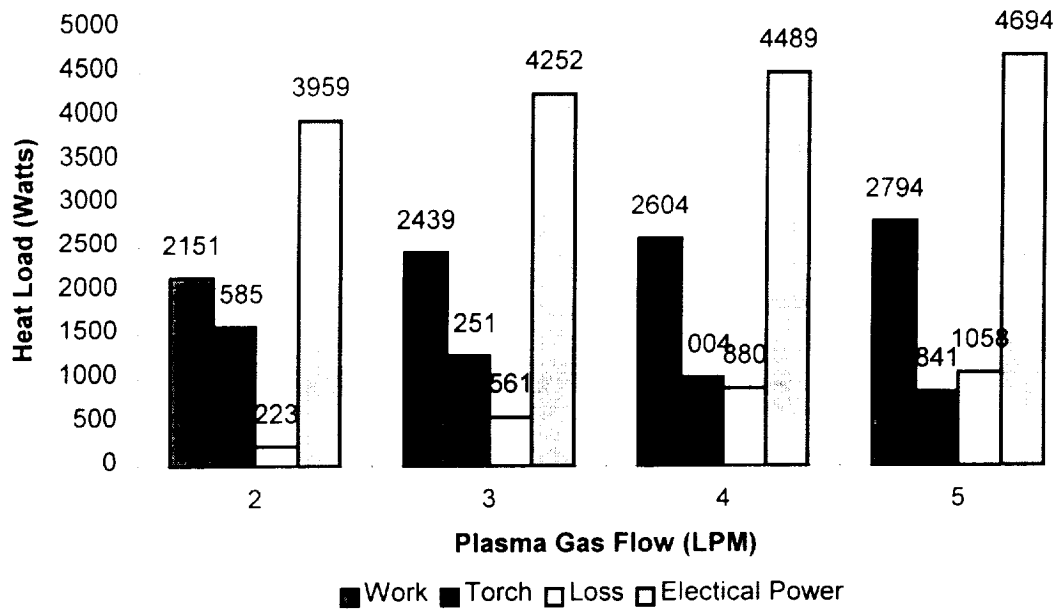


Figure 34. Plasma Gas Flow Variation Effects on Heat Loads.

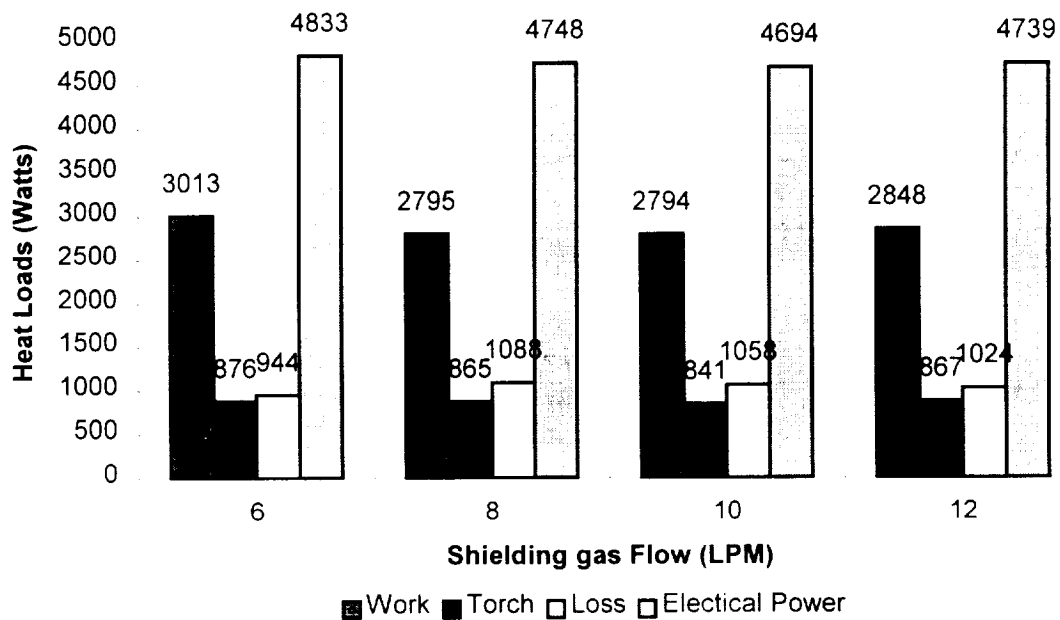


Figure 35. Shielding Gas Flow Variation Effects on Heat Loads.

A third set of experiments dealt with variations in orifice diameter, shown in Figure 36. Other operating conditions are shown in Table 1. In this case, the total electrical power delivered by the welding power supply decreased from 5668 to 3698 Watts with increasing orifice diameter. This is reflected in the voltage drop from 41 to 26 Volts. As the orifice diameter was increased, the welding arc demanded less voltage for the same current level. It can be seen that the increase in electrical power with decreasing orifice diameter is most significantly manifested in an increase in work heat deposition. The increase in torch heat load is relatively small.

Variations in standoff distance were investigated and results are shown in Figure 37. The electrical power increased from 4066 to 4643 Watts for an increase in standoff distance from 0.25 to 0.5 inch. The increase in power dissipation is, in this case, due to an increase in voltage that results from the longer plasma arc length. It is interesting that most of the power dissipation increase shows up in work piece heating rather than in lost heat, as would be expected for a conventional welding arc. This is apparently due to the strong effect of convection of heat to the work via the plasma flow. The torch experiences little increase in heat load due to the increased stand-off distance.

In Figure 36, the lowest torch heat load was found for the 0.125 inch orifice diameter, while Figure 37 shows that the lowest torch heat load occurred at the shortest standoff distance of 0.25 inch. These results are useful relative to design and application considerations directed at the minimizing heat induced deterioration of the torch components. The study of the torch performance by means of calorimetric and arc

pressure measurements have provided documented information that could be used as a baseline for further research and possible guidelines for future torch modifications.

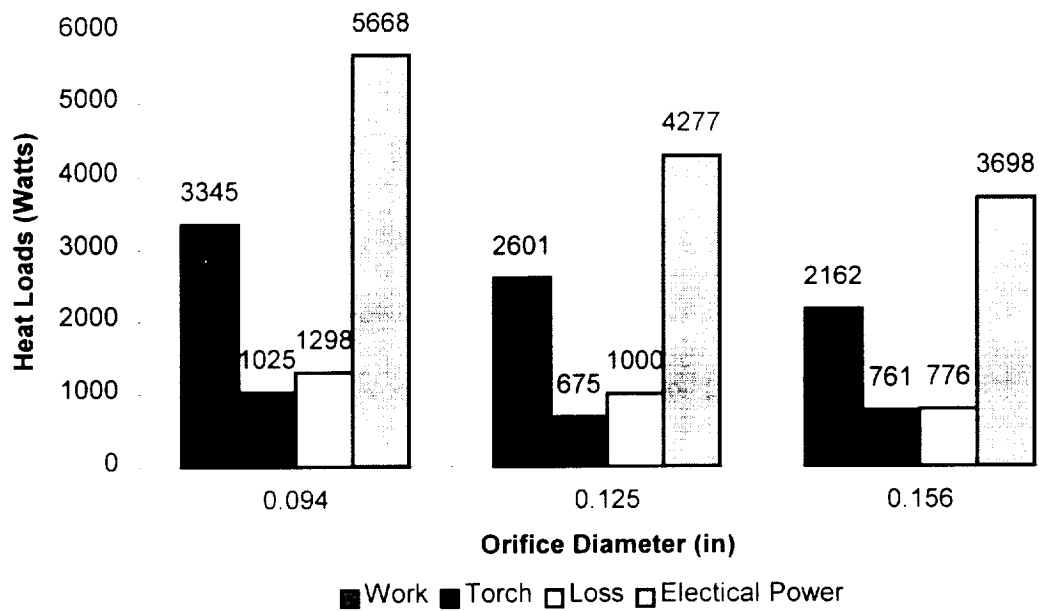


**Figure 36. Orifice Diameter Variation Effects on Heat Loads.**



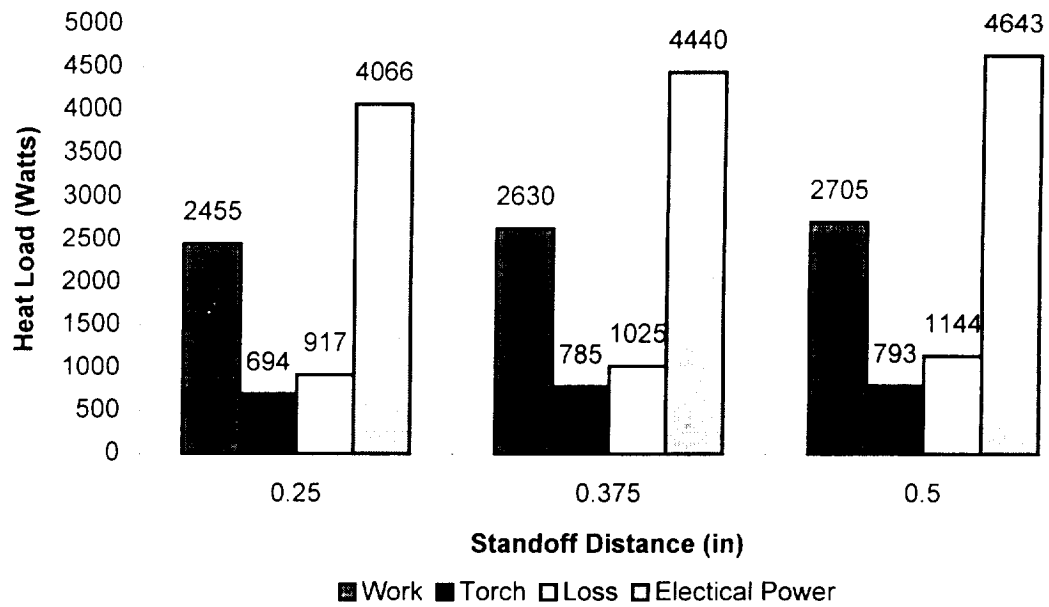


**Figure 37. Standoff Distance Variation Effects on Heat Loads.**

## 4.2 Arc Skew Observations

A series of experiments were designed to study the occurrence of arc skew. The arc skew experiments were developed and refined throughout the course of the investigation. The use of video observations played an important role throughout this investigation. Video was the main method utilized to detect arc blow or arc skew occurrences.

### *Asymmetric Electrode*

Asymmetric erosion within the torch assembly has been thought to be a possible cause for arc skew. In order to test this, an asymmetric electrode tip was deliberately prepared with the idea of simulating uneven erosion of the electrode and to determine its affects on arc skew. The first approach was to perform arc pressure measurements and compare them to those for normal arcs.

Figure 38 shows the cold flow pressure profile, while Figure 39 shows a 90 Ampere arc pressure profile, both with the asymmetric electrode. The arc pressure measurements for an asymmetric electrode presented uneven pressure distributions for both a cold flow and a 90 Ampere arc pressure profiles. In the right corner of both figures, the details of the electrode preparation are presented. The cold flow pressure profile distribution was non-uniform when compared to a previously shown cold flow measurement in Figure 27. In addition to non-uniformity, the asymmetric electrode cold flow shows a decrease in the peak arc pressure value by almost half. This decrease in the peak pressure can be explained by the increase of the exit area available for the plasma gas to flow out of the torch. The non-uniformity in the pressure profile is indicative of arc skew.

In the case of the 90 ampere arc pressure profile, this showed a double peak that could be associated with non-uniform plasma gas flow. This double peak was not present in the previous arc pressure measurement of Figure 28, thus being associated with the asymmetry introduced to the electrode. It can be seen that the arc skew occurred toward

the constricted side of the asymmetry, that is, to the left side in both Figure 38 and Figure 39. This was consistent with the visible arc skew.

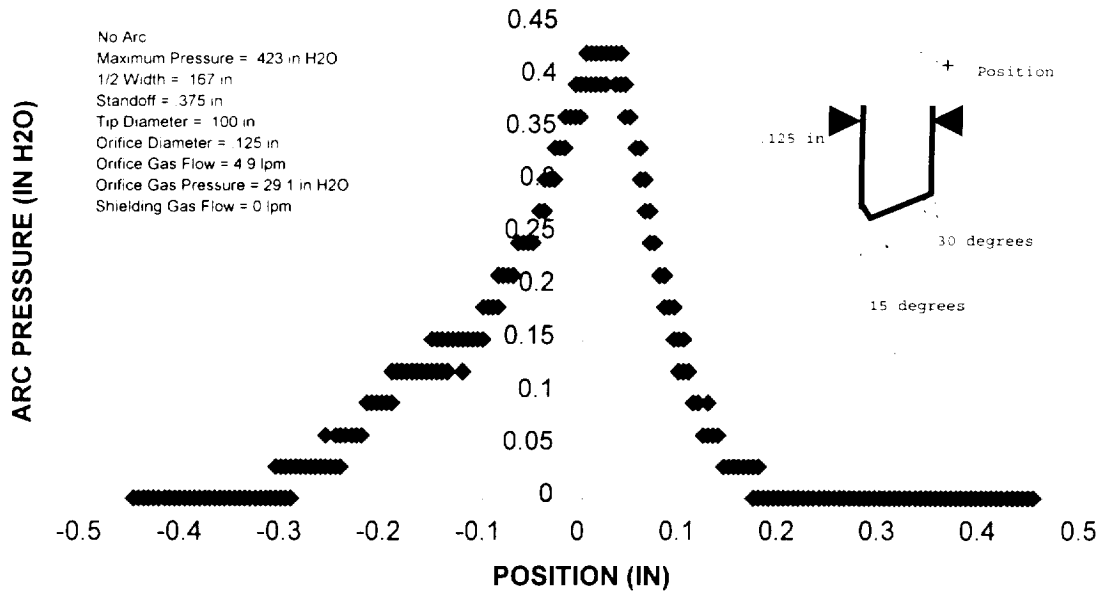


**Figure 38. Cold Flow Pressure Profile for an Asymmetric Electrode Preparation.**

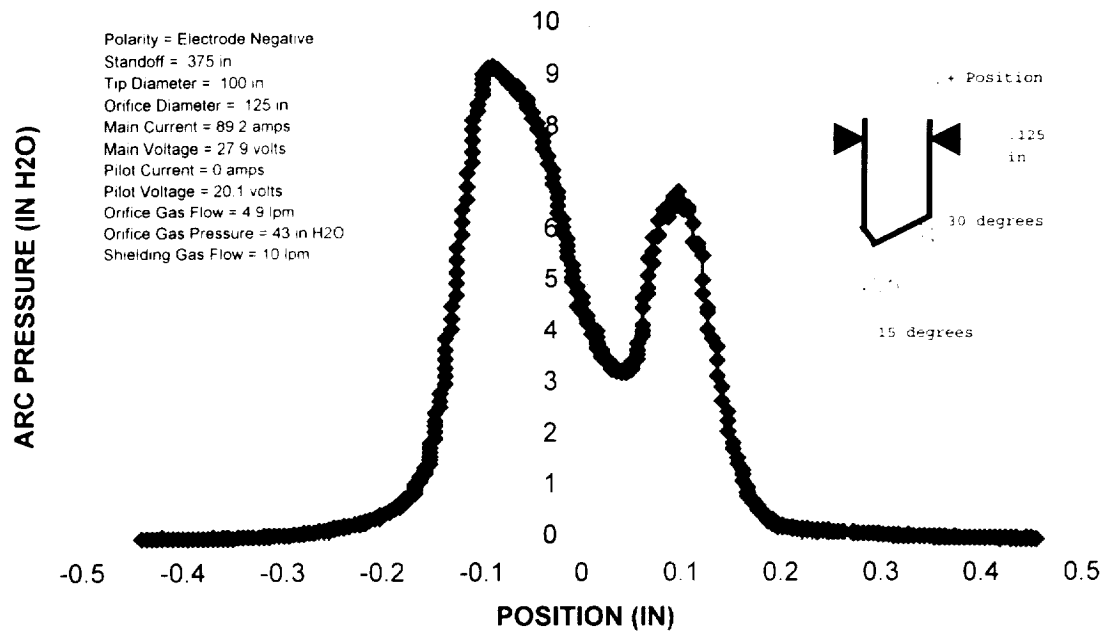


**Figure 39. Arc Pressure Profile for an Asymmetric Electrode Preparation.**

The second method used to examine the effects of erosion on the electrode was based on video observations of the plasma arc. An asymmetry to the electrode was deliberately introduced by knocking a corner of the electrode off with a grinder. Figure 40 shows a schematic representation of the asymmetric condition that was introduced. Figure 41 shows a split video frame of the arc skew that was produced by introducing this asymmetry to the electrode tip. Arc skew was observed to occur towards the front of the torch, as seen in the view of Figure 41. In the rear view of the plasma arc, arc skew was not detected. Therefore, the electrode asymmetry produced an arc skew occurring toward the constricted side, or the greater flow blockage, as depicted in Figure 40. This observation is consistent with the arc pressure measurements although the positioning of the asymmetry is inverted by 180 degrees between the two experiments.

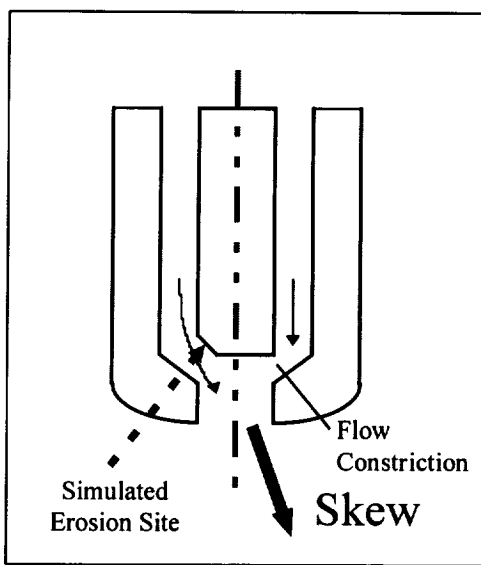


**Figure 40. Electrode Offset by Introducing a Bevel.**

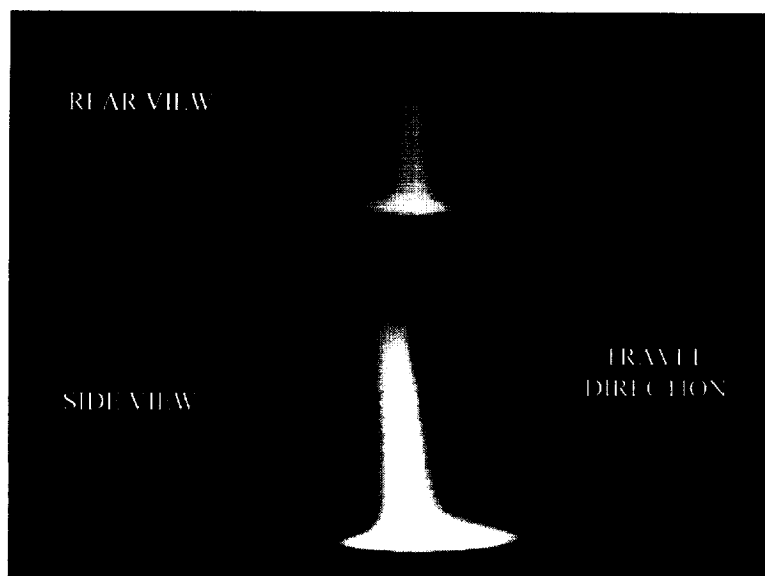


**Figure 41. Video Frame Showing Arc Skew.**



### ***Asymmetric Orifice***

An asymmetric orifice was prepared in order to simulate the erosion effects on the orifice and determine its effects on arc skew. Figure 42 shows a schematic of the offset orifice preparation. In this case, the simulated erosion site is towards the same side of the as that presented for the asymmetric electrode preparation. Arc skew was observed to occur towards the opposite side of the offset hole, or again, towards the constricted side of the flow. The same result as that shown in Figure 41 was observed to occur for the asymmetric orifice.

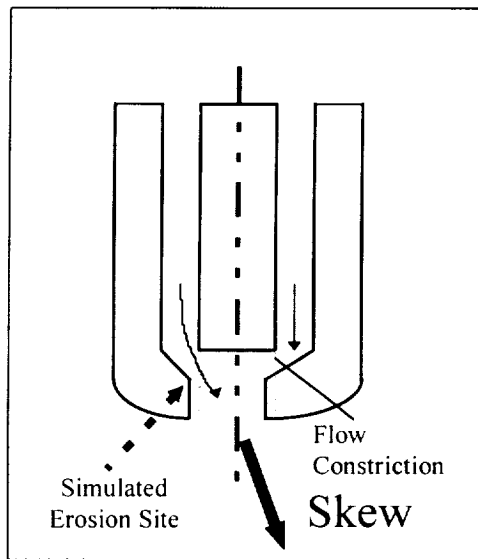


**Figure 42. Orifice Offset by a Shift of the Orifice Hole.**

Simulating electrode and orifice erosion by introducing asymmetries demonstrated that arc skew is in the direction of any constriction in the orifice flow. This

is represented by an arrow pointing in the down-rightward direction as shown in both Figure 40 and Figure 42. In both cases, the plasma gas flow seemed to be altered or blocked on the side opposite to the simulated erosion location, that is, to the constricted side. This apparently produces an asymmetric cross flow towards the constricted side or the orifice, which the arc follows. In addition, the plasma arc will concentrate at the constriction, producing the effect of additional flow blockage.

### ***Asymmetric Shielding Gas Flow***

Alterations to the plasma gas flow due to simulated asymmetry of the electrode and orifice were shown to cause arc skew. It was hypothesized that alterations to the shielding gas flow might also result in arc skew. Blockage to the shielding gas could produce a non-uniform entrainment of ambient air which could cause skewing of the plasma jet.

To test this, a carbon rod was introduced near the plasma arc in order to introduce an asymmetry in the path of the shielding gas flow. The experiment was monitored by video observation. No significant disturbances within the plasma arc region were detected in the form of arc skew. Therefore, asymmetric shielding gas flow was ruled out as a likely cause for arc skew. As in previous experiments, such as the calorimetric and arc pressure measurements, variations in shielding gas did not produce significant changes to the plasma arc. This narrowed the cause to asymmetries internal to the torch, such as asymmetries of the electrode, the orifice and the plasma gas flow.



### ***Asymmetric Pilot Arc Attachment***

Uneven attachment of the pilot arc was examined for its affect on arc skew. During operation of the plasma arc in EN and VP, the pilot arc was turned on and off. During video observations of the plasma arc, turning the pilot arc off and on could switch plasma skew off and on, as shown in Figure 43. It was of interest to observe the pilot arc under these conditions. Normally, the pilot arc operates asymmetrically between the orifice and the electrode, and arc might produce some flow asymmetry.

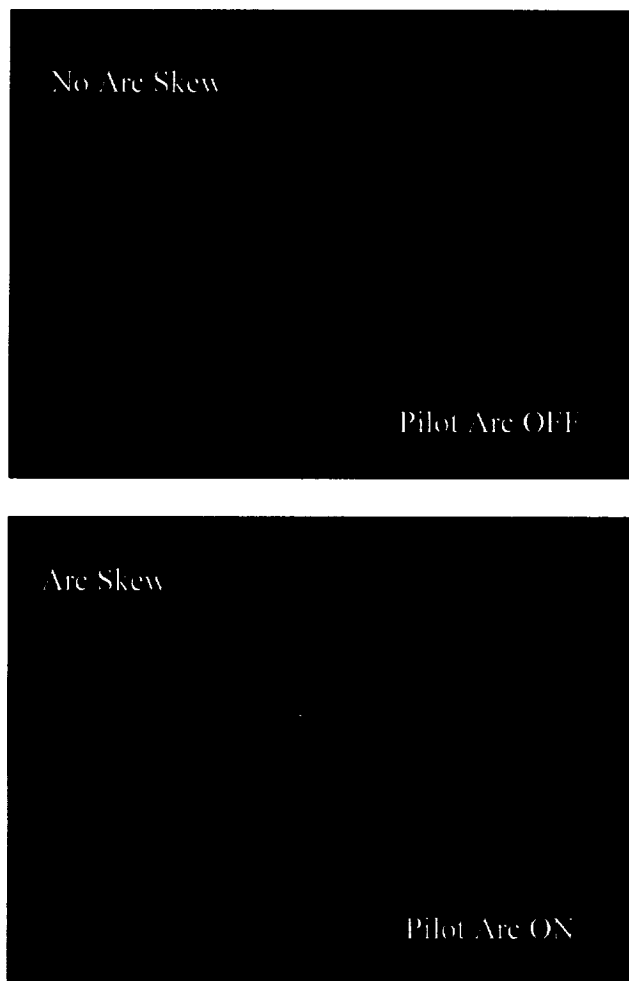


**Figure 43. Video Observation of Arc Skew During EN Operation.**



The location of the pilot arc was determined by observing the operation of the pilot arc alone by viewing into the end of the torch. Figure 44 shows the end view of the electrode and orifice with the high magnification video system. Even though the torch was designed to be self-centering, a gap between the electrode and the orifice can be seen, which indicated some initial misalignment (asymmetry). After the initially misaligned electrode and orifice were observed, the pilot arc was turned on. Figure 45 shows an end view of the welding torch during operation of the pilot arc with the electrode misalignment shown in Figure 44. It must be noted that the gap on the left hand side of Figure 44 corresponds to the upper right hand corner of Figure 45, as indicated. Attachment of the pilot arc was observed to be uneven and consistently located at the closest point between the electrode and the orifice. In addition, it was observed that the main plasma arc deflected towards the side where the pilot arc attachment occurred with main arc operation in EN and VP modes.



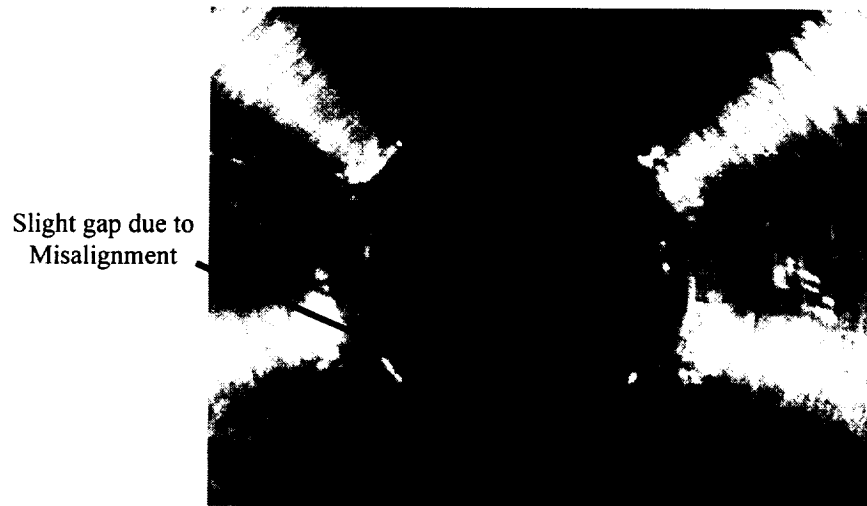


**Figure 44. Electrode and Orifice Assembly with Initial Misalignment.**

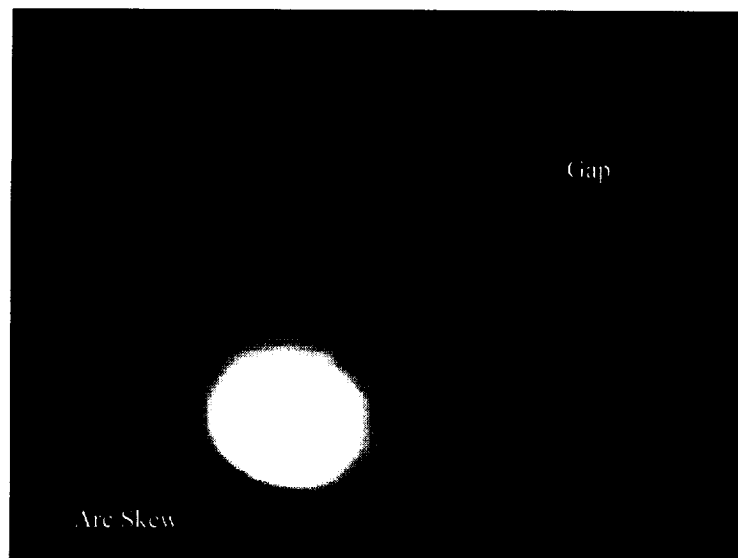


**Figure 45. Pilot Arc Operation Only.**



### ***Erosion Analysis***

Work described to this point strongly indicated that asymmetries in the electrode and orifice geometry were the main causes of arc skew. Also, long duration operation was suspected as a likely cause of asymmetry development due to deterioration of the electrode tip and orifice surfaces. Such deterioration was observed on used electrodes and orifices from NASA, as well as on ones subjected to test work as a part of this work. This prompted the design of experiments to investigate the deterioration of electrode and orifice surfaces for different operating conditions using high magnification video. Also, current flow paths for the main and pilot arc were investigated to find correlations between eroded surfaces and current paths. Parameters for three welding conditions of the EN and VP operations for the analyses are presented in Table 2. Operation was for 20 minutes at the various operating conditions onto the copper block.

<b>EN no pilot arc</b>	<b>EN with pilot arc</b>	<b>VP with pilot arc</b>
170 A Straight Polarity	170 A Straight Polarity	170 A Straight Polarity (19 ms)
		200 A Reverse Polarity (4 ms)
	22 A - pilot arc	22 A - pilot arc

**Table 2. Welding Parameters for Electrode and Orifice Analysis.**

Figure 46 shows high magnification images obtained from the erosion weld runs. The first column of images in the left portion of the figure presents the unused state of electrode and orifice surfaces, labeled as NEW. The second column shows the surfaces after running DCEN without the pilot arc. The third column shows results for DCEN operation with the pilot arc. The fourth column shows the VP run with pilot arc operation. The first row is a high magnification of the electrode tip viewed parallel to the electrode axis. The second row of images is a view of the inner orifice while the third row is a view of the outer orifice surfaces. Five annotations within Figure 46 show the main results which will be presented in the order labeled within the figure.



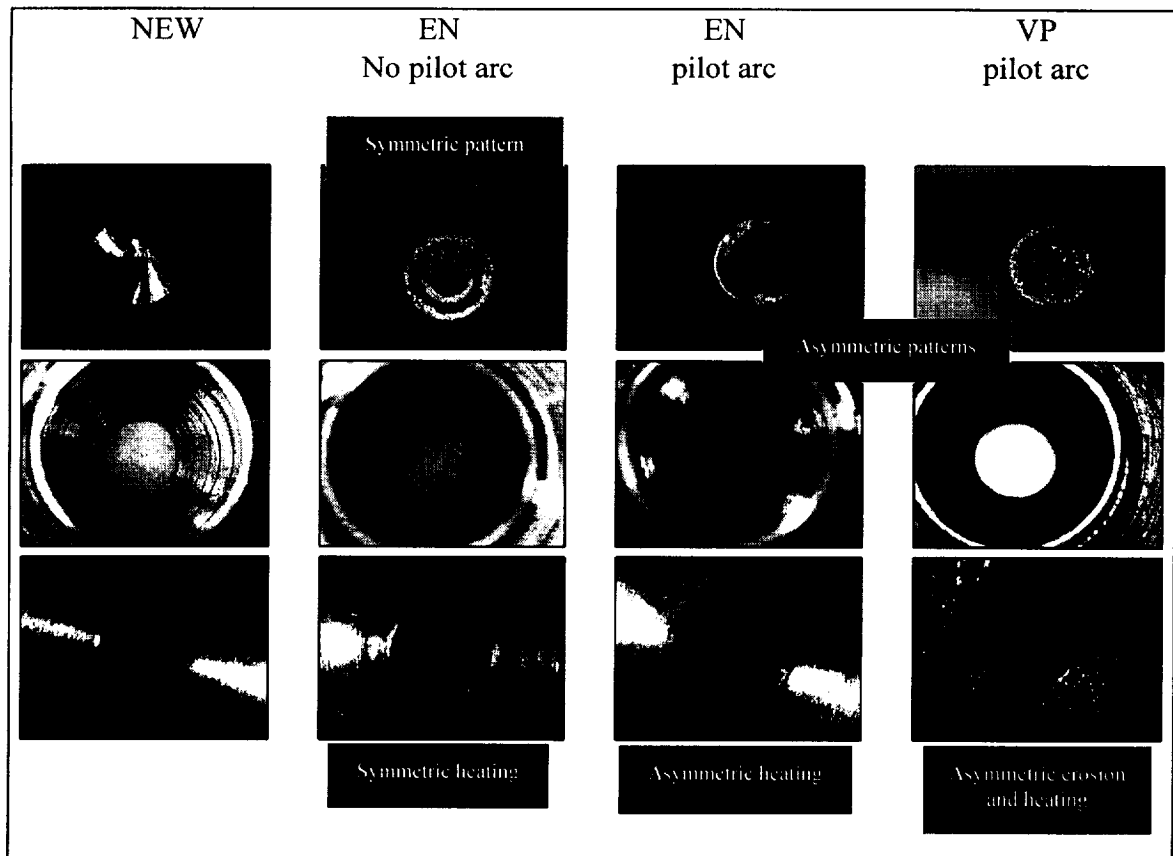


**Figure 46. Electrode and Orifice High Magnification Pictures.**

Analysis of the electrode for the DCEN case without the pilot arc, presented in the second column of Figure 46, showed the presence of a centered ring (Symmetric pattern) of electrode deterioration. This is indicative of uniform arc attachment between the electrode and the work piece, with no evidence of orifice arc attachment found within the inner or outer orifice surfaces. The current flow path for the DCEN operation was analyzed in order to correlate the arc attachment and the eroded surfaces of the electrode and orifice.



Figure 47 presents the current flow path in terms of electron flow for the EN operation. The electron symbol indicates that the directions of current flow represent electron flow around the electrical circuit, rather than the conventional current flow. In the case of electron flow, electrons are transferred from the cathode to the anode. Measurements of currents and voltages at various points in the welding circuit confirmed these current flow paths. Without the pilot arc, only the main current flows as illustrated in the figure, and a symmetric arc forms between the tungsten electrode and the work piece. Analysis of the orifice inner surface for the EN case without the pilot arc, presented in the second column of Figure 46, showed no evidence of deterioration. The outer surface had evidence of only a symmetric discoloration pattern caused by the heat dissipation.

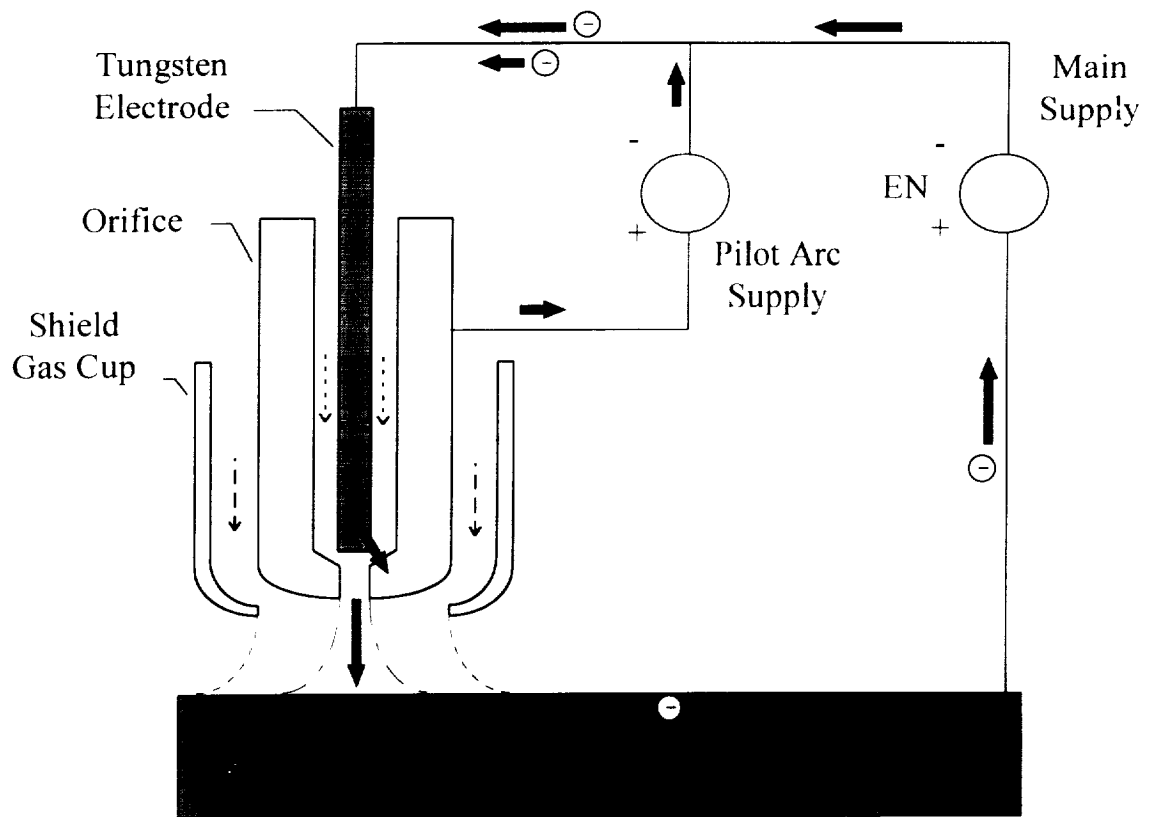


**Figure 47. EN Electron Flow.**

Analysis of the electrode tip and the inner orifice surfaces after EN operation with the pilot arc, presented in the third column of Figure 46, showed the formation of asymmetric deterioration of the electrode surface. This asymmetric deterioration can be explained by the characteristic asymmetric attachment of the pilot arc between the electrode and the orifice as was previously discussed.

In addition to the asymmetric deterioration of the electrode and orifice, the EN operation with the pilot arc, shown in the third column of Figure 46, exhibited an asymmetric heated zone on the outer orifice surface. The asymmetric heating location on

the outer orifice surface was at the same location as the asymmetric attachment of the pilot arc which produced the uneven heat deterioration of the inner orifice.

More pronounced deterioration to the electrode surface, shown in the fourth column of Figure 46, was observed for VP operation with the pilot arc. This deterioration can be related to operation during the EP portion of the VP cycle, which is known to produce higher heat loads on the electrode than EN operation. This high heat load concentration to the electrode causes localized melting of the electrode tip leading to greater rates of deterioration.

Figure 48, as in Figure 47, shows the current flow path in terms of electron flow for the EP portion of the VP cycle. Measurements of currents and voltages throughout the welding circuit confirmed the electron flow path presented in Figure 48. These measurements indicated that not all the current supplied by the main power supply was delivered to the electrode, but some current flows through the pilot arc circuit. During EP operation, the main and pilot arc supplies operate in series allowing for the voltage potential between the orifice and the workpiece to exceed the voltage between the electrode and the workpiece. Also, the pilot arc power supply operates with a ballast resistance, allowing more current to pass through the pilot circuit with the sources in series. This results in a greater current flow from the work piece to the orifice than just the pilot arc current. This contributes to a reduction in current flow and heating to the electrode during EP operation.

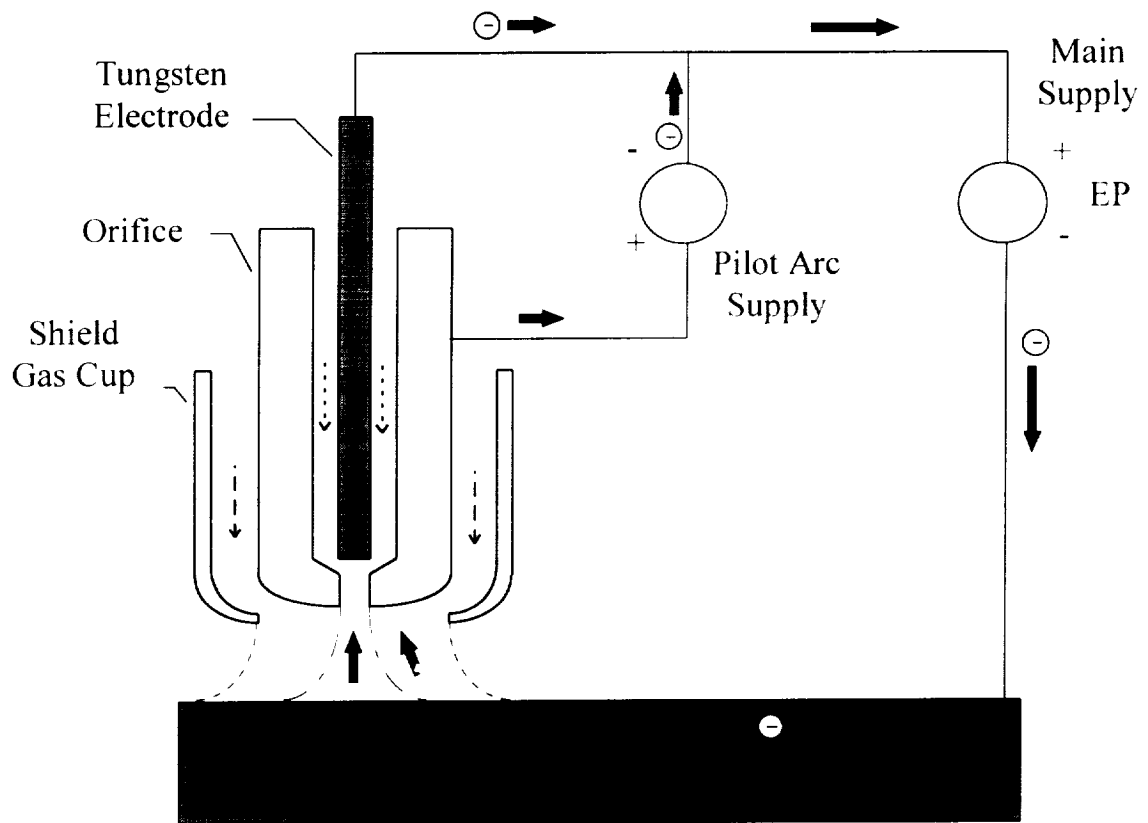


**Figure 48. EP Electron Flow.**

When comparing the outer orifice surfaces for EN and VP operation with the pilot arc, it was observed that in addition to the asymmetric heating present in the EN operation, asymmetric deterioration on the orifice outer surface was present for the VP operation as shown in the fourth column of Figure 46. Both asymmetries, the heating and surface deterioration, were associated with the operation of the pilot arc attachment. Based on the EN and EP electron flow circuits presented in Figure 47 and Figure 48, the pilot arc attachment occurred in two ways. First, there was an attachment between the

electrode and the orifice for the EN portion of the VP operation which was the same as for the EN operation already described in Figure 47. Secondly, in the case of the EP portion of the VP cycle, the pilot arc attachment occurred between the workpiece and the outer orifice surface as shown in Figure 48 by the slanted arrow pointing from the workpiece to the orifice.

It was observed during operation of the EN and VP cases with the pilot arc that the asymmetric heating of the outer orifice occurred in the same direction as the arc skew. Note that in the last row of the third and fourth columns of Figure 46, the region of the orifice surface with most deterioration due to the heat load from the main arc produced an asymmetric heating pattern. Therefore, asymmetric heating of the outer surface of the orifice is a post process indication of asymmetric operation of the pilot arc and the occurrence of arc skew.

#### **4.3 Summary of Results**

Various asymmetries within the electrode and orifice assembly of the plasma torch were found to produce of arc skew. These asymmetries were attributed to initial asymmetries in the electrode and orifice geometry, and deterioration of the electrode and orifice during the EN and VP operation with the pilot arc. Continuous EN operation without the pilot arc showed no evidence of arc skew and no post process indications of asymmetric deterioration of the electrode nor orifice.





## **5. SOLUTIONS TO ARC SKEW**

The experimental results have shown that asymmetries attributed to initial misalignment of the electrode and orifice, pilot arc operation, and asymmetric deterioration of the electrode and orifice can be significant causes of arc skew. In addition, the deterioration studies have shown that the reverse polarity of the VP cycle is mainly responsible for erosion of the electrode surface. During the EP cycle, electrons flow from the workpiece to the electrode carrying high heat loads towards the electrode surface causing localized melting, eroding the electrode. If erosion is asymmetric within the welding torch, arc skew can develop. Since the pilot arc is inherently asymmetric, operation of the pilot arc tends to promote asymmetric erosion.

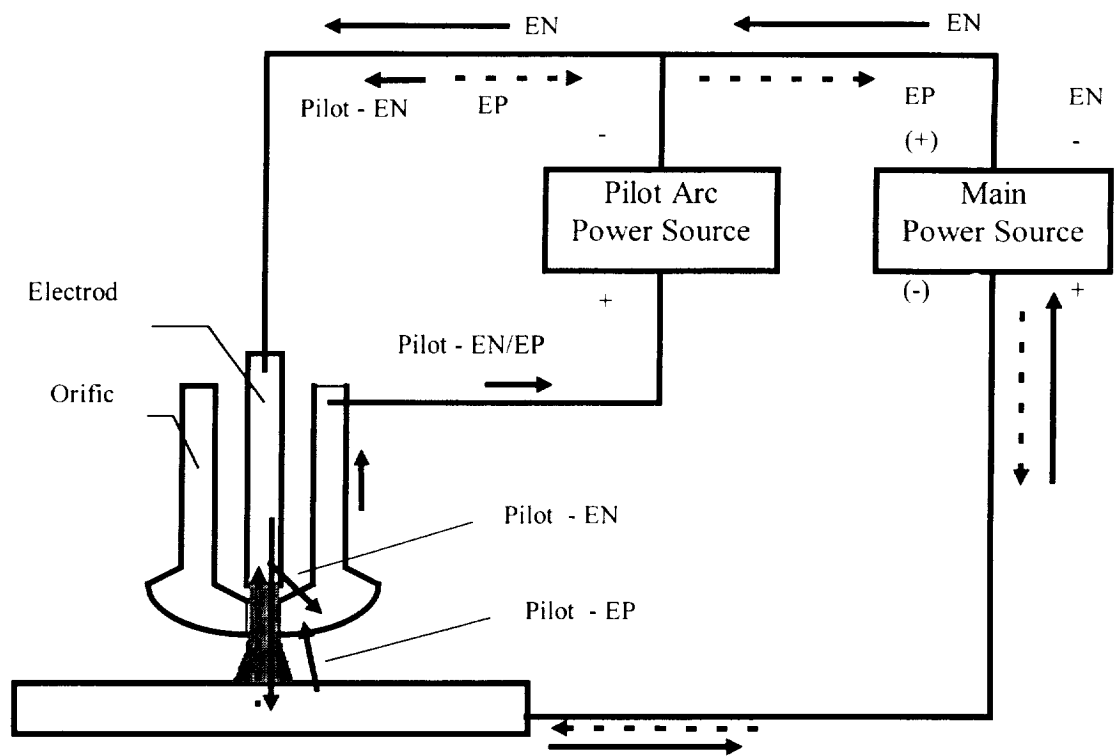
The analysis of the eroded surfaces, in conjunction with the analysis of current flow paths for the EN and EP portions of the VP cycle, led to the idea of attempting to control the current paths within the welding torch for the purpose of minimizing deterioration and reducing the tendency for development of skew conditions. It was believed that diodes could be used in the welding circuit to control the current flow paths in order to decrease the erosion within the torch components. For example, by reducing the EP current flow to the electrode, it was believed that asymmetries due to erosion

could be reduced, allowing for longer weld time without the need for replacement of the electrode and orifice. As a result of this, studies were conducted to investigate the modification of current paths during EP operation by placing diodes in the electrical circuit. The principle of this idea was to bypass the EP current flow around the electrode to a second electrode or to the orifice surface in order to reduce the erosion associated with the EP portion of the VP cycle.

### **5.1 Current Paths Modification**

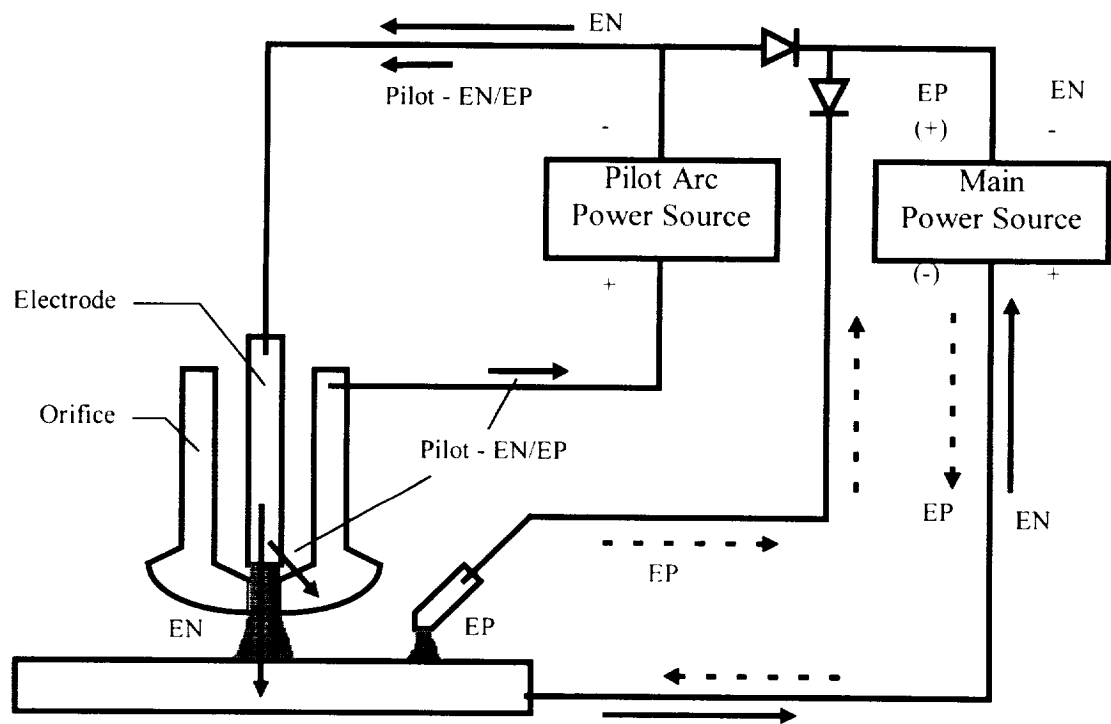
Two configurations of electrical connections using diodes were designed to control the current paths. These configurations will be referred to as “second electrode” and “orifice” configurations. The second electrode configuration used an external GTAW torch for EP operation for the purpose of taking the heat load associated with the EP away from the main electrode and into the GTAW torch electrode. The orifice method was designed so that the orifice would carry all EP current flow and take the EP heat from the electrode.

The electrical schematic for conventional variable polarity is shown in Figure 49 and it will be used as a reference for comparison with the second electrode and orifice method electrical circuits. As previously discussed, the modified current flow paths were confirmed by taking measurements of currents and voltages throughout the electrical circuit. Note that the EP pilot current flows from the work piece to the orifice. The electrode current during EP is reduced by the amount of the pilot current.



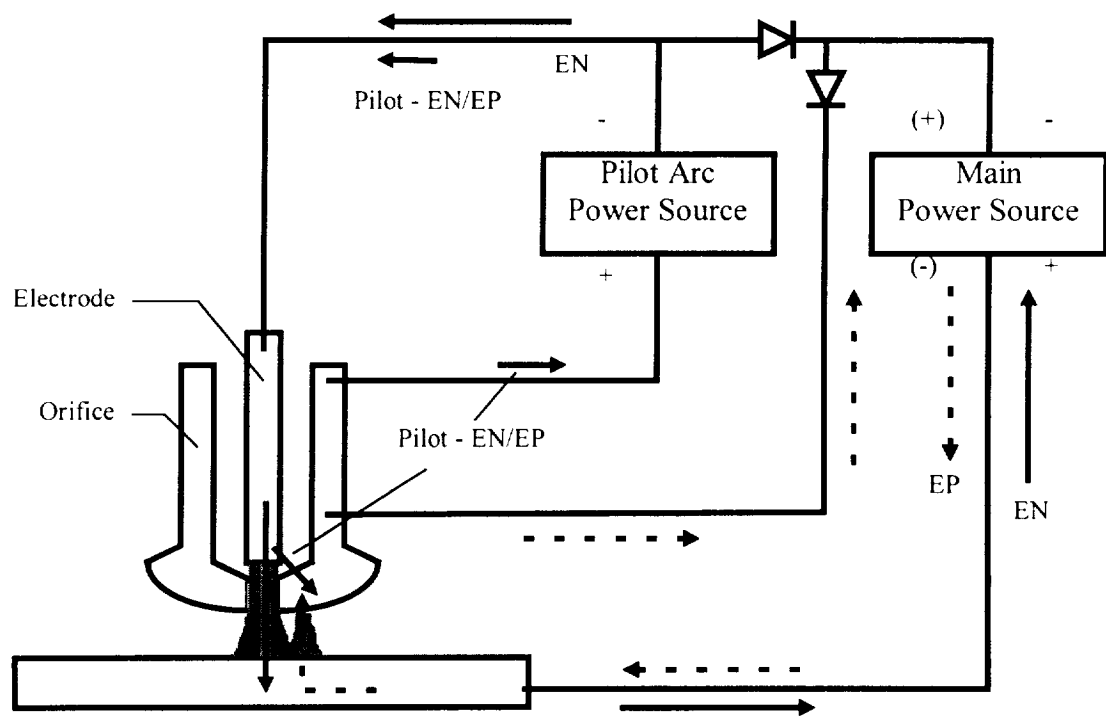
**Figure 49. Conventional Variable Polarity Electron Flow.**

Figure 50 shows the electrical schematic of the setup with the use of a second electrode. Note that the placement of the diodes within the electrical circuit only allows electrons to flow from the main electrode to the workpiece during the EN cycle. During the EP cycle main current electrons will only flow from the workpiece to the second electrode. In this case, the pilot arc operates from the electrode to the orifice during both EP and EN operation. The second electrode consisted of an externally placed GTAW torch electrically connected through one of the diodes and held near the main VPPAW torch, such that the second electrode was very near the axis of the VPP torch.



**Figure 50. Electrical Schematic for The Second Electrode.**

Figure 51 shows the electrical schematic for the orifice setup. During the EN cycle, electrons flow in the same manner as they did for the second electrode circuitry. A change in the EP cycle is produced by making an electrical connection to the body of the torch where the pilot arc is also connected. Therefore, during the EP cycle, the main current electrons flow between the work piece and the outer orifice surface.



**Figure 51. Electrical Schematic for the Orifice Connection.**

## 5.2 Circuit Components

Both electrical circuits were designed using two high power diodes. The two diodes used were International Rectifier 1N4056's. One diode was cathode-to-stud mounted while the other was anode-to-stud mounted. The diodes were rated at 275 Amperes at a maximum temperature of 120°C with a  $V_{rms}$  of a 1000 Volts. The diodes were mounted on an aluminum heat sink, shown in Figure 52, with a fan placed at one end of the heat sink fixture for cooling purposes. A knife switch was used to isolate the diodes and the main power supply from the high frequency starter during pilot arc initiation. A schematic of the diode configuration with the knife switch is shown in Figure 53.

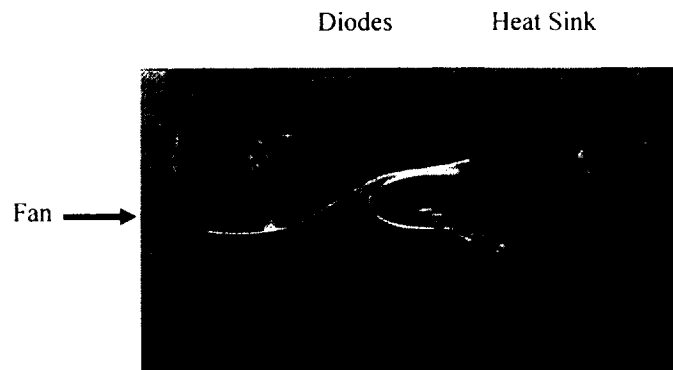


**Figure 52. Diodes Mounted on a Heat Sink.**

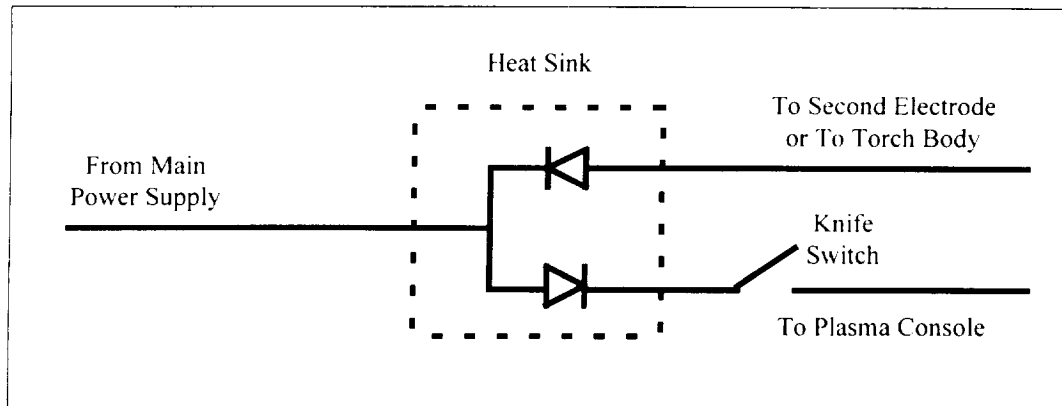


**Figure 53. Electrical Schematic for Diode Assembly.**

### **5.3 Experimental Procedures**

Experiments for the second electrode and the orifice configurations were designed to look at the deterioration of the electrode and orifice to compare them with conventional variable polarity. The torch was operated on the chilled copper block for of 10 minutes of VP for each configuration. Before and after high magnification images were taken of the electrode and orifice for the various configurations.

Analysis of the images similar to that mentioned previously were carried out on the images of the electrode and the orifice. In addition, calorimetry was performed on these two configurations to compare to the results with conventional VP.

Figure 54 shows an illustration of the setup used for the second electrode. This depicts the EN cycle operating between the VPPAW torch and the workpiece while the EP cycle operates between the GTAW torch (at the right) and the workpiece.

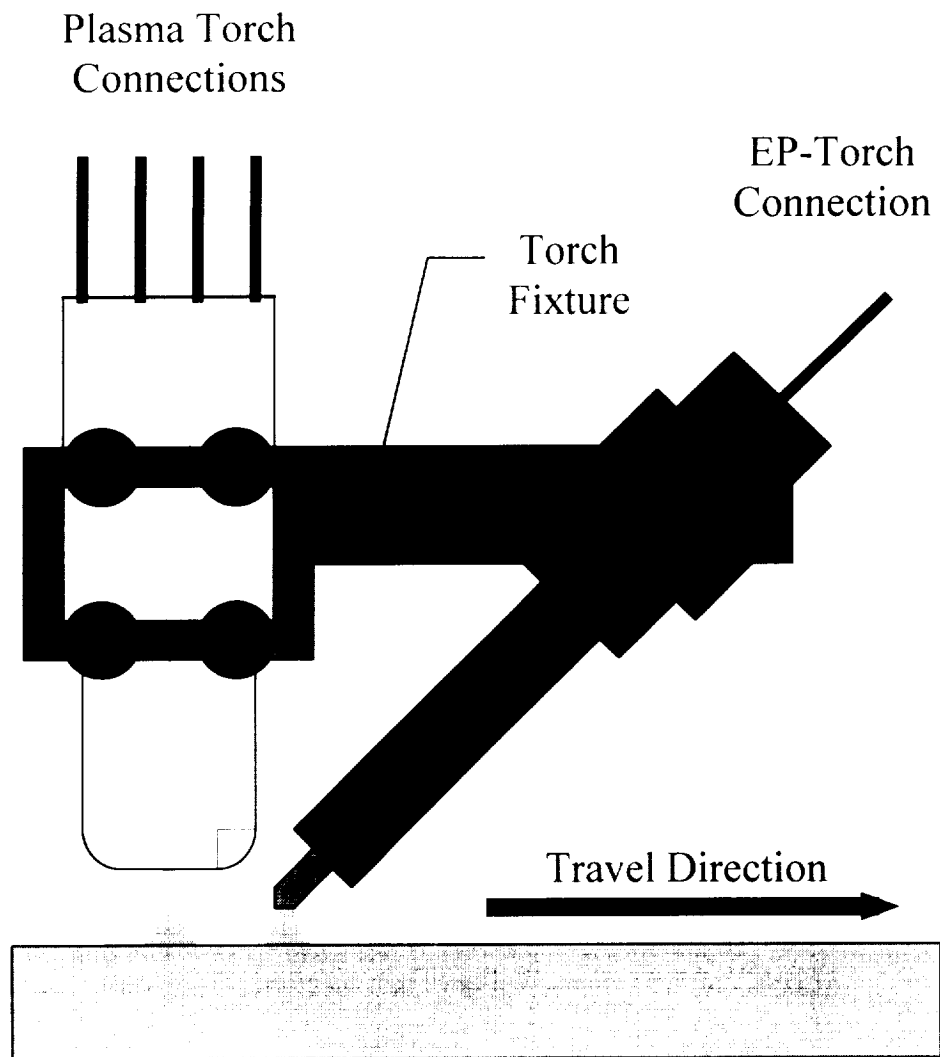


**Figure 54. Schematic of Second Electrode.**



## 5.4 Welding Conditions

Welding parameters were used for experimentation with the second electrode and the orifice connections that were similar to those for earlier tests. The EN cycle was set at 170 Amperes (~30 V) for a duration of 19 milliseconds. The EP cycle was set at 200 Amperes (~40 V) for a duration of 4 milliseconds. The pilot arc was set at 22 Amperes. A 5 LPM plasma gas flow and a 10 LPM shielding gas flow were used. A  $\frac{3}{8}$ <sup>th</sup> inch standoff distance, a  $\frac{1}{8}$ <sup>th</sup> inch diameter 2% thoriated tungsten, and a  $\frac{1}{8}$ <sup>th</sup> inch diameter orifice with a 0.145 inch electrode setback were used. The welding arc was run over the chilled copper block for 10 minutes.

## 5.5 Results and Discussion

### *Second Electrode*

In Figure 55, the results from the erosion analysis photographs with the second electrode configuration are compared to the erosion analysis photographs with the conventional VP operation. Deterioration of the electrode was significantly reduced by the second electrode configuration as seen in the second and third columns of the first row of Figure 55. This was due to the absence of EP current flow to the plasma torch electrode as the electrode flow was redirected to the second electrode during the EP cycle. The asymmetric erosion on the electrode surface for the second electrode, as seen in the

third column of the first row of Figure 55, appeared similar in shape to the asymmetric erosion on the electrode surface of the EN operation with the pilot arc (seen in the third column of the first row of Figure 46). Since deterioration of the electrode surface by the EP cycle was decreased by the second electrode, the current capacity of the welding torch could be increased with the second electrode configuration.

Asymmetric erosion within the inner orifice surface, shown in the second and third columns of the first row of Figure 55, seemed to show no change with the introduction of the second electrode configuration.

It can also be seen that the deterioration of the outer orifice surface associated with the cleaning action on the EP cycle was eliminated by the second electrode, as seen in the third column of the fourth row, when compared to the second column of Figure 55. Asymmetric heating of the outer orifice was still present for the second electrode configuration. This can be attributed to the pilot arc operation.

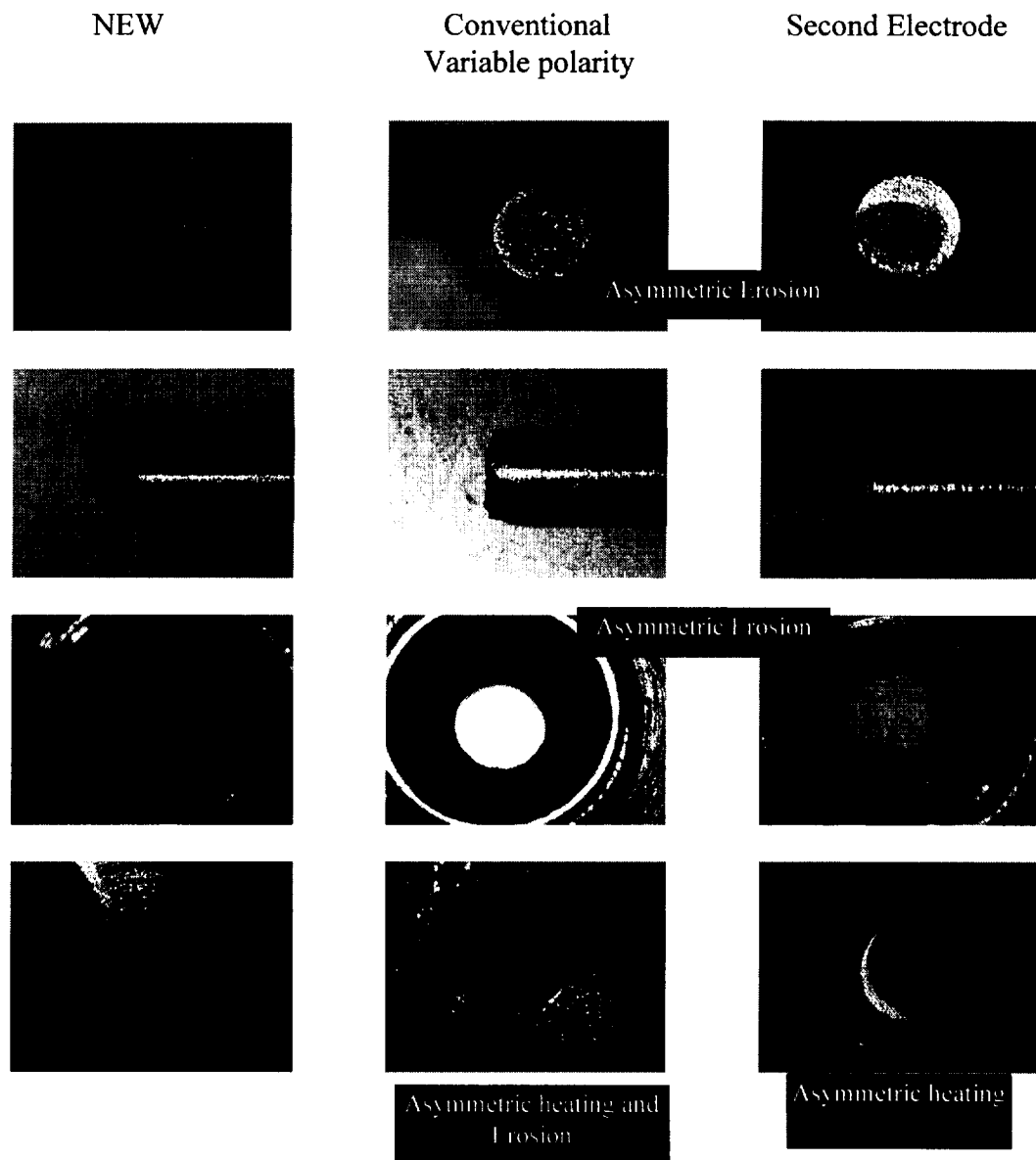


**Figure 55. Electrode and Orifice Deterioration with The Second Electrode.**



### ***Orifice Electrode***

For using the orifice as the second electrode, the electrical connection for the EP cycle was to the torch body. Figure 56 presents the deterioration results for the orifice electrode configuration. Similar to the findings from the second electrode tests, deterioration of the electrode tip surface was significantly reduced when compared to the conventional VP operation with the pilot arc, as seen in comparing the second and third columns of the first row of Figure 56. The deterioration of the outer orifice surface was observed to be similar for both the torch body and the VP operation, as seen in the second and third columns of the fourth row. This deterioration was associated with EP operation and also resulted in asymmetric heating of the outer orifice surface. The inner orifice surface with the orifice electrode configuration showed more evidence of deterioration as can be seen in the third column of the third row. Greater deterioration of the orifice would be expected since it is receiving all of the EP current flow, rather than an amount related to the pilot current for conventional VP. It is not clear why the greater deterioration is on the inner orifice rather than the outer orifice, since it would seem logical that the outer orifice would receive the current.



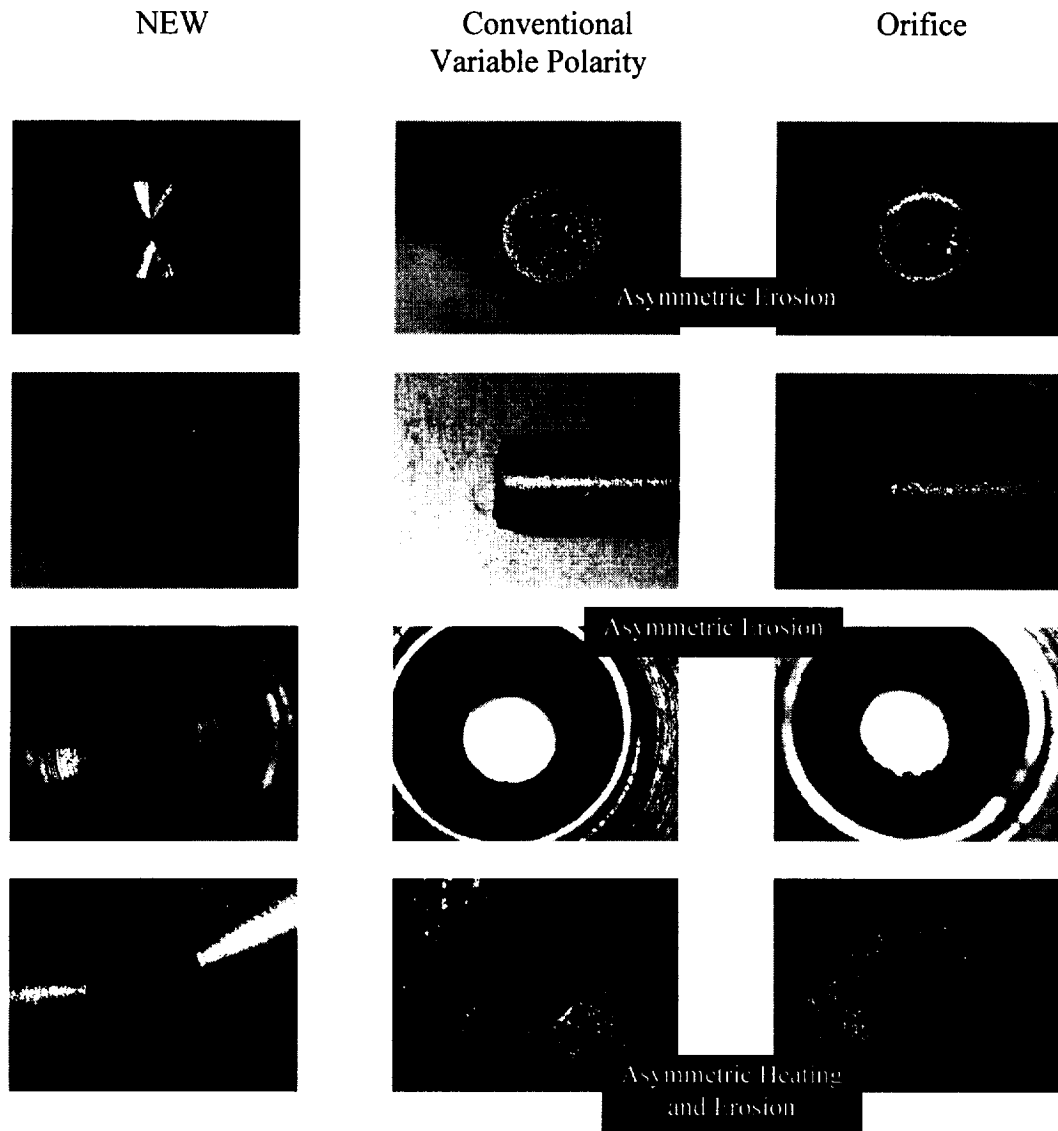


**Figure 56. Electrode and Orifice Erosion for the Orifice Electrode.**





### ***Calorimetric Measurements***

Calorimetric measurements on the second electrode and orifice electrode configurations were compared to the conventional VP configuration measurements. Figure 57 presents the heat load measurements for this comparison. The results show a decrease in the work heat load with VP operation from 2987 Watts to 2676 Watts for the second electrode and to 2771 Watts for the orifice electrode. An increase in heat loss of the VP operation from 616 to 1010 Watts for the second electrode operation was observed. This increase in lost heat load for the second electrode operation can be attributed to the inability to measure the heat load to the GTAW torch (second electrode). The heat load to the torch was found to be around 100 watts lower for the second electrode configuration than for the VP operation since the heat load associated with the EP cycle was diverted to the second electrode by the use of the diodes. It is not entirely clear why the torch heat load dropped by only 100 watts, while the main redirection of heat was from the work piece to lost heat. Nevertheless, the deterioration of the electrode was decreased.

Even though the orifice electrode configuration showed the highest torch heat load, deterioration of the electrode was reduced. A higher torch heat load was measured for the orifice electrode configuration than with conventional VP operation. It is not clear why this increase was so significant, since the heat load was presumably only redirected from the electrode tip to the orifice, which remains a part of the torch heating.

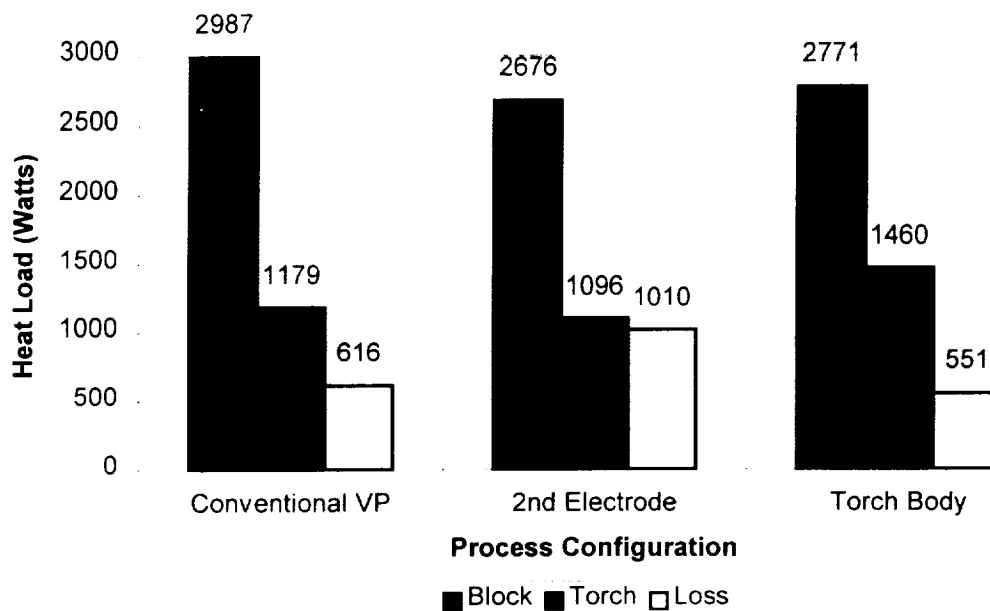


**Figure 57. Heat Load Comparison between Conventional VP, Second Electrode and Orifice Electrode.**

### *Summary of Results*

In summary, the most significant results from using diodes in the welding circuit were the reduction of the deterioration of the electrode for both the second electrode and orifice electrode configurations, and the reduction of erosion of the outer orifice for the second electrode configuration. These investigations have dealt mainly with the erosion analysis. They were performed on a chilled copper block, and experimentation under actual welding conditions was not performed.

## 6. MODELING OF PLASMA TORCH AND EXTERNAL JET FLOWS

The basic equations that govern flowing plasmas (under the continuum approximation) are essentially the compressible Navier-Stokes equations. These plasmas are typically composed of electrons, ions, neutral atoms and molecules, ions and molecular ions. A complete description of these flowing plasmas requires the flow equations to be coupled with an energy equation (or several energy equations), species continuity equations and Maxwell's equations. The solution of this set of equations is indeed a daunting task. Variable properties, presence of  $\vec{j} \times B$  body forces, Ohmic heating, species diffusion, chemical reactions with ionization/recombination, rotational, vibrational and electronic mode non-equilibrium make these system of equations extremely non-linear and stiff, making them very difficult to solve.

This chapter discusses the formulation of problems concerning plasma flows in general. We begin by describing the vector form of the governing equations first. These general equations are then rewritten in cylindrical coordinates assuming axi-symmetry. The 2-D form of these equations is then applied to the geometric configurations relevant for this work. This is followed by a discussion on non-dimensionalization of these equations. Transport properties essential to the description of these plasmas are discussed next. This chapter is finally concluded with a discussion of certain general initial and boundary conditions used in modeling plasma flows.

## 6.1 Vector Forms of the Governing Equations

Vector equations in conservative form describing non-equilibrium plasmas are described in this section [Ref. 30, Ref. 31]. Equation ( 1) describes the continuity equation.

$$\frac{\partial \rho}{\partial t} + \nabla \cdot (\rho \vec{v}) = 0 \quad (1)$$

$$\frac{\partial}{\partial t} (\rho \vec{v}) + \nabla \cdot \rho \vec{v} \vec{v} = -\nabla p + \vec{F} - \nabla \times [\mu (\nabla \times \vec{v})] + \nabla \left[ \frac{4}{3} \nabla \cdot \vec{v} \right] \quad (2)$$

Equation ( 2) describes the momentum equations. These equations are also known as the Navier-Stokes equations.  $\vec{F}$  on the right hand side of equation ( 2) denotes the net Lorentz body force per unit volume. These equations must be supplemented by an equation for conservation of energy for each species.

$$\frac{\partial}{\partial t} e_{T_i} + \nabla \cdot ([e_{T_i} + p_i] \vec{v}) = -\nabla \cdot \vec{q} - \nabla \cdot \vec{q}_r + q''' + \mu \Phi + \sum_j \Delta E_{ij} \quad (3)$$

The above form of the energy equation can be applied to a species  $i$  with a translational temperature  $T_i$ . The term  $-\nabla \cdot \vec{q}$  on the right hand side of equation ( 3) is the net energy per unit volume transferred by heat conduction and diffusion,  $-\nabla \cdot \vec{q}_r$  is the net energy per unit volume transferred by radiation. and  $q'''$  is the energy generated per unit time per unit volume. For a conducting fluid,  $q''' = \vec{j} \cdot \vec{E}$  under the MHD approximation [Ref. 30].  $\mu \Phi = \vec{v} \cdot \nabla \cdot \vec{\tau}$  is the the rate at which work is done by surface forces.  $\sum_j \Delta E_{ij}$  represents the energy exchange per unit volume between the species  $i$  and species  $j$ . In the above energy equation, each specie  $i$  is assumed to be described by a translational temperature  $T_i$ . This inherently assumes that the velocity distribution function is locally described by the Maxwell-Boltzmann distribution. If it is assumed that a single temperature characterizes all the heavy particles, then  $T_i$  in the various

energy equations would be replaced by a single temperature  $T_h$ . A similar equation can then be written for the electrons. In this work, a single temperature is assumed wherein heavy particles and electrons are described by a single temperature,  $T$ .

In addition to the equations governing the conservation of mass, momentum and energy, it is necessary to describe the time-evolution of the various species in the plasma.

Species in a plasma may be monatomic or polyatomic. The monatomic species have only one internal mode - that of electronic excitation. Polyatomic species on the other hand, have states of rotation and vibration in addition to electronic excitation. Each of these different internal states can be treated as a specie with a separate equation governing its evolution. The species conservation equations for monatomic and polyatomic species are:

$$\frac{\partial n_m}{\partial t} + \nabla \cdot (n_m \vec{v}) + \nabla \cdot \left( -n_m \mu_m \vec{E}' + \frac{D_m}{k_b T_m} \nabla \cdot (n_m k_b T_m) \right) = \dot{n}_m \quad (4)$$

$$\begin{aligned} \frac{\partial n_{iv}}{\partial t} + \nabla \cdot (n_{iv} \vec{v}) + \nabla \cdot \left( -n_{iv} \mu_{iv} \vec{E}' + \frac{D_{iv}}{k_b T_{iv}} \nabla \cdot (n_{iv} k_b T_{iv}) \right) \\ = VT_{i,v} + VV_{i,v} + SRD_{i,v} + \dot{n}_{i,v} \end{aligned} \quad (5)$$

where  $\dot{n}_m$  and  $\dot{n}_{i,v}$  represent the net rate of production of monatomic and diatomic species by chemical processes or ionization and recombination. A similar equation is also written for the electron concentration.

## 6.2 Governing Equations in 2-D Axisymmetric Form

For our present purposes, we consider the governing equations in cylindrical polar coordinates in 2-D axisymmetric form. A single temperature is used to describe all the

components of the plasma, so that there is only one energy equation. The continuity equation, radial, axial and azimuthal components of the momentum equations, the energy equation and the species (monatomic and diatomic) equations, are discussed next in dimensional, conservative form.

Conservation of mass is expressed by the continuity equation:

$$\frac{\partial \rho^*}{\partial t^*} + \frac{1}{r^*} \frac{\partial}{\partial r^*} (r^* \rho^* u^*) + \frac{\partial}{\partial x^*} (\rho^* w^*) = 0 \quad (6)$$

where, the asterisks denote dimensional quantities. The radial, azimuthal and axial components of momentum are:

$$\begin{aligned} \frac{\partial}{\partial t^*} (\rho^* u^*) + \frac{1}{r^*} \frac{\partial}{\partial r^*} (r^* \rho^* u^{*2}) + \frac{\partial}{\partial x^*} (\rho^* u^* w^*) - \frac{\rho^* v^{*2}}{r^*} \\ = -\frac{\partial p^*}{\partial r^*} + \frac{\partial}{\partial r^*} \left[ 2\eta^* \frac{\partial u^*}{\partial r^*} - \frac{2}{3} \eta^* \nabla \cdot \vec{u}^* \right] - j_x^* B_\theta^* \\ + \frac{\partial}{\partial x^*} \left[ \eta^* \left( \frac{\partial u^*}{\partial x^*} + \frac{\partial w^*}{\partial r^*} \right) \right] + \frac{2\eta^*}{r^*} \left( \frac{\partial u^*}{\partial r^*} - \frac{u^*}{r^*} \right) \end{aligned} \quad (7)$$

$$\begin{aligned} \frac{\partial}{\partial t^*} (\rho^* v^*) + \frac{1}{r^*} \frac{\partial}{\partial r^*} (r^* \rho^* u^* v^*) + \frac{\partial}{\partial x^*} (\rho^* v^* w^*) - \frac{\rho^* u^* v^*}{r^*} \\ = \frac{\partial}{\partial r^*} \left[ \left( \eta^* \frac{\partial v^*}{\partial r^*} - \frac{v^*}{r^*} \right) \right] + \frac{\partial}{\partial x^*} \left[ \eta^* \frac{\partial u^*}{\partial x^*} \right] \\ + \frac{2\eta^*}{r^*} \left( \frac{\partial v^*}{\partial r^*} - \frac{v^*}{r^*} \right) \end{aligned} \quad (8)$$

$$\begin{aligned} \frac{\partial}{\partial t^*} (\rho^* w^*) + \frac{1}{r^*} \frac{\partial}{\partial r^*} (r^* \rho^* u^* w^*) + \frac{\partial}{\partial x^*} (\rho^* w^{*2}) \\ = -\frac{\partial p^*}{\partial x^*} + \frac{\partial}{\partial x^*} \left[ 2\eta^* \frac{\partial w^*}{\partial x^*} - \frac{2}{3} \eta^* \nabla \cdot \vec{u}^* \right] - j_r^* B_\theta^* \\ + \frac{1}{r^*} \frac{\partial}{\partial r^*} \left[ \eta^* r^* \left( \frac{\partial u^*}{\partial x^*} + \frac{\partial w^*}{\partial r^*} \right) \right] \end{aligned} \quad (9)$$

In the above equation,  $u, v$  and  $w$  are the radial, azimuthal and axial components of velocity respectively. The energy equation can be written as:

$$\begin{aligned}
& \frac{\partial e_T^*}{\partial t^*} + \frac{1}{r^*} \frac{\partial}{\partial r^*} ([e_T^* + p^*] u^* r^*) + \frac{\partial}{\partial x^*} ([e_T^* + p^*] w^*) \\
&= \frac{1}{r^*} \frac{\partial}{\partial r^*} \left( k^* r^* \frac{\partial T^*}{\partial r^*} \right) + \frac{\partial}{\partial x^*} \left( k^* \frac{\partial T^*}{\partial x^*} \right) \\
&+ \eta^* \Phi^* + j_r^* w^* B_\theta^* - j_x^* u^* B_\theta^* + \frac{j_r^{*2} + j_x^{*2}}{\sigma}
\end{aligned} \tag{10}$$

The energy equation is written describing the transport of total energy, i.e. internal energy + kinetic energy, under the assumption of a single temperature (i.e. the electrons are assumed to have the same mean thermal energy as the heavy particles or the ions). This is not strictly true as the electrons lose only a fraction of their energy per elastic collision. A two-temperature model would entail solving another equation governing the energy conservation for the electrons. The aforementioned energy equation would then represent conservation of energy for heavy particles. The electron energy equation and the heavy-particle energy equation can then be coupled to each other via the rate of electron energy loss per unit volume, due to collisions with heavy particles. Here again, as in the conservation equations for momentum, the LHS represents convective terms, while the RHS describes the effects of thermal conduction in the axial and radial directions, viscous dissipation and Ohmic heating respectively. In the equations given here, radiative losses are neglected. In the above equation (3),  $e_T^*$  is given by  $e^* + \rho^*(u^{*2} + v^{*2} + w^{*2})/2$  where  $e^*$  is the internal energy per unit volume given by

$$e^* = 3/2 n_T^* k_b T^* + \sum_{i=1}^{N_d} f_i^* n_i^* k_b T^* / 2 + \sum_{i=1}^{N_d} \sum_{v=0}^{V_{max}} n_{i,v}^* E_{i,v}^* + \Delta \epsilon^*.$$

$\Delta \epsilon$  allows for the change of reference state (i.e. this term is the energy of formation per unit volume from chemical reactions or change in datum in molecular energy

exchanges).  $p^*$  is defined as  $p^* = n_T^* k_b T^*$ . In the energy equation,  $\Phi^*$  is the dissipation function given by,

$$\begin{aligned} \Phi^* = 2 & \left[ \left( \frac{\partial u^*}{\partial r^*} \right)^2 + \left( \frac{u^*}{r^*} \right)^2 + \left( \frac{\partial w^*}{\partial x^*} \right)^2 \right] + \left( \frac{\partial v^*}{\partial x^*} \right)^2 + \left( \frac{\partial u^*}{\partial x^*} + \frac{\partial w^*}{\partial r^*} \right)^2 \\ & + \left( \frac{\partial v^*}{\partial r^*} - \frac{v^*}{r^*} \right)^2 - \frac{2}{3} \left( \frac{\partial u^*}{\partial r^*} + \frac{u^*}{r^*} + \frac{\partial w^*}{\partial x^*} \right)^2, \end{aligned}$$

Having described the equations conserving mass, three components of momentum and energy, the equations describing the time evolution of the individual species (monatomic and diatomic) in the flowing gas are given next. Electronic states of monatomic and diatomic species are not considered in this work, although the present formulation allows their inclusion. Continuity for the monatomic species is:

$$\begin{aligned} \frac{\partial n_m^*}{\partial t^*} + \frac{1}{r^*} \frac{\partial}{\partial r^*} (u^* n_m^* r^*) + \frac{\partial}{\partial x^*} (n_m^* w^*) + \frac{1}{r^*} \frac{\partial}{\partial r^*} \left( -r^* n_m^* \mu_m^* \bar{E}_r^* - \frac{r^* D_m^*}{k_b T^*} \frac{\partial}{\partial r^*} (n_m^* k_b T^*) \right) \\ + \frac{\partial}{\partial x^*} \left( -n_m^* \mu_m^* \bar{E}_x^* - \frac{D_m^*}{k_b T^*} \frac{\partial}{\partial x^*} (n_m^* k_b T^*) \right) = \dot{n}_m^* \end{aligned} \quad (11)$$

and for the diatomic species is:

$$\begin{aligned} \frac{\partial n_{i,v}^*}{\partial t^*} + \frac{1}{r^*} \frac{\partial}{\partial r^*} (u^* n_{i,v}^* r^*) + \frac{\partial}{\partial x^*} (n_{i,v}^* w^*) \\ + \frac{1}{r^*} \frac{\partial}{\partial r^*} \left( -r^* n_{i,v}^* \mu_{i,v}^* \bar{E}_r^* - \frac{r^* D_{i,v}^*}{k_b T^*} \frac{\partial}{\partial r^*} (n_{i,v}^* k_b T^*) \right) \\ + \frac{\partial}{\partial x^*} \left( -n_{i,v}^* \mu_{i,v}^* \bar{E}_x^* - \frac{D_{i,v}^*}{k_b T^*} \frac{\partial}{\partial x^*} (n_{i,v}^* k_b T^*) \right) \\ = VT_{i,v} + VV_{i,v} + SRD_{i,v} + \dot{n}_{i,v}^* \end{aligned} \quad (12)$$

Detailed expressions for the VV, VT and the SRD terms are given in [Ref. 32]. The terms  $\dot{n}_m^*$  and  $\dot{n}_{i,v}^*$ , describe the net production of a particular component due to chemical reactions or molecular collisional exchange processes.



### 6.3 Non-Dimensional Forms of the Governing Equations

The governing equations described in the previous section are solved after first writing them in non-dimensional form. One advantage of doing so is that characteristic parameters of interest can be varied independently. Another is the control of round-off errors during the numerical calculation. The reference quantities used in this study are  $P_{ref}$  (a reference pressure equal to the stagnation pressure in the plenum of the torch; this  $P_{ref}$  takes on different values for different mass-flow rates) ,  $T_{ref}$  (a reference temperature set equal to 10,000 K),  $l_{ref}$  (a reference length set equal to 3.175 mm) and  $B_{ref}$  (based on the total current prescribed as can be seen below). All other non-dimensionalizing quantities can be normalized using these reference values. The choice of  $l_{ref}$  is based on a characteristic length of the geometric configuration under study (a length or diameter).  $P_{ref}$  is usually the stagnation pressure. The reference temperature is chosen arbitrarily to be 10,000 K. The reference velocity is based on the isentropic speed of sound at the reference temperature. This choice of non-dimensionalization differs from convention [Ref. 33] but is closely related to those used in [Ref. 34]. Since, in general, the properties such as thermal conductivity and viscosity are locally varying (and in most instances by as much as orders of magnitude) in reacting flows, non-dimensionalization using quantities such as local frozen speed of sound [Ref. 35], pressure etc., are neither useful nor relevant. From the foregoing definitions,

$$P_{ref} = n_{ref} k_b T_{ref} = \rho_{ref} k_b T_{ref}$$

$$u_{ref} = \gamma R T_{ref}$$

It must be pointed out here that  $\gamma$  in the above definition is not the ratio of the specific

heats, but is a fixed value of 5/3. This arises as a result of expressing the internal energy  $e$  as the sum of the translational energies of all components (monatomic and diatomic) and the internal energies separately. For isentropic flow of a monatomic gas,  $\gamma$  is indeed equal to 5/3. In addition to these non-dimensionalizing factors, the magnetic transport equation is non-dimensionalized by  $B_{ref}$ , defined as

$$B_{ref} = \frac{\mu_o I}{2\pi r_c}$$

Based on these non-dimensionalized quantities the governing equations after non-dimensionalizing are as follows:

$$\frac{\partial \rho}{\partial t} + \frac{1}{r} \frac{\partial}{\partial r}(r\rho u) + \frac{\partial}{\partial x}(\rho w) = 0 \quad (13)$$

$$\begin{aligned} & \frac{\partial}{\partial t}(\rho u) + \frac{1}{r} \frac{\partial}{\partial r}(r\rho u^2) + \frac{\partial}{\partial x}(\rho uw) - \frac{\rho v^2}{r} \\ &= -\frac{3}{5} \frac{\partial p}{\partial r} + \frac{\partial}{\partial r} \left[ 2\eta \frac{\partial u}{\partial r} - \frac{2}{3} \eta \nabla \cdot \vec{u} \right] - (jbar) j_x B_\theta \\ &+ \frac{\partial}{\partial x} \left[ \eta \left( \frac{\partial u}{\partial x} + \frac{\partial w}{\partial r} \right) \right] + \frac{2\eta}{r} \left( \frac{\partial u}{\partial r} - \frac{u}{r} \right) \end{aligned} \quad (14)$$

$$\begin{aligned} & \frac{\partial}{\partial t}(\rho v) + \frac{1}{r} \frac{\partial}{\partial r}(r\rho uv) + \frac{\partial}{\partial x}(\rho vw) - \frac{\rho uv}{r} \\ &= \frac{\partial}{\partial r} \left[ \left( \eta \frac{\partial v}{\partial r} - \frac{v}{r} \right) \right] + \frac{\partial}{\partial x} \left[ \eta \frac{\partial u}{\partial x} \right] \\ &+ \frac{2\eta}{r} \left( \frac{\partial v}{\partial r} - \frac{v}{r} \right) \end{aligned} \quad (15)$$

$$\frac{\partial}{\partial t}(\rho w) + \frac{1}{r} \frac{\partial}{\partial r}(r\rho uw) + \frac{\partial}{\partial x}(\rho w^2)$$

$$\begin{aligned}
&= -\frac{3}{5} \frac{\partial p}{\partial x} + \frac{\partial}{\partial x} \left[ 2\eta \frac{\partial w}{\partial x} - \frac{2}{3} \eta \nabla \cdot \vec{u} \right] \\
&- (jbar) j_r B_\theta + \frac{1}{r} \frac{\partial}{\partial r} \left[ \eta r \left( \frac{\partial u}{\partial x} + \frac{\partial w}{\partial r} \right) \right]
\end{aligned} \tag{16}$$

where  $jbar$  and  $\eta$  are defined as given below:

$$\begin{aligned}
jbar &= \frac{3}{5} \frac{B_{ref}^2}{\mu_o P_{ref}} \\
\eta &= \frac{\eta^*}{l_{ref} u_{ref} \rho_{ref}}
\end{aligned}$$

$$\begin{aligned}
&\frac{\partial e_T}{\partial t} + \frac{1}{r} \frac{\partial}{\partial r} \left( \left[ e_T + \frac{2}{3} p \right] u r \right) + \frac{\partial}{\partial x} \left( \left[ e_T + \frac{2}{3} p \right] w \right) \\
&= \frac{1}{r} \frac{\partial}{\partial r} \left( k r \frac{\partial T}{\partial r} \right) + \frac{\partial}{\partial x} \left( k \frac{\partial T}{\partial x} \right) \\
&\quad + \frac{10}{9} \eta \Phi + j_{sq} \left( \frac{j_r^2 + j_x^2}{\sigma} \right) \\
&+ (jubar) j_r w B_\theta - (jubar) j_x u B_\theta
\end{aligned} \tag{17}$$

In the energy equation, the thermal conductivity  $k$  is defined as

$$k = \frac{2}{3} \frac{k^*}{n_{ref} k_b u_{ref} l_{ref}};$$

and

$$\begin{aligned}
e_T &= n_T T + \sum_{i=1}^{N_d} \frac{f_i n_i T}{2} + \sum_{i=1}^{N_d} \sum_{v=0}^{Vmax} n_{i,v} E_{i,v} \\
&+ \Delta \epsilon + \frac{10}{9} \frac{\rho (u^2 + v^2 + w^2)}{2}
\end{aligned} \tag{18}$$

here,

$$\begin{aligned}
f_i &= \frac{2}{3} \frac{f_i^* l_{ref}}{P_{ref} u_{ref}} \\
E_{i,v} &= \frac{2}{3} \frac{E_{i,v}^* l_{ref}}{P_{ref} u_{ref}} \\
\epsilon &= \frac{2}{3} \frac{\Delta \epsilon^* l_{ref}}{P_{ref} u_{ref}}
\end{aligned}$$

$j_{sq}$  is defined as

$$j_{sq} = \frac{2}{3} \left( \frac{B_{ref}}{\mu_o l_{ref}} \right)^2 \left( \frac{l_{ref}}{P_{ref} u_{ref}} \right)$$

and  $j_{ubar}$  is defined as

$$\frac{2}{3} \left( \frac{B_{ref}^2}{\mu_o P_{ref}} \right)$$

Non-dimensional form of the continuity equation for monatomic species is

$$\begin{aligned} \frac{\partial n_m}{\partial t} + \frac{1}{r} \frac{\partial}{\partial r} (u n_m r) + \frac{\partial}{\partial x} (n_m w) + \frac{1}{r} \frac{\partial}{\partial r} \left( -r n_m \mu_m \bar{E}_r - \frac{r D_m}{kT} \frac{\partial}{\partial r} (n_m kT) \right) \\ + \frac{\partial}{\partial x} \left( -n_m \mu_m \bar{E}_x - \frac{D_m}{kT} \frac{\partial}{\partial x} (n_m kT) \right) = \bar{n}_m \end{aligned} \quad (19)$$

and the diatomic species is

$$\begin{aligned} \frac{\partial n_{i,v}}{\partial t} + \frac{1}{r} \frac{\partial}{\partial r} (u n_{i,v} r) + \frac{\partial}{\partial x} (n_{i,v} w) + \frac{1}{r} \frac{\partial}{\partial r} \left( -r n_{i,v} \mu_{i,v} \bar{E}_r - \frac{r D_{i,v}}{kT} \frac{\partial}{\partial r} (n_{i,v} kT) \right) \\ + \frac{\partial}{\partial x} \left( -n_{i,v} \mu_{i,v} \bar{E}_x - \frac{D_{i,v}}{kT} \frac{\partial}{\partial x} (n_{i,v} kT) \right) = \bar{V} T_{i,v} + \bar{V} V_{i,v} + S \bar{R} D_{i,v} + \bar{n}_{i,v} \end{aligned} \quad (20)$$

In the monatomic and diatomic species, the  $\bar{E}_r$  and  $\bar{E}_x$  are defined as

$$E_r = \frac{B_{ref} j_r}{\mu_o l_{ref} u_{ref} \sigma}$$

$$E_x = \frac{B_{ref} j_x}{\mu_o l_{ref} u_{ref} \sigma}$$

$\bar{n}_{i,v}$  and  $\bar{n}_m$  represent the non-dimensional net rate of production of the  $i^{th}$  species in the  $v^{th}$  vibrational state and the  $m^{th}$  monatomic species, respectively. The forward and backward rates describing these reactions are suitably redefined so that the nondimensionalising multiplying factors are "absorbed" into the expressions describing

the rates.

## 6.4 Magnetic Transport Equation

Maxwell's equations are used to describe the B-field distribution established due to current flow through the plasma. The Ohmic heating term in the energy equation and the body force terms in the momentum equations are computed from the the B-field distribution. A single equation for magnetic transport can be obtained from Maxwell's equations [Ref. 36] and Ohm's law as follows:

$$\nabla \times \vec{E} = -\frac{\partial \vec{B}}{\partial t}$$

$$\nabla \times \vec{B} = \mu_o \vec{j}$$

$$\nabla \cdot \vec{B} = 0$$

In addition to the above set of equations, a relationship between  $\vec{j}$  and  $\vec{E}$  given by Ohm's law

$$\vec{j} = \sigma [\vec{E} + \vec{u} \times \vec{B}]$$

is used to obtain the magnetic transport equation.

Elimination of  $\vec{E}$  and  $\vec{j}$  from these equations gives the magnetic transport equation in terms of  $\vec{B}$  and  $\sigma$  as:

$$\nabla \times (\nabla \times \vec{B}) - \frac{\nabla \sigma}{\sigma} \times (\nabla \times \vec{B}) - \mu_o \sigma (\nabla \times (\vec{u} \times \vec{B})) = 0 \quad (21)$$

where  $\partial \vec{B} / \partial t$  term has been neglected.

The inclusion of the  $\mu_o \sigma \left( \frac{\partial \vec{B}}{\partial t} \right)$  would involve resolution of extremely small time-scale due to the presence of the  $1/c$  term in the unsteady magnetic transport equation. This

would make the scheme unduly computation intensive and hence render it unattractive. This sort of computation is also unnecessary as a steady-state solution is desired. The assumption that the magnetic field relaxes to its new distribution instantaneously in each time step allows the exclusion of the time-derivative in the magnetic transport equation.

Using the vector identity

$$\nabla \times (\nabla \times \vec{B}) = -\nabla^2 \vec{B} + \nabla (\nabla \cdot \vec{B}) \quad (22)$$

and that  $\nabla \cdot \vec{B} = 0$ , equation (21) can be written as

$$-\nabla^2 \vec{B} - \frac{\nabla \sigma}{\sigma} \times (\nabla \times \vec{B}) - \mu_o \sigma (\nabla \times (\vec{u} \times \vec{B})) = 0 \quad (23)$$

The cross products in the above equations are expanded assuming that the magnetic field has only one component in the azimuthal direction, i.e.  $\vec{B} = -\hat{e}_\theta B_\theta$ .

The magnetic transport equation written in strong conservative form is as follows:

$$\frac{1}{r} \frac{\partial}{\partial r} \left( \frac{r}{\sigma} \frac{\partial B_\theta}{\partial r} \right) + \frac{\partial}{\partial x} \left( \frac{1}{\sigma} \frac{\partial B_\theta}{\partial x} \right) + \frac{B_\theta}{r} \frac{\partial}{\partial r} \left( \frac{1}{\sigma} \right) + \mu_o \frac{\partial}{\partial x} (w B_\theta) - \mu_o \frac{\partial}{\partial r} (u B_\theta) = 0 \quad (24)$$

Written in non-dimensional form

$$\frac{1}{r} \frac{\partial}{\partial r} \left( \frac{r}{\sigma} \frac{\partial B_\theta}{\partial r} \right) + \frac{\partial}{\partial x} \left( \frac{1}{\sigma} \frac{\partial B_\theta}{\partial x} \right) + \frac{B_\theta}{r} \frac{\partial}{\partial r} \left( \frac{1}{\sigma} \right) + \alpha \frac{\partial}{\partial x} (w B_\theta) - \alpha \frac{\partial}{\partial r} (u B_\theta) = 0 \quad (25)$$

where  $\alpha$  is defined as  $\mu_o u_{ref} l_{ref}$ . In terms of the classical magnetic Reynold's number,  $\alpha = R_m / \sigma$ . Since the magnetic Reynold's number in the problems studied in the present work are small, the  $\vec{v} \times \vec{B}$  terms are neglected and the above equation is written as

$$\frac{1}{r} \frac{\partial}{\partial r} \left( \frac{r}{\sigma} \frac{\partial B_\theta}{\partial r} \right) + \frac{\partial}{\partial x} \left( \frac{1}{\sigma} \frac{\partial B_\theta}{\partial x} \right) + \frac{B_\theta}{r} \frac{\partial}{\partial r} \left( \frac{1}{\sigma} \right) = 0 \quad (26)$$

The above form of the magnetic transport equation is used in the computation of the  $B_\theta$  in the present study.

## 6.5 Transport Properties

The governing equations discussed above include transport coefficients, namely, the coefficients of viscosity, thermal conductivity and the species diffusivities. In addition, the magnetic transport equation involves  $\sigma$  (electrical conductivity). These transport properties are evaluated using mean-free-path theory, wherein macroscopic quantities are calculated from kinetic theory [Ref. 37]. The high number density in the plasmas under consideration ensures that microscopic processes are collision dominated. This justifies the use of the mean-free-path theory. The transport properties based on the mean-free-path theory depend on average cross-sections, number densities of the species, and temperature. Since these quantities have a spatial dependence, the properties also vary spatially. The electrical resistivity is calculated as the sum of an electron-neutral component and a Spitzer-Harm Coulomb component. In the present work, we use a conductivity “floor” in order to avoid instabilities associated with the calculation of the B-field. In the colder regions of the plasma flow, the electrical conductivity predicted by mean-free-path theory is plausibly less than the real electrical conductivity. The low conductivity in these regions makes the elliptical magnetic transport equation lose its highest order derivative and hence, diagonal dominance. In practice, this conductivity floor is not an adjustable parameter. Rather, it has a fixed value based on the total power, which is normally maintained during an experimental measurement. The value of

the conductivity floor required to attain a specified power level is higher than that required for stability.

The drawback with the use of properties computed from mean-free-path theory is the reliance on average values of collision frequencies. These collision frequencies are in turn averaged over particle velocities. This averaging leads to results being accurate only to a factor of two or three [Ref. 37]. Computation of transport properties based on the EEDF gives more realistic estimates in non-equilibrium plasma flows.

## 6.6 Initial Conditions

The governing equations described in the previous sections are mixed hyperbolic-parabolic in character and it is important to specify appropriate initial conditions. The initial conditions for each of the variables are dependent on the problem at hand. These initial conditions will be further discussed with each case study. No initial distribution is required for the magnetic transport equation as it is elliptic in nature. However, the presence of the electrical conductivity in the magnetic transport equation indirectly demands an appropriate initial guess for the number densities and temperatures for stability.

## 6.7 Boundary Conditions

Solution of the governing equations described in the previous sections require the specification of appropriate boundary conditions for each of the dependent variable. The



boundary conditions are problem specific and will be discussed in detail in Chapter 8. However, the universally applicable boundary conditions are no-slip conditions for velocities and implicit extrapolation of number densities on solid surfaces. The magnetic transport equation also requires the specification of boundary conditions, which again will be discussed in Chapter 8.

The complete set of governing equations, and boundary and initial conditions constitute a model describing a particular phenomena or system. The solution of these equations yields variations of the quantities of interest describing the system. The complex form of the equations describing reacting plasma flows precludes analytical solution, leaving one with no recourse but to use numerical methods to obtain solutions. Chapter 7 describes the numerical technique employed in this work and its extension to the solution of reacting flows.



## 7. NUMERICAL METHOD

### 7.1 Introduction

Models of reacting flows describe the close interaction between several chemical and physical processes. This leads to numerous difficulties in the numerical solution of the governing equations. The governing equations describing such flows are time-dependent, non-linear and strongly coupled. Several methods have been devised to solve these equations. The *Block-Implicit method* or *Global-Implicit method*, and the *Fractional Step method* or *Timestep Splitting* are two major lines of approach. In the past, several attempts have been made to solve the compressible Navier-Stokes equations which essentially form a subset of the governing equations describing reacting flows. Among more popular methods of solving the compressible Navier-Stokes equations are MacCormack's Scheme [Ref. 38], Beam-Warming's Scheme [Ref. 39] and the Linearized Block Implicit Scheme of Briley and McDonald [Ref. 34]. In this work, the *Linearized Block Implicit Scheme* developed by Briley and McDonald for the solution of the unsteady, compressible Navier-Stokes equations is extended *to study reacting flows*.

### 7.2 Block Implicit Methods

The choice of a time marching scheme, namely implicit or explicit, depends on the time-scales involved in the problem. Explicit methods are best suited for problems when

the time-scales of interest are smaller than the minimum time-step dictated by the Courant condition. Simplicity in implementation is the single most important factor weighing in favor of explicit methods. However, if the time-scales of concern are greater than those required by the Courant condition ( $\Delta t \leq \Delta x/c$ ) [Ref. 40], and the equations are stiff, implicit methods have to be used. The reason is that stiffness precludes taking the maximum possible  $\Delta t$  allowed by the Courant condition. This makes the use of explicit schemes impractical as the computational time required for the solution of such equations immense. Stiffness, on occasions, tends to put such stringent requirements on the size of the time-step in explicit methods that roundoff errors become crucial. Implicit schemes have the virtue of circumventing these problems, at a price, albeit. This price, is the complexity in the implementation of the algorithm. Implicit schemes involve the simultaneous solution of a system of equations. This either means an iteration procedure at each time step must be employed or complicated matrices must be inverted which is time-intensive. Implicit methods are also slightly less accurate when compared to stable explicit methods.

Implicit methods aimed at solving a coupled set of equations are known as Block-Implicit methods. Block-Implicit methods were developed by Lindemuth and Killeen, McDonald and Briley, Beam and Warming, Briley and McDonald [Ref. 41] for solving compressible, time-dependent Euler and Navier-Stokes equations. The method essentially consists of a implicit scheme in which the solution is linearized by a Taylor expansion about the value at the previous time level. This produces a set of coupled linear difference equations which are valid for a given time step. This procedure will be described in detail next.

A non-linear set of coupled partial differential equations can be written as [Ref. 41]:

$$\frac{d}{dt}\mathbf{y}(\mathbf{x}, t) = G(\mathbf{y}, \nabla : \mathbf{y}, \nabla \cdot \nabla : \mathbf{y}, \mathbf{x}, t) \quad (1)$$

where,  $\mathbf{y}$  is a vector consisting of all the dependent variables and  $\mathbf{x}$  is a vector denoting the spatial coordinate. Each element of the vector  $\mathbf{y}$  is also time-dependent. The block-implicit method treats each of the dependent variables using fully implicit finite-difference approximations. The right hand side of equation ( 1) is evaluated using quantities at the advanced time level. The equation ( 1) in finite-difference form is written as:

$$\frac{\mathbf{y}^{n+1} - \mathbf{y}^n}{\Delta t} = \mathbf{G}^{n+1}$$

The arguments of  $\mathbf{y}$  and  $\mathbf{G}$  are suppressed in the above finite-difference equation for clarity. The above equation can also be written in the following approximate form:

$$\mathbf{y}^{n+1} \approx \mathbf{y}^n + \Delta t \mathbf{G}^{n+1} \quad (2)$$

The difficulty with the implicit treatment of the right hand side of equation ( 2) is that the new values of  $\mathbf{G}$  depends on the values of  $\mathbf{y}$  at the time level  $n + 1$  which are unknown. Equation ( 2) could be solved either iteratively at each time step or *linearized locally about the solution at the previous time step and thus solved without iteration as done in the linearized block implicit schemes*. In principle, the solution of nonlinear difference equations obtained iteratively is attractive as it obliterates errors occurring due to the linearization process. However, iterative solution of nonlinear difference equations can be very time consuming. Also, the convergence of the iteration is greatly dependent on the initial conditions prescribed. Hence from the point of view of stability and computational time, the later approach is advantageous.

The linearization of the nonlinear terms on the RHS of equation ( 2) is accomplished by assuming that the changes in  $\mathbf{y}$  are small. If the changes in  $\mathbf{y}$  are small then it may be assumed that the corresponding changes in  $\mathbf{G}$  are small too. This assumption permits one to expand  $\mathbf{G}^{n+1}$  in a Taylor expansion retaining only the first order terms in  $\Delta t$ . Thus yielding the form,

$$\mathbf{G}^{n+1} = \mathbf{G}^n + \Delta \mathbf{y} \frac{\partial \mathbf{G}^n}{\partial \mathbf{y}}$$

The linearization procedure is illustrated in a lucid manner by applying the above technique to the one-dimensional continuity equation, which is of the form,

$$\rho_t + F_x = 0 \quad (3)$$

where  $F$  is  $\rho u$ . Linearizing the above equation at time level  $n + 1/2$  (Crank-Nicolson differencing) and at a spatial location  $j$

$$\frac{\rho_j^{n+1} - \rho_j^n}{\Delta t} + \left( \frac{\partial F}{\partial x} \right)_j^{n+\frac{1}{2}} = 0 \quad (4)$$

The subscript  $j$  denotes the spatial location of discretization.  $\Delta t = t^{n+1} - t^n$ . The changes in the dependent variables are assumed to be small in the time interval  $\Delta t$ . The term  $(\partial F / \partial x)_j^{n+\frac{1}{2}}$  is expanded as a follows:

$$\left( \frac{\partial F}{\partial x} \right)_j^{n+\frac{1}{2}} = \left( \frac{\partial F}{\partial x} \right)_j^n + \frac{1}{2} \Delta t \left[ \frac{\partial}{\partial t} \left( \frac{\partial F}{\partial x} \right) \right]_j^n + O(\Delta t)^2 \quad (5)$$

The term  $\partial / \partial t (\partial F / \partial x)$  in the previous equation can be written as,

$$\frac{\partial}{\partial t} \left( \frac{\partial F}{\partial x} \right) = \frac{\partial}{\partial x} \left( \frac{\partial F}{\partial t} \right) = \frac{\partial}{\partial x} \left( \frac{\partial F}{\partial \rho} \frac{\partial \rho}{\partial t} + \frac{\partial F}{\partial u} \frac{\partial u}{\partial t} \right) = \frac{\partial}{\partial x} \left( u \frac{\partial \rho}{\partial t} + \rho \frac{\partial u}{\partial t} \right) \quad (6)$$

The equations ( 4)-( 6) can be combined to give the following equation;

$$\frac{\rho_j^{n+1} - \rho_j^n}{\Delta t} + \frac{u_{j+1}^n (\rho_{j+1}^{n+1} - \rho_{j+1}^n) - u_{j-1}^n (\rho_{j-1}^{n+1} - \rho_{j-1}^n)}{4\Delta x} +$$

$$\frac{\rho_{j+1}^n (u_{j+1}^{n+1} - u_{j+1}^n) - \rho_{j-1}^n (u_{j-1}^{n+1} - u_{j-1}^n)}{4\Delta x} = \frac{(\rho u)_{j+1}^n - (\rho u)_{j-1}^n}{2\Delta x} \quad (7)$$

In equation ( 7) central spatial differencing is used. The scheme is formally first order in time, the truncation error being  $O [\Delta t, (\Delta x)^2]$ . At steady-state the accuracy of the above scheme is  $O [(\Delta x)^2]$ . Equation ( 7) is unconditionally stable. It can be seen that equation ( 7) is linear in the quantity  $(\rho^{n+1} - \rho^n)$  and all other quantities are known as they are evaluated at the time instant  $n$ .

In a system of coupled difference equations, each one of the equations is finite differenced in a manner akin to that illustrated above. In each of these equations, fully-implicit finite-differencing gives rise to terms such as,  $(\phi_{1,j}^{n+1} - \phi_{1,j}^n)$ ,  $(\phi_{2,j}^{n+1} - \phi_{2,j}^n)$ ,  $(\phi_{3,j}^{n+1} - \phi_{3,j}^n)$ ,  $\dots$ ,  $(\phi_{q,j}^{n+1} - \phi_{q,j}^n)$ ,  $(\phi_{1,j-1}^{n+1} - \phi_{1,j-1}^n)$ ,  $(\phi_{2,j-1}^{n+1} - \phi_{2,j-1}^n)$ ,  $(\phi_{3,j-1}^{n+1} - \phi_{3,j-1}^n)$ ,  $\dots$ ,  $(\phi_{q,j-1}^{n+1} - \phi_{q,j-1}^n)$ ,  $(\phi_{1,j+1}^{n+1} - \phi_{1,j+1}^n)$ ,  $(\phi_{2,j+1}^{n+1} - \phi_{2,j+1}^n)$ ,  $(\phi_{3,j+1}^{n+1} - \phi_{3,j+1}^n)$ ,  $\dots$ ,  $\dots$ ,  $(\phi_{q,j+1}^{n+1} - \phi_{q,j+1}^n)$ , etc. and terms evaluated at the time instant  $n$ . It is assumed that the vector  $\rho$  contains  $q$  dependent variables. Terms such  $\phi_{1,j} \dots \phi_{q,j}$  represent the various dependent variables constituting the vector  $\rho$  at the spatial location  $j$ . The quantities evaluated at time instant  $n$  are carried over to the right hand side of the individual equations and constitute the “source” terms. In other words, the fully-implicit finite-differencing of the  $q$  governing equations at the spatial location  $j$  following the Briley-McDonald method would yield a set of linear algebraic equations as shown below

$$b_{11}\Delta\phi_{1,j-1} + \dots + b_{1q}\Delta\phi_{q,j-1} + d_{11}\Delta\phi_{1,j} + \dots + d_{1q}\Delta\phi_{q,j} +$$

$$a_{11}\Delta\phi_{1,j+1} + \dots + a_{1q}\Delta\phi_{q,j+1} = s_{1,j}$$

$$b_{21}\Delta\phi_{1,j-1} + \dots + b_{2q}\Delta\phi_{q,j-1} + d_{21}\Delta\phi_{1,j} + \dots + d_{2q}\Delta\phi_{q,j} +$$

$$a_{21}\Delta\phi_{1,j+1} + \dots + a_{2q}\Delta\phi_{q,j+1} = s_{2,j}$$

$\vdots$

$$b_{q1}\Delta\phi_{1,j-1} + \cdots + b_{qq}\Delta\phi_{q,j-1} + d_{q1}\Delta\phi_{1,j} + \cdots + d_{qq}\Delta\phi_{q,j} +$$

$$a_{q1}\Delta\phi_{1,j+1} + \cdots + a_{qq}\Delta\phi_{q,j+1} = s_{q,j}$$

The quantities  $(\phi_{1,j}^{n+1} - \phi_{1,j}^n)$  etc. at each spatial location  $j, j+1, j-1$ , etc. are written as  $\Delta\phi_{1,j}, \Delta\phi_{1,j-1}, \Delta\phi_{1,j+1}$ , etc. This system of equations can be written in a compact form at each spatial grid point  $j$  as,

$$B_j^n \psi_{j-1}^* + D_j^n \psi_j^* + A_j^n \psi_{j+1}^* = S_j^n \quad (8)$$

where,  $\psi_j^*$  represents a vector comprising the incremental changes in the dependent quantities at successive time steps, at the spatial location  $j$ , i.e.,

$$\psi_j^* = [(\phi_{1,j}^{n+1} - \phi_{1,j}^n), (\phi_{2,j}^{n+1} - \phi_{2,j}^n) + \cdots + (\phi_{q,j}^{n+1} - \phi_{q,j}^n)]^T$$

$B_j^n, D_j^n, A_j^n$ , are square matrices each containing terms evaluated at the known time instant  $n$  at the spatial location  $j$ .  $S_j^n$ , represents the vector comprising of the source terms in each of the  $q$  equations at the spatial location  $j$ . The forms of  $B_j^n, D_j^n, A_j^n$  and  $S_j^n$  are given below.

$$B_j = \begin{bmatrix} b_{1,1,j} & b_{1,2,j} & \cdots & b_{1,q,j} \\ b_{2,1,j} & b_{2,2,j} & \cdots & \vdots \\ \ddots & \ddots & \ddots & \ddots \\ b_{q,1,j} & b_{q,2,j} & \cdots & b_{q,q,j} \end{bmatrix}$$

$$D_j = \begin{bmatrix} d_{1,1,j} & d_{1,2,j} & \cdots & b_{1,q,j} \\ d_{2,1,j} & d_{2,2,j} & \cdots & \vdots \\ \ddots & \ddots & \ddots & \ddots \\ d_{q,1,j} & d_{q,2,j} & \cdots & d_{q,q,j} \end{bmatrix}$$



$$A_j = \begin{bmatrix} a_{1,1,j} & a_{1,2,j} & \cdots & a_{1,q,j} \\ a_{2,1,j} & a_{2,2,j} & \cdots & \vdots \\ \ddots & \ddots & \ddots & \ddots \\ a_{q,1,j} & a_{q,2,j} & \cdots & a_{q,q,j} \end{bmatrix}$$

$$S_j^n = \begin{bmatrix} s_{1,j} \\ s_{2,j} \\ s_{3,j} \\ \vdots \\ s_{q-1,j} \\ s_{q,j} \end{bmatrix}$$

It is computationally advantageous to solve the equations ( 8) in terms of these incremental changes (i.e.  $\Delta\phi_{1,j}$ ,  $\Delta\phi_{1,j-1}$ ,  $\Delta\phi_{1,j+1}$ ), etc. rather than the dependent variable itself at the next time instant (i.e.  $\phi^{n+1}$ ), not only because it simplifies the difference equations but also reduces round-off errors. If the number of dependent variables is  $q$ , then the size of each of the matrices,  $B_j^n$ ,  $\mathcal{D}_j^n$ ,  $\mathcal{A}_j^n$ , is  $q \times q$ .

When equation ( 8) is written out for all the points (in one direction) it yields a system of equations which can be cast in a matrix-vector form. This can be done by an appropriate treatment of the boundary points using the boundary conditions. This is described next.

Equation ( 8), when written out explicitly at  $j = 1$ , gives rise to terms such as

$(\phi_{1,0}^{n+1} - \phi_{1,0}^n)$ ,  $(\phi_{2,0}^{n+1} - \phi_{2,0}^n)$ ,  $(\phi_{3,0}^{n+1} - \phi_{3,0}^n)$ ,  $\cdots$ ,  $(\phi_{q,0}^{n+1} - \phi_{q,0}^n)$ . These quantities are expressed in terms of  $(\phi_{1,1}^{n+1} - \phi_{1,1}^n)$ ,  $(\phi_{2,1}^{n+1} - \phi_{2,1}^n)$ ,  $(\phi_{3,1}^{n+1} - \phi_{3,1}^n)$ ,  $\cdots$ ,  $(\phi_{q,1}^{n+1} - \phi_{q,1}^n)$  and  $(\phi_{1,2}^{n+1} - \phi_{1,2}^n)$ ,  $(\phi_{2,2}^{n+1} - \phi_{2,2}^n)$ ,  $(\phi_{3,2}^{n+1} - \phi_{3,2}^n)$ ,  $\cdots$ ,  $(\phi_{q,2}^{n+1} - \phi_{q,2}^n)$  using the boundary conditions.

Similarly, equation ( 8), when written out explicitly at  $j = N$ , gives rise to terms such

as,  $(\phi_{1,N+1}^{n+1} - \phi_{1,N+1}^n)$ ,  $(\phi_{2,N+1}^{n+1} - \phi_{2,N+1}^n)$ ,  $(\phi_{3,N+1}^{n+1} - \phi_{3,N+1}^n)$ ,  $\cdots$ ,  $(\phi_{q,N+1}^{n+1} - \phi_{q,N+1}^n)$  which can be expressed in terms of  $(\phi_{1,N}^{n+1} - \phi_{1,N}^n)$ ,  $(\phi_{2,N}^{n+1} - \phi_{2,N}^n)$ ,  $(\phi_{3,N}^{n+1} - \phi_{3,N}^n)$ ,  $\cdots$ ,

$$\left(\phi_{q,N}^{n+1} - \phi_{q,N}^n\right) \text{ and } \left(\phi_{1,N-1}^{n+1} - \phi_{1,N-1}^n\right), \left(\phi_{2,N-1}^{n+1} - \phi_{2,N-1}^n\right), \left(\phi_{3,N-1}^{n+1} - \phi_{3,N-1}^n\right), \dots, \\ \left(\phi_{q,N-1}^{n+1} - \phi_{q,N-1}^n\right).$$

This enables the elimination of  $B_1$ , and  $A_N$  from the system of equations. Thus, after elimination of the boundary conditions as described above, equation ( 8) at points  $j = 1$  and  $j = N$ , are;

$$\mathcal{D}_1^n \psi_1^* + \mathcal{A}_1^n \psi_2^* = \mathcal{S}_1^n$$

$$B_N^n \psi_{N-1}^* + \mathcal{D}_N^n \psi_N^* = \mathcal{S}_N^n$$

This system given by equations ( 8) can now be written in a matrix-vector form as

$$\mathcal{C}\Psi = \mathcal{S} \quad (9)$$

where,

$$\mathcal{C} = \begin{bmatrix} \mathcal{D}_1 & \mathcal{A}_1 & 0 & \cdots & 0 \\ B_2 & \mathcal{D}_2 & \mathcal{A}_2 & & \vdots \\ 0 & \ddots & \ddots & \ddots & 0 \\ \vdots & & B_{N-1} & \mathcal{D}_{N-1} & \mathcal{A}_{N-1} \\ 0 & \cdots & 0 & B_N & \mathcal{D}_N \end{bmatrix}, \quad \Psi = \begin{bmatrix} \psi_1^* \\ \psi_2^* \\ \psi_3^* \\ \vdots \\ \psi_{N-1}^* \\ \psi_N^* \end{bmatrix}, \quad \mathcal{S} = \begin{bmatrix} \mathcal{S}_1^n \\ \mathcal{S}_2^n \\ \mathcal{S}_3^n \\ \vdots \\ \mathcal{S}_{N-1}^n \\ \mathcal{S}_N^n \end{bmatrix}$$

This block-tridiagonal system can be solved very efficiently using methods discussed in [Ref. 42]. A detailed treatment of the linearized block implicit scheme can be found in [Ref. 34].

### 7.3 Alternate-Direction-Implicit (ADI) Technique

If the number of grid points in one direction is  $N_x$ , and the number of coupled equations to be solved at each spatial location is  $q$ , then the size of the block-tridiagonal

matrix,  $C$  obtained by applying the LBI scheme at each spatial point in the computational domain, is  $qN_x \times qN_x$ . The nature of the block-tridiagonal matrix is such that the overall computational matrix is very sparse. The blocks on the diagonal, and adjacent to the diagonal of  $C$  are  $q \times q$  in size. Direct inversion of these matrices is computationally very time consuming. In case of multidimensional problems, wherein, one has  $N_x$  grid points in one dimension, (say  $r$ -direction in  $r - \theta - z$  system, or  $x$ -direction in  $x - y - z$  system, etc.)  $N_y$  grid points in the second dimension (say,  $z$ -direction in  $r - \theta - z$ ,  $y$ -direction in  $x - y - z$  direction etc.) the size of the computational matrix,  $C$  is  $qN_xN_y \times qN_xN_y$ .

From the discussion in the previous paragraph, it is seen that multidimensional problems place very stringent demands on computational resources in terms of storage and solution of the block-tridiagonal matrices arising out of the block-implicit methods. This is due to the fact that large sparse matrices have to be solved completely over the entire computational domain at each time step.

Demands on computational resources can be greatly reduced if one resorts to the Alternating-Direction Implicit or ADI method for multidimensional problems. This method, first derived by Peaceman and Rachford [Ref. 43], is used in the numerical solution of multidimensional PDEs. *The basis of this method is to make the equations implicit along only one direction at a time.* This approximation, leads to the equations reducing to three-point relations along one direction. These equations can then be cast in a matrix-vector form akin to equation ( 9). The block-tridiagonal form of the resulting equation can be solved efficiently. The intermediate solution obtained along one direction is then used in the solution of the system of equations in the other direction. An attractive feature of this scheme is that it is unconditionally stable. It is

only conditionally unstable in 3-D when periodic boundary conditions are used. This procedure can be extended to three dimensional problems also. A detailed explanation of the ADI procedure is given in [Ref. 44]. In this work, following Briley and McDonald [Ref. 34] we adopt the Douglas-Gunn ADI scheme for the solution of the multidimensional system of equations.

The application of the Douglas-Gunn ADI scheme, to the system of equations discussed in Chapter 6 is demonstrated next using a simple set of coupled equations in 2-D.

Consider a system of equation in 2-D written as;

$$\frac{\partial \phi}{\partial t} = D_x(\phi) + D_y(\phi)$$

Here,  $D_x(\phi), D_y(\phi)$  represent spatial derivative operators. Applying the Crank-Nicholson differencing at time instant  $n + 1/2$ , yields, the following form:

$$\left(I - \frac{\Delta t}{2} D_x - \frac{\Delta t}{2} D_y\right) (\phi^{n+1} - \phi^n) = \Delta t (D_x + D_y) \phi^n \quad (10)$$

The LHS of the above equation can be approximately factorized as follows;

$$\left(I - \frac{\Delta t}{2} D_x - \frac{\Delta t}{2} D_y\right) (\phi^{n+1} - \phi^n) \approx \left(I - \frac{\Delta t}{2} D_x\right) \left(I - \frac{\Delta t}{2} D_y\right) (\phi^{n+1} - \phi^n)$$

Equation ( 10) can then be written as

$$\left(I - \frac{\Delta t}{2} D_x\right) \left(I - \frac{\Delta t}{2} D_y\right) (\phi^{n+1} - \phi^n) = \Delta t (D_x + D_y) \phi^n \quad (11)$$

The above equation can also be written as

$$\left(I - \frac{\Delta t}{2} D_x\right) \phi^* = R^n \quad (12)$$

where

$$\left(I - \frac{\Delta t}{2} D_y\right) (\phi^{n+1} - \phi^n) = \phi^* \quad (13)$$

and,

$$R^n = \Delta t (D_x + D_y) \phi^n \quad (14)$$

Equation ( 12) and ( 14) are first solved to yield  $\phi^*$ . Equation ( 13) is then solved to obtain the  $(\phi^{n+1} - \phi^n)$ .

This technique is called *Operator-Splitting*. It can be seen from the above treatment that the technique can be easily extended to 3-D problems. The method of operator-splitting has effectively reduced equation ( 10) to one that requires solution of another intermediate equation to obtain  $\phi^*$ , which is then used to yield  $(\phi^{n+1} - \phi^n)$ . As mentioned above, the two-step solution of equation ( 10) maintains the narrow-banded block-tridiagonal structure in each dimension (direction) and hence lends itself to be solved by efficient block-elimination methods. A virtue of this method of operator-splitting is that the intermediate solutions are consistent approximations to  $(\phi^{n+1} - \phi^n)$ . This facilitates the use of the physical boundary conditions applicable to  $(\phi^{n+1} - \phi^n)$  for the solution of the intermediate equations (i.e. equations containing  $\phi^*$ ) without a serious loss of accuracy. It is for this reason that the LBI scheme using the Douglas-Gunn ADI procedure is called “Consistently split Linearised Block Implicit method”. Briley and McDonald give a detailed analysis of the application of this method to multidimensions.

#### 7.4 Salient Features of the LBI Scheme

The LBI scheme exploits the favorable stability properties of implicit schemes and thus improves computational efficiency by allowing larger time steps to be used when

time marching unsteady, coupled equations as compared with explicit methods. This method is easily extendable to multidimensional problems. *The true import of this method, is its promise to lead to development of efficient, non-iterative solutions of coupled nonlinear multidimensional PDEs describing reacting flows.* The stability properties of this scheme allow time steps in the time marching scheme of unsteady coupled equations to be orders of magnitude larger than the maximum allowable time steps for conditionally stable methods as determined by the Courant-Friedrichs-Lewy (CFL) condition. This a great boon in the solution of stiff equations describing chemical kinetics in reacting flows. Briley et.al report [Ref. 34] that the computational cost per time step is only approximately twice that of most explicit methods for problems involving cold flows through 3-D rectangular ducts. However, it is highly dubious whether explicit methods can yield solutions to plasma flow problems at all.

## 7.5 Artificial Dissipation

Central differencing of the convective terms in the governing equations gives rise to numerical diffusion terms [Ref. 45]. Numerical diffusion, which can be a major source of error in finite-difference calculations has the same form and effect as physical diffusion [Ref. 41]. The effect of numerical diffusion is not only to bring about a damping of the solution (dissipation) but also to distort the phase relations between various waves (dispersion). These spurious oscillations often cause the solution to become unstable by making quantities like mass density and temperature go negative. Artificial dissipation of some form is necessary [Ref. 34, Ref. 41] in order to avoid these spurious

oscillations and maintain positivity. Artificial dissipation in some form is also necessary to provide overall stability to the algorithm when boundary conditions are treated inaccurately, when the mesh spacing is coarse or in the presence of discontinuities [Ref. 34]. Artificial dissipation in the form of a second derivative is added in the axial and radial direction to all the governing equations. The functional form of the dissipation terms used in this work is  $\epsilon_x \mathcal{D}_x^2 \phi + \epsilon_r \mathcal{D}_r^2 \phi$ , where  $\phi$  is  $\rho$  in the continuity equation,  $u, v, w$  in the radial, azimuthal and axial components of the momentum equations, respectively,  $T$  in the energy equation and  $n_{i,v}$  or  $n_m$  (as the case may be) in the species equations. The dissipation term is treated implicitly just as all other terms, and thus contributes to both the source terms on the right hand side as well as the elements of the block-tridiagonal on the left hand side. The dissipation model used in this work is different from that used by Briley. The coefficients  $\epsilon_x$  and  $\epsilon_r$  are chosen so as to ensure the positivity of all the dependent variables and minimize the effect of the term  $\epsilon_x \mathcal{D}_x^2 \phi + \epsilon_r \mathcal{D}_r^2 \phi$  in the overall solution. Unfortunately, the functional forms of  $\epsilon_x$  and  $\epsilon_r$  are dependent on the problem under consideration. These forms and their impact on the accuracy of the solution are described in greater in Chapter 8.

## 7.6 Grid Generation

The governing equations described in Chapter 6 describe the variables of interest in the physical domain. Physical domains of interest in this study have complicated geometries. In such situations it is necessary to transform the governing equations and the relevant boundary condition describing the flow in the physical domain to the

computational domain. This transformation from the physical domain to the computational domain requires the inclusion of the metrics of mapping in the differential equations. To facilitate the use of the reacting flow solver developed here at The Ohio State University to a wide variety of problems, the grid generation module is independent of the reacting flow solver. Since this work is primarily directed towards obtaining 2-D axi-symmetric solutions of reacting flows, the grid generation module currently in use, transforms a 2-D (more specifically, the  $r$  and  $z$  directions) physical domain of interest, into a rectangular computational domain. The grid generation module currently allows the usage of non-uniform grids in the radial direction only. Use of non-uniform grids is not greatly advantageous in the axial direction since no steep gradients are encountered, except in regions where the relatively cold gas traverses the arc. Additionally, use of uniform grids in the axial direction simplifies the transformed equations considerably and hence greatly reduces programming efforts. Non-uniform grids in the radial direction, however, allow a better resolution of phenomena occurring close to the electrodes. The grid generation routine transforms the physical domain into the computational domain and evaluates the transformation derivatives. These transformation derivatives are then read by the flow solver. Non-uniform transformation from the physical to the computational domain can be brought about by transformations similar to those described by Anderson et.al [Ref. 33]. It is important to point out that non-staggered grids are used in this study. In the present work, *uniform grids in both the axial and radial direction* are used to solve the transformed governing equations and boundary conditions. A general cylindrical coordinate system which is axi-symmetric is described by  $r$  and  $x$ . The radial coordinate at the boundaries



(i.e.  $r_i$  and  $r_o$ ) may vary with  $x$ . The coordinate transformations employed here are:

$$\xi = \frac{r - r_i}{r_o - r_i}$$

and

$$\zeta = x$$

and where,  $r_i(x)$  is the inner boundary,  $r_o(x)$  is the outer boundary and  $x$  is the axial coordinate. Thus, we are transforming from  $(r(x), x)$  to  $(\xi(\zeta), \zeta)$ . Under this transformation

$$\frac{\partial}{\partial r} = \xi_r \frac{\partial}{\partial \xi} \quad (15)$$

$$\frac{\partial}{\partial x} = \xi_x \frac{\partial}{\partial \xi} + \frac{\partial}{\partial \zeta} \quad (16)$$

$$\frac{\partial^2}{\partial r^2} = \xi_r^2 \frac{\partial^2}{\partial \xi^2} + \xi_{rr} \frac{\partial}{\partial \xi} \quad (17)$$

$$\frac{\partial^2}{\partial x^2} = \xi_x^2 \frac{\partial^2}{\partial \xi^2} + 2\xi_x \frac{\partial^2}{\partial \xi \partial \zeta} + \frac{\partial^2}{\partial \zeta^2} + \xi_{xx} \frac{\partial}{\partial \xi} \quad (18)$$

These transformations are used to transform the governing equations from the real physical domain to a rectangular computational domain (see. Figure 58).

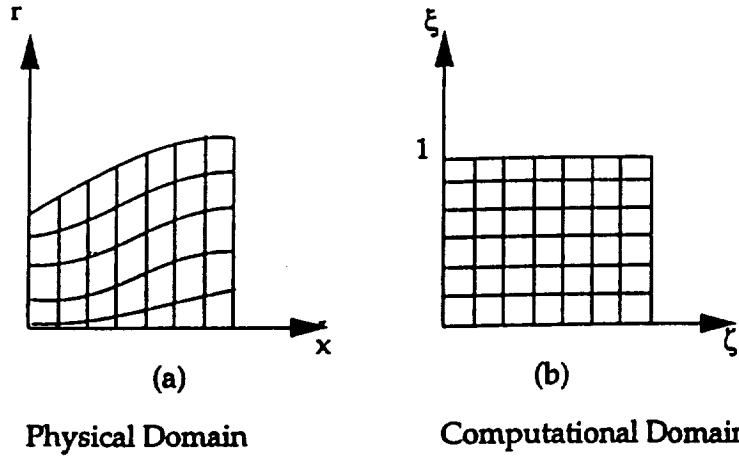


**Figure 58 Transformation from Physical Domain to Computational Domain**

### 7.7 Extension of the LBI Scheme to Reacting Flows

The transformed governing equations along with the boundary conditions are time-discretized using second order accurate Crank-Nicolson differencing. The linearization of the nonlinear terms is done according to the procedure described in section 7.2 on Block Implicit Methods. All terms containing the dependent variables are discretized implicitly, including those in the boundary conditions. Since no diatomic gases are involved in the present study, the diatomic species equations need not be solved. Assuming quasi-neutrality, a single equation describing the time-evolution of electrons is solved. The concentration of Argon atoms is determined from the relationship between mass density and number densities of electrons, argon ions and argon atoms and not a species continuity equation. This is done to make the equations linearly independent. The equation describing the time-evolution of electrons is similar

to the monatomic species equation. The net production term,  $\dot{n}_m$  is a function of rate-constants and number densities. The rate constants are functions of temperature. However, this term is discretized by treating the number densities implicitly and the rates explicitly i.e. they are evaluated using temperature values from the previous time step. This is primarily due to the fact that the expressions for rate constants are experimentally obtained values usually fit to a curve. More importantly, the experimentally available information on rate constants do not cover the entire temperature range which one is likely to observe in different problems. Implicit treatment of the rate constants in these governing equations would preclude the possibility of changing the rate models with ease. Quasi 1-D simulations describing nozzle flows with high degree of vibrational non-equilibrium [Ref. 32] has shown that explicit treatment of rate constants do not adversely affect the overall stability of the numerical scheme. Furthermore, since we are interested in steady-state solutions, errors arising out of explicit treatment of the rates in the transient solution are not a matter of great concern.

Since this work is aimed at examining 2-D axisymmetric flows, the Douglas-Gunn ADI scheme is used to solve the transformed governing equations. The transformed operators are consistently “split” as explained in section 7.3, and then solved in each spatial direction, namely,  $x$ – direction and  $r$ – direction. The spatial derivatives of the dependent variables in the transformed equations in each coordinate direction are then discretized using second order accurate central differences. The boundary conditions are then used to eliminate the boundary points, thus reducing the system of linear algebraic equations to obtain a block-tridiagonal system of equations in each coordinate direction. Having obtained the block-tridiagonal matrices, the unsteady set of equations are time

marched. Computations can be begun with an initial guess, or from an intermediate solution that has been previously advanced to a certain time level. Properties are calculated at each time step based on the solutions from the previous time step. The magnetic transport equation is solved at each time-step during the time marching. This is necessary because the transient nature of temperature and number densities cause the electrical conductivity, and hence the magnetic induction to change. The magnetic transport equation is solved using an odd-even point Jacobi iterative scheme. Solution of this system of equations in each coordinate direction, yields quantities such as  $\phi_j^{n+1} - \phi_j^n$  where  $\phi_j$  denotes the vector of the dependent variables, at each grid point in the computational domain. This correction  $(\phi_j^{n+1} - \phi_j^n)$  when added to the quantity  $\phi_j^n$  yields the solution at the next time level  $n + 1$  (i.e.  $\phi_j^{n+1}$ ). The solution is thus advanced until steady-state is reached.

## 8. RESULTS FOR INTERNAL AND EXTERNAL PLASMA FLOWS

### 8.1 Introduction

The plasma arc welding torch can be operated in one of several modes - straight polarity, reverse polarity, or variable polarity. The discharge is initiated by applying a high frequency alternating voltage between the inner electrode (cathode) and the constricting nozzle (anode) so as to establish a pilot arc. The polarity of the pilot arc does not alternate. The nozzle is always held positive with respect to the electrode (by about 20 V). The main arc (transferred arc) is then struck between the workpiece and the cathode. The workpiece is always grounded and the inner electrode is biased positive or negative with respect to the workpiece. This bias voltage is usually around 30 V. When an arc is struck by applying an electric field between two electrodes, the positive ions and electrons in the arc column act as charge carriers. By virtue of their significantly lower mass, electrons acquire a greater velocity as compared with the ions in the interelectrode space. This fact is made use of in the various modes of operation of the Plasma Arc Welding (PAW) process. In the straight polarity mode, the central electrode acts as the cathode (held negative) and the workpiece acts as the anode. The flux of electrons impinging on the workpiece is much greater than the ion flux impinging

on the cathode. Hence, this mode of operation is used when the objective is to deliver a maximum amount of heat to the workpiece with minimal deterioration of the electrode. In the reverse polarity mode, the electrode is positive and the workpiece is negative. This subjects the workpiece to a cleaning process called “cathodic cleaning”, on account of the surface bombardment by heavy ions. This is of importance when the work-piece is Aluminium. In the variable polarity mode, the polarities of the workpiece and the central electrode are reversed at fixed time intervals. This method exploits the merits of both - the straight polarity and the reversed polarity modes of operation. Typically, it is operated in the straight polarity mode for about 19 milliseconds and the reverse polarity mode for 4 milliseconds.

A systematic study of the design and operating conditions of the torch and the plasma jet is required to obtain a better understanding of the operating characteristics of the torch. The results of such a study would establish plausible links between the skew phenomena, the torch design and operating conditions. This should provide a more rational basis for future designs with better performance. With these main objectives in mind the present study endeavors to study flow characteristics in these torches, and the external jets impinging on the work-piece.

## **8.2 Background**

A number of groups have attempted to model plasma jets occurring in welding applications and compare the results of their calculations with available experiments. The experimental results mostly comprise of temperature measurements in the plume of a free jet. The earliest attempts to model plumes of plasma torches [Ref. 46, Ref. 47, Ref. 48] required the specification of temperature and velocity profiles at the exit plane

of the nozzle as boundary conditions. Lee and Pfender [Ref. 48] studied the effects of two different temperature and velocity profiles at the nozzle exit on the external flow of a free jet. The profiles chosen were such that the overall mass and energy flow rates in the two cases were identical. In spite of this imposed overall mass and energy flow rates, the largest temperature difference computed in the external plume domain was 3000 K and the largest velocity difference was 300 m/s. These differences are equivalent to about a 30% variation in temperature and about 100% in velocity. Since these models did not include the arc region within the torch, the temperatures and velocities of the plasma at the exit plane of the torch could be obtained only by a gross specification of the mass and energy flow rate. Thus, to obtain realistic information about the flow characteristics in the plume, it is essential to correctly model the arc region in the interior of the torch. To overcome these deficiencies in these earlier models, Scott et.al [Ref. 49] attempted to model the torch as a single entity. The region behind the cathode, the arc region and the plasma plume region were all included in a single model. This model was a steady, 2-D model which included the swirl component of the flow and a  $K - \epsilon$  turbulence model. Further, the plasma and the ambient gas were both argon, so the effects of mixing and entrainment were not included. Westhoff et.al [Ref. 50] attempted a study similar to that of Scott et. al [Ref. 49]. However no additional physics was included in their model. Murphy and Kovitya [Ref. 51] have extended Scott et. al.'s model [Ref. 49] to include the effects of mixing of the plasma gas with an ambient gas. However, these models do not include the effect of shielding gases. They also do not include ionization reactions, and ionization fractions are computed from equilibrium (Saha) considerations. All the above mentioned models simulate free jets and are thus non-transferred arcs. It is indeed surprising that the above mentioned works are the

only models that attempt a numerical solution of the 2-D MHD equations describing plasma arcs. All solve steady flow equations and do not model transferred arcs. In contrast to these earlier works, the present work is the *first attempt to model transferred plasma arcs*. The governing equations described in Chapter 6 are solved to obtain the flow characteristics and species concentrations in a *transferred plasma arc*. The internal flow simulations are used to obtain all the flow variables at the exit plane of the torch. The external flow simulation is then used to model the plasma jet impinging on the work-piece by using the exit plane values computed from the internal flow. The flow is assumed to be laminar in the present work, although effects of turbulence can be included given a turbulence model. Effects of the shielding gas are included in the external flow simulation. The effects of ambient entrainment are not included, though the present formulation can be very easily modified to include this effect. Model validation in the present work is radically different from other earlier and existing investigations. Scott et.al. [Ref. 49] and Murphy et.al [Ref. 51] have compared the results of their simulations to temperature contours obtained experimentally from free jets. Using measured temperature as a measure of model reliability is questionable since the measurement techniques make inherent assumptions about the radiating state of the plasma (such as LTE). Fincke et.al [Ref. 52] discuss the results obtained by two methods - enthalpy probe and laser light scattering experiments. Murphy et.al. [Ref. 51] point out that the comparison reported by Scott et.al [Ref. 49] are suspect since they used emission spectroscopy to obtain experimental temperature profiles, a technique which relies on the gas being in LTE. On the other hand, the laser light scattering technique for temperature measurement used by Murphy et.al. requires a precise knowledge of the gas composition. To avoid these complications,



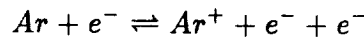
a simple and inexpensive diagnostic technique is used in the present work for model validation. A radial pressure profile is measured on a water-cooled copper plate while the plasma jet impinges on it. This measured radial pressure distribution is then compared with pressure profiles predicted by the present calculation.

### 8.3 Formulation

A 2-D axi-symmetric model is developed here and the calculations are carried out in two stages. The internal and external flows are described by the same set of governing equations as described in Chapter 6, except that the boundary conditions for the two are different. An internal flow simulation is first conducted in order to obtain the flow field, temperature and species concentration within the torch body for a given mass-flow rate and power. The calculated exit plane values of the flow variables are then used as boundary conditions for the external flow calculations of the plasma jet. The predicted radial pressure profile is then compared with experimentally measured pressure profiles at the surface of a water-cooled copper workpiece (see Chapter 4 [Ref. 53]). The internal flow simulations provide profiles of the flow variables at the exit plane of the torch. This enables investigation of the effects of torch geometry on the temperature and velocity fields at the exit plane of the torch, and allows us to explore their effects on the external jet.

## 8.4 Assumptions

The above paragraph outlines the broad framework adopted in the study of plasma flows in these torches. Arc welding involves highly complex phenomena. These include close coupling of several phenomena including electromagnetic forces, fluid flow and both molten and gaseous phases. From the practical standpoint, the development of thermal stresses and stress-induced deformation are of importance as they affect the properties of the weldment. To make the problem tractable however, some simplifying assumptions are made in addition to the general assumptions discussed earlier. Emphasis is placed here only on the plasma jet impinging on the workpiece. Phase-change at the surface is not taken into consideration. This work does not attempt to couple the modeling of the weld pool with the arc. The workpiece is considered a boundary of the fluid domain. Self-induced magnetic fields are considered. Buoyancy effects are neglected. Argon ( $Ar$ ) is the plasma gas as well as the shield gas. It is assumed that the gas comprises of  $Ar$ ,  $Ar^+$ , and  $e^-$  and hence the only reaction considered is:



The plasma is assumed to be quasi-neutral i.e. the effect of space-charges are neglected. Figure 59 shows the physical domain under consideration for the internal flow.

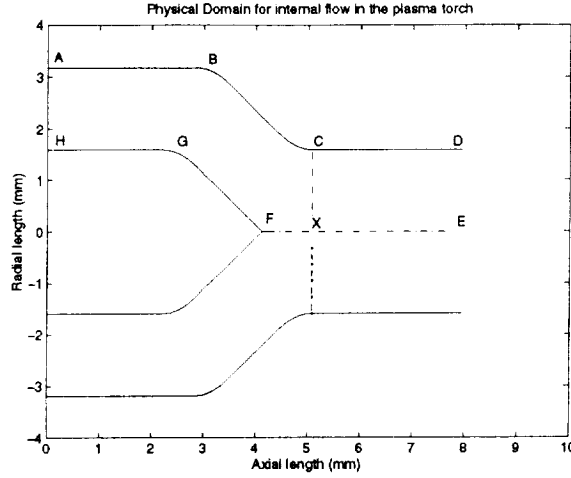


Figure 59 Geometry of the Plasma Torch for internal flow simulations

### 8.5 Internal Flow - Boundary Conditions

The non-dimensional form of the governing equations described in Chapter 6 are solved in conjunction with appropriate boundary and initial conditions to obtain the velocity, temperature, magnetic induction and species concentrations within the torch.

All the boundary conditions for the flow variables are identical to those discussed in relation to the arcjets [Ref. 54, Ref. 55] except at the anode wall. To simulate the cooling of the torch body, a convective boundary condition of the form

(non-dimensionalized)  $dT/dr|_{wall} = h_{eff}(T|_{wall} - T_{cool})$  is used.  $h$  was set to 175 and the  $T_{cool}$  was set 300 K. The solution was not found to be very sensitive to the values of  $h$  and  $T_{wall}$ . The mass density and the electron number density at the wall were determined by setting the first derivative of each of the quantities to zero. This prescription was found to be most stable numerically. The boundary conditions for the

electromagnetics differ from those discussed earlier for the arcjet. As shown in Figure 59 the nozzle does not have a diverging region. The electromagnetic computations commence from the axial location corresponding to the beginning of the straight section. At this axial location, the radial current density,  $j_r$ , is set to zero, which is tantamount to setting  $\partial B/\partial x = 0$ . A constant value of  $B_\theta$  depending on the operating current, is prescribed along the straight section of the nozzle. In other words  $B_\theta = \mu_o I/2\pi r_c$ , where  $r_c$  is the inside radius of the torch nozzle body.  $B_\theta = 0$  along the centerline and  $\partial B/\partial x = 0$  along the exit plane. These boundary conditions mimic a transferred arc well. The presence of the pilot arc is not included in the results presented here. The Neumann boundary conditions applied at the beginning of the electromagnetic calculations and at the exit plane, make the current lines parallel to the centerline and the prescription of a fixed value of  $B_\theta$  along the inside radius of the constricting nozzle prevents any current attachment on the walls.

The boundary conditions described above are summarized in tables 3 and 4

	ABCD (Anode)	DE (Exit Plane)	EF (Centerline)	FGH (Cathode)	HA (Inlet)
$\rho$	$\partial\rho/\partial r = 0$	from $P_{exit}$	$\partial\rho/\partial r = 0$	$\partial^2\rho/\partial r^2 = 0$	Equation of state
u	$= 0$	$\partial^2 u/\partial x^2 = 0$	$= 0$	$= 0$	u = 0
w	$= 0$	$\partial^2 w/\partial x^2 = 0$	$\partial w/\partial r = 0$	$= 0$	$\partial^2 w/\partial x^2 = 0$
T	$\partial T/\partial r =$ $h(T_{r=r_o} - T_{wall})$	$\partial^2 T/\partial x^2 = 0$	$\partial T/\partial r = 0$	$\partial^2 T/\partial r^2 = 0$	from $T_o$
$n_e$	$\partial^2 n_e/\partial r^2 = 0$	$\partial^2 n_e/\partial x^2 = 0$	$\partial n_e/\partial r = 0$	$\partial^2 n_e/\partial r^2 = 0$	$\partial^2 n_H/\partial x^2 = 0$

**Table 3 Boundary conditions for internal flow variables in a plasma torch**

	CD	DE	EF	CX
$B_\theta$	Prescribed	$j_r = 0$	$B_\theta = 0$	$j_r = 0$

**Table 4 Boundary conditions for electromagnetics**

## 8.6 External Flow - Boundary Conditions

The exit plane values of all the flow variables generated by the internal flow calculations are used as inflow boundary conditions for the external flow up to the radial location corresponding to the dimensions of the inner radius of the nozzle (along AB in Figure 60). BC in Figure 60 denotes the portion of the domain simulating the flowing shield gas. Shield gas flow is simulated by prescribing a profile for the axial and radial components of velocities in such a way that their integrated values over the cross-section yields the desired mass-flow rate used in experiments. The pressure is set equal to the atmospheric pressure in the region of the computational domain where the shield gases enter. Based on this value of pressure and a prescribed temperature (500 K) for the shield gas, a density can be computed. The integrated mass flow rate of the shield gas is thus set to the experimentally reported shield gas mass flow rate ( $\approx 25$  standard cubic feet/hour (SCFH)). A reasonable value for the temperature and density need to be prescribed for the shield gases. Our calculations indicate however that these profiles have a negligible influence on the final solution. Variations in shield gas flow rate also have minimal effect on the overall solution. It was seen that doubling the flow rate led to a change of less than 2% in the predicted pressure profile at the surface of the

work-piece. The edge of the torch body (denoted by CD in Figure 60) is maintained at a fixed temperature and atmospheric pressure. In these simulations the torch body was maintained at 500 K, although the final solution is not sensitive to this value of temperature. Symmetry boundary conditions are maintained along the centerline (AF in Figure 60) for all variables except the azimuthal and the radial components of velocity, i.e.,  $\partial\phi/\partial r|_{r=0} = 0$ . The radial and the swirl component of velocities are set to zero identically along the centerline.

At the plate surface (FE in Figure 60), no slip conditions are applied for all components of velocity. A convective boundary condition is used for the temperature in the following non-dimensional form, to simulate cooling of the work-piece at which pressure measurements are made:  $\partial T/\partial x|_{x=L} = h_{eff}(T_{x=L} - T_c)$ , where  $h_{eff} = h_o \exp(-r/r_o)^2$ ,  $T_c = 500$  K.  $h_o = 75$  and  $(r/r_o)^2$  is the normalized distance from the centerline along the plate surface. It was found that the algebraic form of the heat-transfer coefficient influences the radial pressure profile. The present form exhibited the best results in simulating the steep radial temperature gradient that is expected along the surface of the workpiece. In addition,  $\partial\rho/\partial x = 0$  and  $\partial n_e/\partial x = 0$  are the boundary conditions used for the mass density and number density of electrons at the work-piece. The radial location corresponding to the edge of the torch body is the outer boundary of the computational domain in the radial direction (DE in Figure 60).

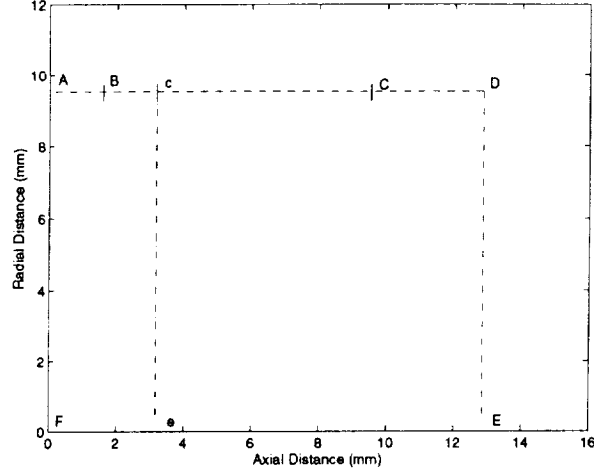


**Figure 60 Physical Domain for simulation of Plasma Jet issuing from the torch**

Implicit extrapolation in the radial direction is used along DE to describe all velocity components and species (i.e.  $\partial^2 \phi / \partial r^2|_{r=r_o} = 0$ ). Static pressure along this plane is set equal to the ambient atmospheric pressure. An insulated boundary condition is used to describe the temperature at the outer radial boundary, i.e.  $\partial T / \partial r = 0$ . Since the size of the computational domain chosen is big enough, such a boundary condition is unlikely to affect the solution. It was found that prescription of a constant temperature along the outer radial boundary (a posteriori) influenced the solution and therefore was not used in the present calculations. Implicit extrapolation in the radial direction is used to obtain the electron number density at this radial outflow boundary. The equation of state is used to determine the mass density in non-dimensional form ( $\rho = P_{atm} / T_{r=r_o} - n_e$ ).

The governing equation describing the  $B_\theta$  field is the same as in the internal flow.

However, in the interest of attaining high computational speeds, the magnetic transport equation is not solved over the entire domain. It has been observed experimentally that the spread of the jet is negligible. Hence the extent of the computational domain for the

electromagnetics is restricted to twice the extent of the nozzle radius (AceF denotes the region over which the magnetic transport equation is solved). A restricted domain describing the electromagnetics has the virtue of saving computing time. No current flow is assumed along the surface of the plate, which translates to  $\partial B/\partial x = 0$ .  $B_\theta = 0$  along the centerline by symmetry. Values of  $B_\theta$  obtained from the internal flow solutions are prescribed up to grid locations less than the nozzle radius (Along AB in Figure 60). Along the remaining radial grid points the enclosed current is assumed to be constant (i.e.  $B_\theta = \mu_o I/2\pi r$  along Bc in Figure 60). The constant value of enclosed current corresponding to the location 'c' is prescribed along 'ce' in Figure 60. Thus a constant value of  $B_\theta$  is maintained along 'ce'.

The boundary conditions described above are summarized in tables 5 and 6

	AD	DE (Outflow)	EF (Workpiece)	FA (Centerline)
$\rho$	Prescribed	$\partial^2 \rho / \partial r^2 = 0$	$\partial \rho / \partial r = 0$	$\partial \rho / \partial r = 0$
$u$	Prescribed	$\partial^2 u / \partial r^2 = 0$	$= 0$	$= 0$
$w$	Prescribed	$\partial^2 w / \partial r^2 = 0$	$= 0$	$\partial w / \partial r = 0$
$T$	Prescribed	$\partial T / \partial r = 0$	$\partial T / \partial x =$ $h(T_{r=r_o} - T_{plate})$	$\partial T / \partial r = 0$
$n_e$	Prescribed	$\partial^2 n_e / \partial^2 r = 0$	$\partial n_e / \partial x = 0$	$\partial n_e / \partial r = 0$

**Figure 5 Boundary conditions for external flow variables**

	AB	Bc	ce	eF	FA
$B_\theta$	Prescribed	$B_\theta = \mu_o / 2\pi r$	$B_\theta = \mu_o / 2\pi r_{r=r_c}$	$j_r = 0$	$B_\theta = 0$

**Table 6 Boundary conditions for electromagnetics**



## 8.7 Initial Conditions

Reasonable initial profiles need to be specified to begin the internal and external flow simulations. The axial velocity profile linearly increases from a small value at the inlet to a prescribed subsonic value of 1000 m/s. Pressure at the exit plane is set equal to one atmosphere and the pressure decreases linearly from the  $P_{ref}$  to this value. The temperature increases linearly from 1000 K to 10,000 K at the exit plane. These axial variations are then scaled in the radial direction to give a parabolic variation. The initial conditions for the external flow were not found to be very crucial for stable time-marching. Small velocities for the axial and radial velocities are prescribed throughout the domain ( $u \approx 20$  m/s,  $w \approx 20$  m/s). The static pressure within the domain was set at the ambient value. The temperature was kept at 10000 K throughout the domain. The electron number density was set at a small constant value all through the domain ( $n_e = 1e - 6 \times P_{ref}/k_b T_{ref}$ ). The density was evaluated from the temperature and pressure using the equation of state in non-dimensional form ( $\rho = P_{atm}/T - n_e$ ).

## 8.8 Artificial Dissipation

Some amount of artificial dissipation is required in the present numerical method in order to suppress spurious oscillations that can be de-stabilizing during the time-marching. The form of the term describing artificial dissipation was  $\mu_r \partial^2 \phi / \partial r^2 + \mu_x \partial^2 \phi / \partial x^2$ . The coefficients  $\mu_r$  and  $\mu_x$  were defined differently for different

equations. These were as follows:

$$\mu_{r_{exp}} = \begin{cases} 0.00025\rho dr & \text{for } T \leq 2000K \\ 0.005\rho dr & \text{for } 2000K \leq T \leq 10000K \\ 0.025\rho dr & \text{for } T \geq 10000K \end{cases}$$

and

$$\mu_{r_{imp}} = 5e - 6/dr$$

$$\mu_{x_{exp}} = \begin{cases} 0.05\sqrt{T}dx & \text{for } T \leq 10000K \\ 0.025\sqrt{T}dx & \text{for } T \geq 10000K \end{cases}$$

$$\mu_{x_{imp}} = \begin{cases} 0.0025\sqrt{T}dx & \text{for } T \leq 2000K \\ 0.00025\sqrt{T}dx & \text{for } T \geq 2000K \end{cases}$$

Coefficients in the artificial dissipation term for the external flow were as follows:

$$\mu_{r_{exp}} = \begin{cases} 0.0005\rho dr & \text{for } T \leq 2000K \\ 0.005\rho dr & \text{for } 2000K \leq T \leq 10000K \\ 0.025\rho dr & \text{for } T \geq 10000K \end{cases}$$

and

$$\mu_{r_{imp}} = 2.5e - 3/dr$$

$$\mu_{x_{exp}} = \begin{cases} \sqrt{T}dx & \text{for } T \leq 2000K \\ 0.05\sqrt{T}dx & \text{for } 2000K \leq T \leq 10000K \\ 0.05\sqrt{T}dx & \text{for } T \geq 10000K \end{cases}$$

$$\mu_{x_{imp}} = \begin{cases} 0.1\sqrt{T}dx & \text{for } T \leq 2000K \\ 0.0005\sqrt{T}dx & \text{for } 2000K \leq T \leq 10000K \\ 0.00025\sqrt{T}dx & \text{for } T \geq 10000K \end{cases}$$

This artificial dissipation model was used in the simulation as it was found to be most stable numerically. It is seen that the flow regimes can be categorized into three regions.  $T \leq 2000K$  represent cold regions of the flow - regions close to the inlet plane in the internal flow and regions close to the torch body in the external flow are characterized

by such temperatures. Regions close to the core of the arc are characterized by temperatures between 2000 K and 10000 K, both in the internal and external flow. Temperatures above 10000 K are typical of the arc core. In the colder regions, where the mass-density is high the  $\mu_r$  has a smaller constant multiplicative value as compared to the hotter regions which have a lower mass-density. Constant multiplicative factors for the implicit and explicit terms in the axial directions also scale with temperature. The constant multiplicative factors were obtained by trial and error. They were based on the idea that insufficient dissipation leads to unphysical values of the dependent variables and instability. Location of the maximum and minimum values of temperature, pressure and velocity in the computational domain were monitored. The multiplicative factors were varied only in those temperature regions where the minimum values were unphysical. This approach, though ad-hoc, provides a very good measure with which to vary dissipation.

## 8.9 Results

The physical domain for the internal flow computations consisted of a portion extending about 8 mm inwards from the exit plane of the torch. The cathode tip is approximately 3 mm from the exit plane (see Figure 59). This portion of the torch was chosen as it is important to model the region before the plasma gas encounters the arc. The cold gas flow through the entire torch assembly is not modeled. The results of this simulation are compared to experiments conducted at the Industrial, Systems and Welding Engineering Department (ISWE) at OSU [Ref. 53]. The case study presented

here is compared with an experiment with the following operating conditions:

Polarity	Straight
Plasma Gas	Argon
Shield Gas	Argon
Plasma Gas flow rate (CFH)	13
Shield Gas flow rate (CFH)	35
Current (Amps)	100
Stand-off Distance (in.)	3/8
Power (KW)	2.3

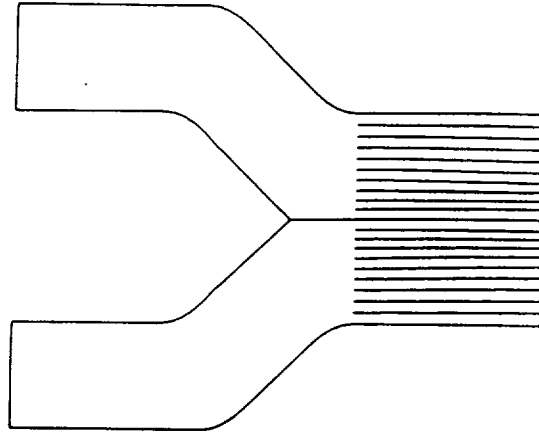
In the experiment, a radial profile of the static pressure (gage) at the surface of a water-cooled copper plate can be measured for different operating conditions by scanning the plasma torch over a water-cooled plate with a pressure tap. A pressure trace obtained for the above mentioned conditions was compared with the results of the present simulation.

An internal and external flow simulation for the above mentioned experimental conditions was performed. It is difficult to match the exact experimental conditions in terms of the flow rates as these are measured far upstream of the torch exit. To match these conditions as closely as possible, the simulations aimed at obtaining a mass-flow rate corresponding to the experimental volume flow rate at a temperature of 300 K. A total upstream pressure of 40 in. of water (gauge) was required to give a mass-flow rate of 0.235 g/s at the exit plane. This corresponds to a volume-flow rate of 15 CFH. A power-level of about 2.4 KW (matching the experimental conditions) was obtained by setting the conductivity floor at 1000 mho/m. These simulations were run on a Silicon Graphics Challenger L workstation. A uniform  $50 \times 32$  grid was used in this simulation of the internal flow and converged solutions were obtained in about 12-15 hours of CPU time.

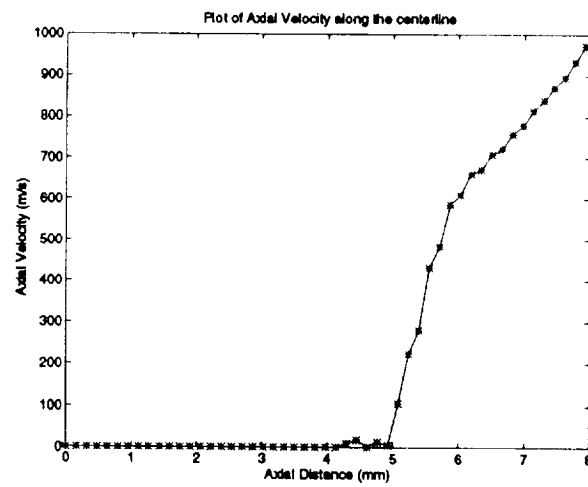
The computational domain for the external flow extends from the centerline up to the edge of the torch body and from the exit plane of the torch to the workpiece. Physically, it is a rectangle of dimensions 9.5 mm by 12.7 mm. The boundary of the computational domain (along the torch exit plane) is split into three regions - the region representing the exit plane of the torch (1.58 mm), region representing the shield gases (7.93 mm) and the region along the solid torch body (3.175 mm) (see Fig 60). A uniform  $30 \times 80$  grid was used in this computation of the external flow. These simulations were also run on a Silicon Graphics Challenger L workstation and converged solutions were obtained in about 15 hours of CPU time. Since the results of the simulation were compared against gage pressures less than 20 inches of water, it was necessary to ensure convergence of the non-dimensional quantities to at least 4 decimal places. This had to be done as the non-dimensional pressure values are multiplied by  $1.1267 \times 10^5$  (value of  $P_{ref}$ ) to obtain dimensional values of pressure.

#### 8.9.1 Results for Internal and External Flow

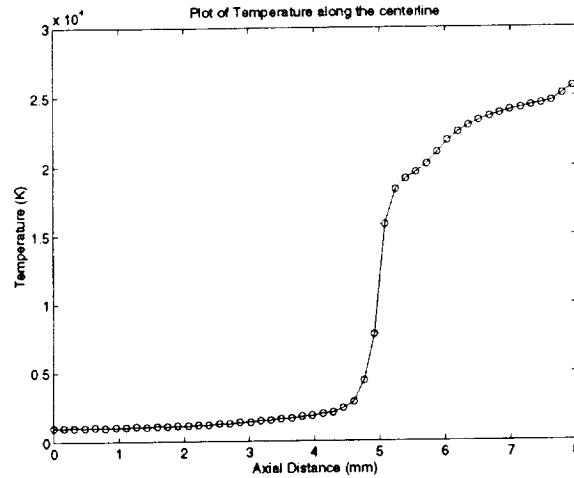
Figure 61 shows the current contours within the torch. The current lines leave the exit-plane of the torch towards the workpiece. The electromagnetic computations are performed only in the straight section of the torch assembly hence the current lines do not extend all the way to the cathode tip.



**Figure 61 Current Contours within the plasma torch**

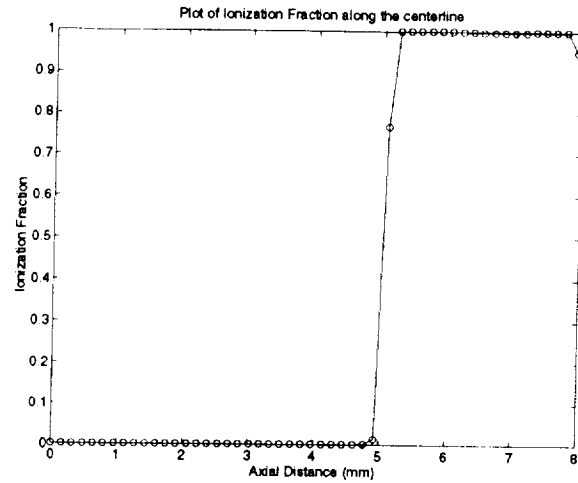


**Figure 62 Centerline Axial Velocity Profile**

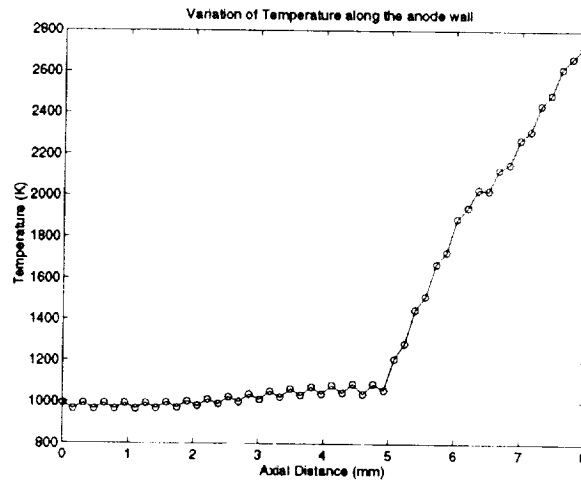


**Figure 63 Centerline Temperature Profile**

Figures 62 and 63 show the velocity and temperature profiles along the centerline, respectively. It can be seen that the cold plasma gas is moving at a low velocity, till it encounters the hot arc region. The energy gained from the arc (by Ohmic heating) accelerates the gas and also raises its temperature considerably. This energy addition to the gas brings about ionization of the cold gas as can be seen in Fig 64 depicting the variation of the ionization-fraction ( $\alpha$ ) along the centerline. It is interesting to note that the plasma gas is fully ionized along the centerline in the region of the arc. This indicates that doubly ionized argon atoms  $Ar^{++}$  may well be present in the experiment, although these have not been included in the calculations.



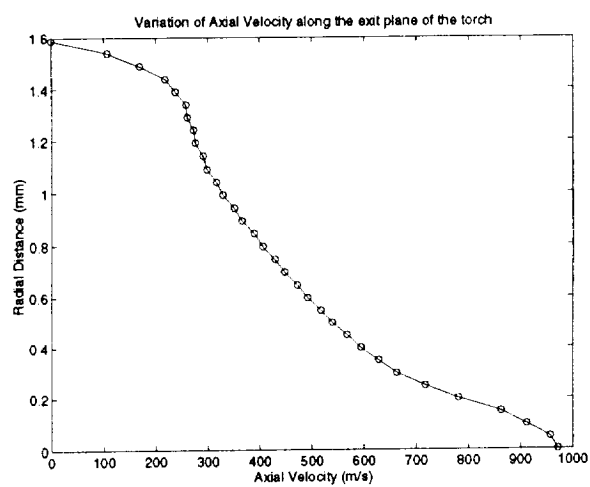
**Figure 64 Centerline Ionization Fraction Profile**



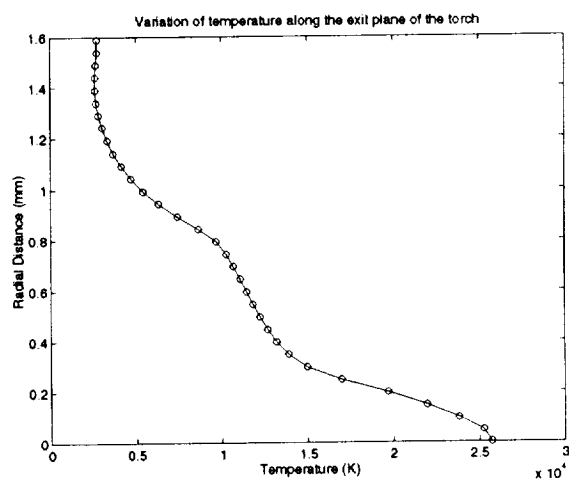
**Figure 65 Plasma Temperature along the inner surface of the torch body**

Figure 65 shows the plasma temperature profile along the inner surface of the anode. It can be seen that the temperature remains fairly constant till the flow encounters the region close to the arc where it rises rapidly to about 3000 K. These gas temperatures are not unrealistic as the inner surface of the nozzle undergoes a considerable amount of deterioration.

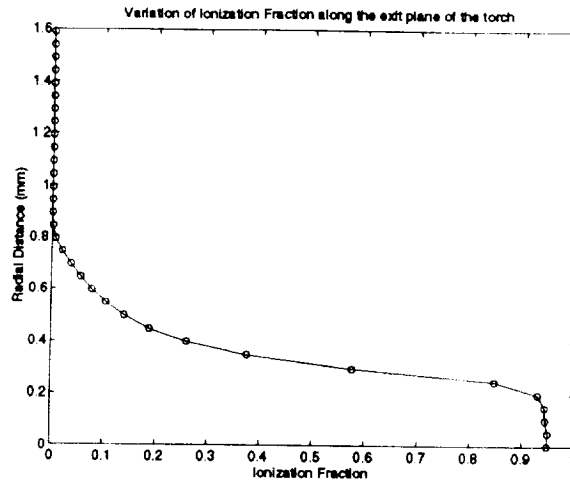




**Figure 66** Radial profile of axial velocity at the exit plane of the plasma torch

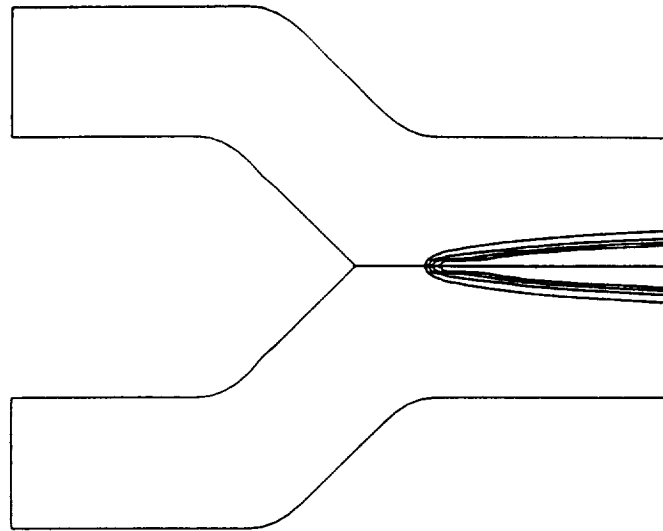


**Figure 67** Radial profile of Temperature at the exit plane of the plasma torch

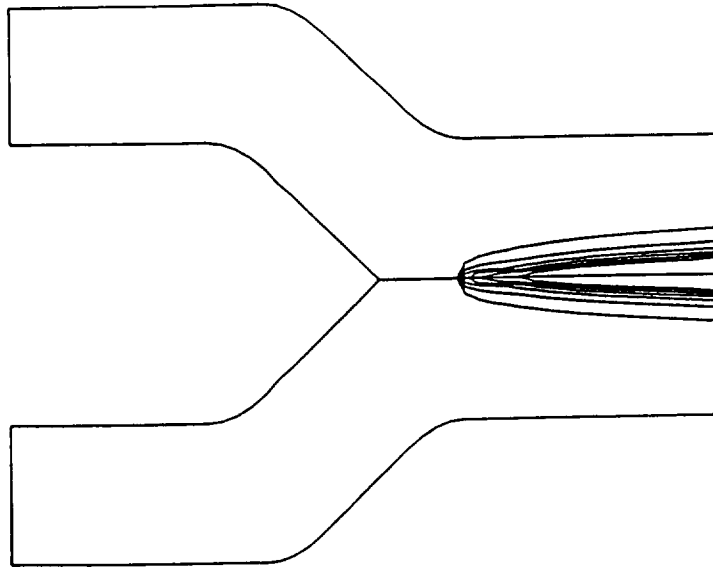


**Figure 68** Radial profile of Ionization fraction at the exit plane of the torch

Figure 66 through 68 show profiles of radial velocity, temperature and ionization fraction at the exit plane. Steep gradient in velocity and temperature are seen in regions close to the centerline. The gradient is less steep in regions further away from the centerline.

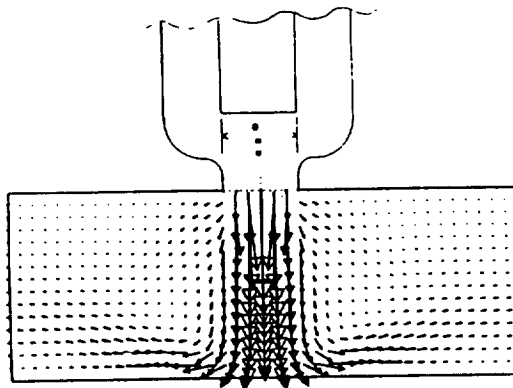


**Figure 69** Ionization fraction in the plasma torch. Innermost contour is  $\alpha = 1.0$ , the outermost is  $\alpha = 0.2$ . Each contour is incremented by 0.2

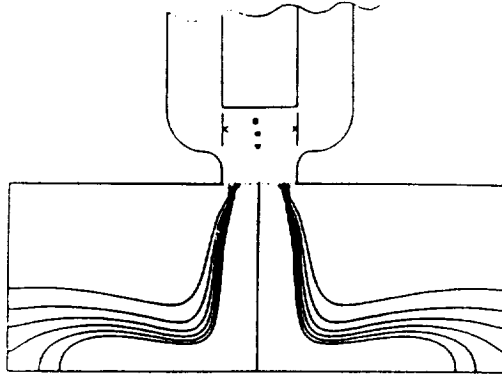


**Figure 70 Temperature contours in the plasma torch. Innermost contour is  $T=20,000$  K, the outermost is  $T = 12,000$  K. Each contour is incremented by 1,600 K**

Figures 69 and 70 show contours of ionization fraction and temperature, respectively in the plasma torch. The region close to the centerline consists of the hot core. A high degree ionization is expected in this region as shown in Figure 69.

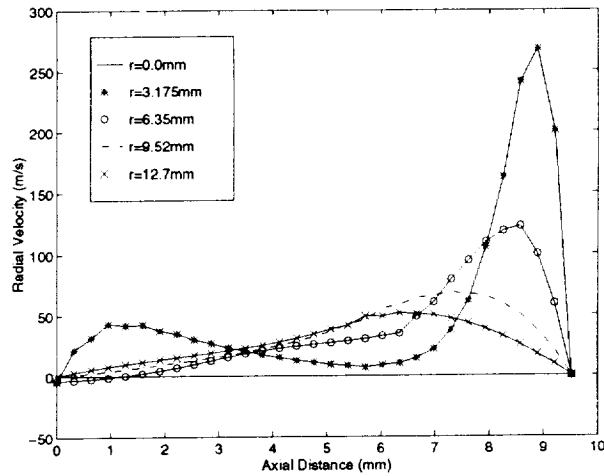


**Figure 71 Velocity Vectors in the external flow of the plasma jet**



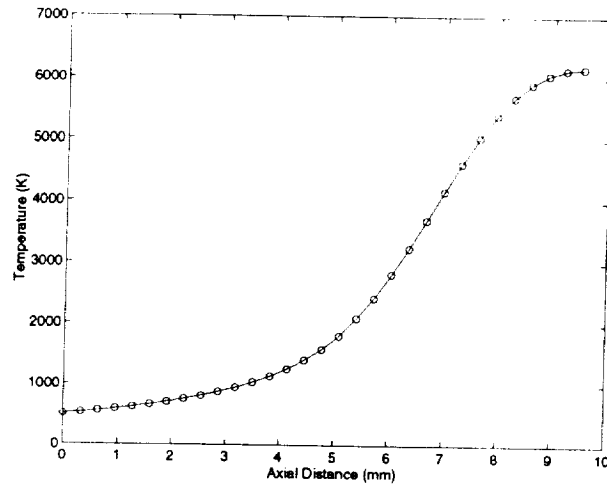
**Figure 72 Temperature Contours in the external jet. The innermost is  $T = 8000$  K, and the outermost is  $T = 2000$  K. Each contour is incremented by 1,200 K**

Figure 71 shows the velocity vectors in the external flow. Temperature contours are shown in Figure 72. It can be seen that plasma jet spreads very little. The innermost contour shows the high temperature regions (temperatures above 8000) in the arc. The turning of the hot gas flow is illustrated by these two plots.



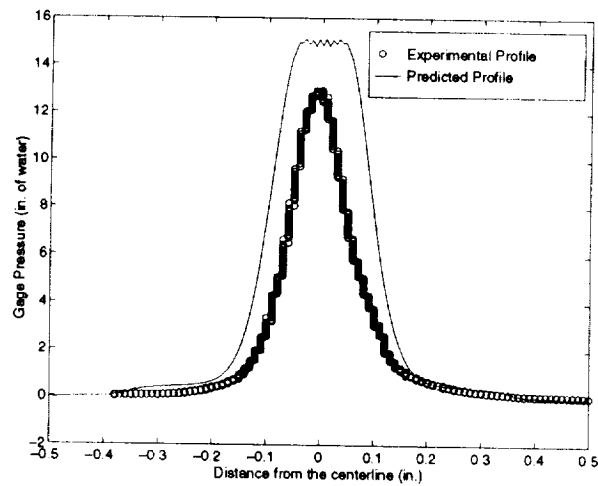
**Figure 73 Radial component of velocity in the Plasma torch external flow at five radial locations:  $r=0\text{mm}$ ,  $r=3.175\text{mm}$ ,  $r=6.35\text{mm}$ ,  $r=9.525\text{mm}$  and  $r=12.7\text{mm}$**

Figure 73 displays the growth of the wall jet. It can be seen that with radially increasing distances from the centerline, the maximum radial velocity increases up to a point and then decreases thereafter. Also the location of the maximum velocity in each of the radial velocity profiles occurs further away from the workpiece (stagnation plane) with increasing distance from the centerline. These are typical characteristics of wall jets.



**Figure 74 Temperature profile at the edge of the computational domain in the external flow,  $r=12.7\text{mm}$**

Figure 74 shows the temperature of the gas along radial outflow boundary (along DE in Figure 60). It is seen that the temperatures near the workpiece are high but drop off sharply with increasing distance from the workpiece.



**Figure 75 Comparison of the radial distribution of static pressure along the surface of the workpiece with experimental data from [Ref. 53]**

Figure 75 shows a comparison of the static pressure profile obtained experimentally (the

only quantity measured) and that obtained from the simulations. The pressure profile obtained experimentally shows that the plasma jet tends to remain collimated. It is seen that the arc pressure (gage) drops sharply to values close to zero within a distance of about three times the nozzle radius from the centerline. The pressure profile predicted by the simulations match the experiments very well. The steep drop off in the profile is not captured very well by the simulations in regions very close to the centerline. This is largely due the effects of artificial dissipation.

## 8.10 Discussion of Results

The current contours in the internal flow (see Figure 61) depict the current flow that is expected in such plasma arcs where the stand-off distance is small. The high velocities at the exit plane and the small stand-off distance restrains the arc from expanding. This is important for concentration of the heat load on the workpiece so as to obtain maximum peneration of the weld pool and obtain the keyholing effect. The heating of a subsonic flow leads to its acceleration. The axial velocity profile along the centerline shows this effect rather well. Based on these velocities, the residence time of the gas in the region of the arc is on the order of a few microseconds. These relatively long residence times allow the gas to proceed towards thermal equilibrium and full ionization. The sharp drop off in the radial temperature distribution at the exit plane (Figure 67) in regions close to the centerline is due to the high degree of ionization.

The temperature contours representing the temperature field in the external jet closely follow the velocity vectors representing the flow. These contours also show that the hot

core of the jet does not expand very much. The predicted pressure profiles although demonstrating good agreement with experiments do not completely capture the steep drop off shown by experiments. The experimental data show that  $dp/dr|_{z=L}$  is negative and large in regions close to the centerline. This behaviour could possibly be due to the shape of velocity profile issuing out of the plasma torch and the cooling of the plate. It is possible that the drop-off in the real axial velocity profile along the exit plane may be steeper than that predicted by the internal flow simulation. This could impact the shapes of the radial pressure profiles predicted by simulation and those observed experimentally. Another possible reason is the cooling of the plate. The cooling of the plate was simulated by a convective boundary condition with a radially varying heat-transfer coefficient. Since  $P = n_T kT$ , the following analysis is likely to explain the difference in shapes of the pressure profiles close to the centerline.

$$\frac{dP}{dr} = n_T k \frac{dT}{dr} + kT \frac{dn_T}{dr}$$

As it can be seen from the above equation,  $dP/dr$  is zero at the centerline, however, the shape of the profile depends on the radial slopes of temperature and total number density and temperature and total number density. All these quantities at the plate surface depend on the cooling of the plate. Our model is unable to capture this effect in regions close to the plate. Varying  $h_o$  and  $\alpha$  did not affect the shape of the pressure profile in that region. A more elaborate heat-transfer model is probably needed to model the cooling of the plate in regions close to the centerline. Lastly, the effects of artificial dissipation could also lead to the flatness of the pressure profile in regions close to the centerline.

In summary, a self-consistent numerical model of the plasma flows within the VPPA welding torch and the external jet impinging on a plate have been developed. This is the



most comprehensive model based on first principles developed to date, and the very first complete model of a transferred arc. Although its development consumed a majority of the two years duration of this contract, important insight has been gained into the nature of the plasma flow in a VPPA torch and its influence on the skew.



## 9. CONCLUSION

This work has focused on the characterization of the VPPAW process and the investigation of arc skewing tendencies with the objective of offering possible solutions to the arc skew problem and the associated undercutting. Based on the study of the VPPAW process and the results of the arc skew investigation the following conclusions can be drawn:

1. The main sources of arc skew are associated with geometrical asymmetries within the torch, specifically the electrode and the orifice.
2. These asymmetries can be related to orifice and/or electrode deterioration sustained during long term operation. In addition, deterioration associated with the pilot arc operation can accelerate asymmetric deterioration and arc skewing tendencies.
3. The pilot arc itself can introduce asymmetries in the torch configuration leading to arc skew.
4. Initial misalignment of the electrode and orifice introduces asymmetries in the welding torch, and also cause arc skew. However, this skew would appear immediately upon start-up, as opposed to manifesting itself after some time.
5. Our observations indicate the tendency of the skew to occur in the same direction as the pilot arc attachment on the orifice inner wall.

From investigating possible solutions to the arc skew phenomena, the following conclusions can be drawn:

1. The direction of EP current to a second electrode, as well as to the orifice, resulted in a significant decrease in electrode deterioration. Therefore, by using these configurations, electrode deterioration can be reduced. Also, torch current carrying capacity may be increased using either method.
2. More research is needed in order to determine to what extent the second electrode or the orifice electrode configuration can reduce or eliminate the arc skew under practical application.

Future work regarding possible changes to the welding process and torch design is warranted. Specifically, the knowledge gained from the present experiments can be applied to future torch designs, thereby eliminating or reducing the problem of arc skew. Additional research on controlling current flows to reduce electrode and orifice deterioration may result in solution of the arc skew problem.

## LIST OF REFERENCES

- Ref. 1 Fuerschbach, P. W. 1985. Plasma Arc Welding, Equipment, Installation, and Process Control. Sandia National Laboratories. SAND84-2146.
- Ref. 2 Welding, Brazing, and Soldering. 1993. Vol. 6. ASM Handbook. p.195-199.
- Ref. 3 Torres, M. R., McClure, J. C., Nunes, A. C. and Gurevitch, A. C. April 1992. Gas Contamination Effects in Variable Polarity Plasma Arc Welded Aluminium. *Welding Journal* 71(4):123-s to 131-s.
- Ref. 4 Tomsic, M. and Barhorst, S. February 1984. Keyhole Plasma Arc Welding of Aluminium with Variable Polarity Power. *Welding Journal* 63(2):25 to 32.
- Ref. 5 O'Brien, R. L. 1991. Welding Processes. *Welding Handbook*. AWS. 8<sup>th</sup> Edition. Vol. 2.
- Ref. 6 Nunes, A. C., Bayless, O. E., Jones III, C. S., Munafo, P. M. Biddle, A. P. and Wilson, W. A. June 1983. The Variable Polarity Plasma Arc Welding Process: Its Application to the Space Shuttle External Tank - First Interim Report. NASA Report No: NASA TM-82532.
- Ref. 7 Plasma Arc Welding Torch. Materials & Processes Laboratory. Marshall Space Flight Center. NASA. Pub. 5-505-3.

- Ref. 8 Waldron, D. J. Arc/Metal Interaction in Variable Polarity Plasma Arc Welding. *McDonnell Douglas Aerospace*. Project 1-293:1 to 8.
- Ref. 9 Cary, Howart B. 1994. Modern Welding Technology. 43<sup>rd</sup>. Edition. p. 81-89.
- Ref. 10 Tomsic, M. and Barhorst, S. 13-15 September 1983. The cathode etching technique for automated aluminium tube welding. *Development and Innovations for Improved Welding Production*. International Conference in Birmingham, UK. P38-1 to P38-7.
- Ref. 11 Rodriguez, D. R. 1985. Variable Polarity Plasma Arc Welding (VPPAW) of Aluminium Alloys. Masters Thesis. The Ohio State University.
- Ref. 12 Pang, Q., Pang, T., McClure, J. C. and Nunes, A. C. Workpiece Cleaning During Variable Polarity Plasma Arc Welding of Aluminium. NASA Contract No. NAS8-36822.
- Ref. 13 Manufacturing/Fabrication. June 1995. Swirl Ring Improves Performance of Welding Torch. NASA Tech Brief. p. 78.
- Ref. 14 Spraragen, W. and Lengyel, B. A. Physics of the Arc and the Transfer of Metal in Arc Welding. January 1943. Welding Research Supplement to the Welding Journal. p. 2-s to 42-s.
- Ref. 15 Taylor, P. L. Development and test of a system for the study of Full Penetration Gas Tungsten Arc Welding. Masters Thesis. Department of Welding Engineering. The Ohio State University, 1990.
- Ref. 16 Hobart Owner's Manual No. OM-197. Model VP-300-S Variable Polarity Welding Machine. Issued: July 27/81. Revised: November 9/82.

- Ref. 17 Hobart Owner's Manual No. OM-364. Model MPW-400C Plasma Torch. Issued: July 25/83. Revised: November 1/85.
- Ref. 18 Hobart Owner's Manual No. OM-304. Hobart 300 Programmer Issued: February 17/83.
- Ref. 19 Hobart Owner's Manual No. TM-680. Plasma Control Console Model HPW-400. Issued: January 29/79. Revised: September 12/80.
- Ref. 20 Current/Watt Sensors. PI SERIES. F. W. Bell. Orlando, Florida. Publication #910205S 360960.
- Ref. 21 PX150 Series Pressure Transducer. February 1989. Omega. Stamford, Connecticut. Operator's Manual: M804/038.
- Ref. 22 PX140 Series Pressure Transducer. 1993. Omega. Stamford, Connecticut. Operator's Manual: M0258/0593.
- Ref. 23 The Temperature Handbook. 1992. Omega Temperature Measurement Handbook & Encyclopedia. Vol 28.
- Ref. 24 Pang, Q., Pang, T., McClure, J. C. and Nunes, A. C. Spectroscopic Measurements of Hydrogen and Oxygen in Shielding Gas During Plasma Arc Welding. NASA Contract No. NAS8-36822.
- Ref. 25 Pang, Q. and McClure, J. C. Emission Spectrum and Resistivity of Low Pressure Weld Arcs. Metallurgy and Materials Engineering Department. University of Texas at El Paso.
- Ref. 26 Analog Devices Inc. 1987. The 5B User's Manual. Publication # G1114-20-8/87.

- Ref. 27 Nelson, J. G. and Brungraber, R. J. March 1973. Effects of Welding Variables on Aluminum Alloy Weldments. *Welding Journal* 52(3):97s.
- Ref. 28 Beil, R. J., Hahn, G. T. and Hartman, J. A. March 1987. Effect of Copper-Rich Regions newline on Tensile Properties of VPPA Weldments of 2219-T87 Aluminum. *Welding Journal* 66(3):73s.
- Ref. 29 Nunes, A. C., Bayless, E. O. and Jones, C. S. October 1984. Variable Polarity Plasma Arc Welding on the Space Shuttle External Tank. *Welding Journal* 63(10):27 to 35.
- Ref. 30 Hughes, W. F. and Young, F. J., *Electromagnetodynamics of Fluids.*, John Wiley & Sons, NY, 1966.
- Ref. 31 Todreas, N. E. and Kazimi, M. S., *Nuclear Systems I- Thermal-Hydraulic Fundamentals.*, Taylor & Francis, 1990.
- Ref. 32 Babu, V. and Subramaniam, V. V., *Journal of Thermophysics & Heat Transfer*, Vol. 9, No.2, pp. 227-232, April-June 1995.
- Ref. 33 Anderson, D. A, Tannehill, J. C and Pletcher, R. H., *Computational Fluid Mechanics and Heat Transfer*, Hemisphere Publishing Corporation, Washington, 1984.
- Ref. 34 Briley, W. R, and McDonald, H., *Journal of Computational Physics*, 24, pp. 372-397, 1977.
- Ref. 35 Vincenti, W. G and Kruger C. H., *Introduction to Physical Gas Dynamics*, John Wiley and Sons, Inc., New York, N.Y, 1965.
- Ref. 36 Sutton, G. W. and Sherman, A., *Engineering Magnetohydrodynamics.*, McGraw-Hill, New York, 1965.



- Ref. 37 Mitchner, M and Kruger, C. H. Jr., *Partially Ionized Gases*, John Wiley & Sons, 1973.
- Ref. 38 MacCormack, R. W., *AIAA Paper 81-0110*, 1981.
- Ref. 39 Beam, R. M and Warming, R. F. *AIAA Journal*, **16**, No. 4, 393-402, 1978.
- Ref. 40 Richtmeyer, R. D. and Morton, K. W., *Difference Methods for Initial-Value Problems*, Interscience Publishers, John-Wiley & Sons, 2<sup>nd</sup> edition, 1967.
- Ref. 41 Oran, E. S. and Boris, J. P., *Numerical solution of reacting flows*, 154, Elsevier Science Publishing Co. Inc., New York, 1987.
- Ref. 42 Isaacson, E and Keller, H. B., *Analysis of Numerical Methods*, Wiley, New York, 1966.
- Ref. 43 Hansen, W. F. and Clark, K., *Numerical Methods in Reactor Analysis*.
- Ref. 44 Mitchell, A. R., "Numerical Methods for Partial Differential Equations," Barnes & Noble, New York, 1969
- Ref. 45 Tajima, T., "Computational Plasma Physics: With Applications to Fusion and Astrophysics", Addison-Wesley Publishing Co. Inc, 1989, p. 142-144.
- Ref. 46 McKelliget, J., Szekely, J., Vardelle, M. and Fauchais, P., *Plasma Chem. Plasma Process*, **2**, 1992.
- Ref. 47 Dilawari, A. H. and Szekely, J., *Plasma Chem. Plasma Process*, **7**, 1987.
- Ref. 48 Lee, Y. C. and Pfender, E., *Plasma Chem. Plasma Process*, **7**(1), 1987.

- Ref. 49 Scott, D. A., Kovitya, P. and Haddad, G. N., *J. Appl. Phys.*, 66(11), December 1989.
- Ref. 50 Westhoff, R. and Szekely, J., *J. Appl. Phys.*, 70(7), October 1991.
- Ref. 51 Murphy, A. B., and Kovitya, P., *J. Appl. Phys.*, 73(10), May 1993.
- Ref. 52 Fincke, J. R., Snyder, S. C. and Swank, W. D., *Rev. Sci. Instrum.*, 64(3), March 1993.
- Ref. 53 Pagan, J. M., Masters Thesis, The Ohio State University, June 1996.
- Ref. 54 Aithal, S. M., Subramaniam, V. V. and Babu, V., "*Numerical simulation of plasma and reacting flows*", (Invited Paper, No. 96-2024), presented at the 27<sup>th</sup> AIAA Fluid Dynamics meeting, New Orleans, June 18-21, 1996.
- Ref. 55 Aithal, S. M., Subramaniam, V. V. and Babu, V., "*Effects of Arc Attachment on Arcjet Flows*", Paper No. 96-3295, presented at the 32<sup>nd</sup> AIAA/ASME/SAE/ASEE Joint Propulsion Conference, Lake Buena Vista, Fl, July 1-3, 1996.